Addressing of individual Barium ions for quantum information processing

A master's thesis submitted to the faculty of mathematics, computer science and physics, of the University of Innsbruck in partial fulfillment of the requirements for the degree of

Master of Science (MSc)

carried out at the Institute of Experimental Physics under the supervision of

Assoz. Prof. Dr. Thomas Monz
Ass.-Prof. Dr. Martin Ringbauer

written and presented by

Walter J. Hörmann



Institute for Experimental Physics
University of Innsbruck
March 2026

Abstract

This thesis presents the modification, characterization, and experimental implementation of an optical addressing system for the manipulation and control of trapped $^{138}Ba^{+}$ ions in a quantum computing experiment. A central focus of this work is the detailed opto-mechanical characterization of the addressing optics and their subsequent integration into the experimental apparatus. Key system properties, including the achievable focal spot size, the available addressing range in the ion plane, and the magnitude of single-ion addressing–induced crosstalk, are investigated experimentally.

Furthermore, the specific design and implementation of the addressing system enable an alternative approach to fulfilling the experimental requirements for addressed light-shift gate operations on motional modes transverse to the optical axis of the addressing laser beams. The feasibility and limitations of this novel approach are discussed theoretically and supported by experimental results presented in this thesis.

Zusammenfassung

Diese Arbeit präsentiert die Modifikation, Charakterisierung und experimentelle Implementierung eines optischen Adressierungssystems zur Manipulation und Kontrolle gefangener $^{138}Ba^{+}$-Ionen in einem Quantencomputing-Experiment. Ein zentraler Schwerpunkt dieser Arbeit ist die detaillierte optomechanische Charakterisierung der Adressierungsoptik sowie deren anschließende Integration in den experimentellen Aufbau. Zentrale Systemeigenschaften, darunter die erreichbare Fokusgröße, der verfügbare Adressierungsbereich in der Ionenebene sowie das Ausmaß des durch Einzelionenadressierung induzierten Crosstalks, werden experimentell untersucht.

Darüber hinaus ermöglichen das spezifische Design und die Implementierung des Adressierungssystems einen alternativen, neuartigen Ansatz zur Erfüllung der experimentellen Anforderungen für adressierte Light-Shift-Gatteroperationen auf Bewegungsmoden, die transversal zur optischen Achse der adressierenden Laserstrahlen liegen. Die Realisierbarkeit und die Grenzen dieses neuartigen Ansatzes werden theoretisch diskutiert und durch die in dieser Arbeit präsentierten experimentellen Ergebnisse untermauert.

Contents

1 Introduction **4**

2 Quantum information with trapped ions **7**
2.1 Basics of quantum information processing . . . 7
2.1.1 Single-qubit gate operations . . . 8
2.1.2 Two-qubit gate operations . . . 10
2.1.3 Entanglement and fidelity . . . 11
2.2 Optical concepts . . . 14
2.2.1 Gaussian optics . . . 14
2.2.2 Jones formalism . . . 15
2.2.3 Nijboer-Zernike diffraction theorem . . . 16
2.3 Paul trap and general trapping procedure . . . 17
2.3.1 Paul trap . . . 17
2.3.2 General trapping procedure . . . 22
2.4 Cooling, readout and SPAM of $^{138}Ba^{+}$ qubits . . . 23
2.4.1 Cooling methods . . . 23
2.4.2 State preparation and measurement via readout (SPAM) . . . 24
2.5 Ion-light interactions with a harmonically confined ion . . . 27
2.5.1 Single-light-field interaction Hamiltonian . . . 27
2.5.2 Raman interaction Hamiltonian . . . 32
2.5.3 Optical forces . . . 33
2.6 Physical realization of gate operations . . . 33
2.6.1 Single-qubit gate operations . . . 33
2.6.2 Two-qubit gate operations . . . 35
2.6.3 Transverse light-shift gate operation . . . 39

3 Qubit considerations **42**
3.1 Qubits with calcium ions ($^{40}Ca^{+}$) . . . 42
3.2 Qubits with barium ions ($^{138}Ba^{+}$) . . . 44

4 Experimental setup **46**
4.1 Overview and laser alignment . . . 46
4.2 Optical addressing and imaging . . . 48
4.3 Light distribution and addressing control . . . 51

5 Layout of addressing units and incorporation of phase plate **53**
5.1 Addressing unit layout . . . 53
5.2 TEM_{10} mode creation and phase plate incorporation . . . 55
5.2.1 Physical working principle of the phase plate for TEM_{10} mode generation . . . 55
5.2.2 Mount adapter . . . 56

6 Characterization and implementation of addressing units **57**
6.1 Collimation quality of addressing unit input . . . 57
6.2 Efficiency and bandwidth of both AOD devices . . . 58
6.3 Fundamental addressing properties in the ion plane . . . 61
6.3.1 Spot size characterization after the Photon Gear objective . . . 61
6.3.2 Deflection range . . . 66
6.3.3 Estimation of Airy fringe induced crosstalk . . . 67
6.4 Quantification of aberrations through addressing optics . . . 68
6.5 Quality of created TEM_{10} mode . . . 69
6.6 Contrast investigation of addressing beam superposition . . . 70
6.7 Implementation and performance optimization . . . 73

7 Conclusion and outlook **78**

8 Acknowledgment **84**

Chapter 1

Introduction

Most of our classical physical laws lose their validity when studying microscopic systems at the scale of single atoms. A paradigm-shifting theory had to be developed to accurately describe the physical reality: quantum mechanics. The introduction and development of quantum mechanics was a gradual process, which began with Max Planck in 1900. At this time he proposed that the nature of energy is not continuous, but rather quantized in discrete packets also called quanta [1]. Today we know his proposal better as Planck's quantum hypothesis, for which he was awarded the Nobel prize in 1919. Other physicists adopted his concept to successfully explain complex phenomena in nature, which could not previously be explained within classical physics. Albert Einstein, for example, explained the photoelectric effect through the quantization of light into photons in 1905 [2]. Niels Bohr used the concept of energy quantization to create his atomic model in 1913 [3].

Even though there was still great dispute about certain aspects of the theory, especially about the non-deterministic nature of quantum mechanics when compared to its classical counterpart, it has been officially developed in the 1920s. The works of Paul Dirac, Werner Heisenberg, and Erwin Schrödinger, together with contributions from many other physicists, formed the basis of modern quantum mechanics as we know it today. Heisenberg used matrix formalism to describe the quantum mechanical theory [4], while Schrödinger approached the problem using wave mechanics [5]. Dirac was the first to unify quantum mechanics with Einstein's theory of relativity, effectively laying the foundation of quantum field theory [6].

Over the course of decades new observations contributed to extend the key concepts of quantum mechanics. The principles of wave-particle duality, superposition states, uncertainty relations, and entanglement, are only a few of them. Systems that exhibit such quantum mechanical properties have the capability to interact, interfere and evolve under the laws of quantum mechanical theory. Quantum computers exploit these quantum phenomena in quantum algorithms, where information is encoded and processed in the form of quantum bits. For certain problems, this can reduce the required computational resources substantially, and in some cases exponentially, compared with known classical approaches. Demonstrating such an advantage beyond the reach of practical classical computation is often referred to as quantum supremacy or quantum advantage.

A prominent example of such a theoretical quantum advantage is the integer factorization problem, in which an integer number is factorized into prime numbers. Shor's quantum algorithm solves this problem with polynomial resource scaling, whereas the best known classical algorithms exhibit sub-exponential scaling [7]. This result is particularly relevant for cryptography, since widely used public-key encryption schemes, such as RSA, rely on the practical difficulty of factoring large integers. A sufficiently large and fault-tolerant quantum computer could therefore compromise such encryption schemes with substantially more favorable resource scaling than known classical approaches. This prospect has motivated the development of post-quantum cryptography (PQC), which aims to design cryptographic protocols that remain secure in the presence of quantum computers [8].

When assessing the practical relevance of a quantum algorithm, its asymptotic resource scaling is only one part of the comparison. Present-day quantum processors remain limited by the number of qubits that can be used coherently for computation, corresponding to available register sizes on the order of 10 to 6000 qubits [9]. Classical computing platforms, by contrast, provide extremely large memory registers and highly optimized architectures, which can compensate for less favorable asymptotic scaling over a wide range of practically relevant problem sizes. Therefore, the useful computational power of a device is not determined by register size alone, but also by the rate and fidelity with which elementary operations can be performed. In current classical processors, characteristic operation rates are commonly in the GHz regime, whereas the experimental system considered in this thesis operates on characteristic timescales corresponding to the kHz regime.

The practical benefit of a quantum algorithm is therefore determined by the interplay between algorithmic complexity, available register size, operation rates, initialization and readout overhead, and possible error correction requirements. While exponential improvements in complexity scaling are particularly striking, more moderate scaling advantages can also be relevant for practically important problem classes. Such advantages become relevant when the classical resource requirements grow rapidly with system size, as in the simulation of interacting many-body quantum systems. For example, molecular simulations in chemistry involve a large number of electronic and nuclear degrees of freedom, and the corresponding classical description can become computationally demanding for large molecules. Quantum algorithms with polynomial or otherwise improved scaling may therefore provide a practical advantage beyond a problem-size-dependent crossover regime, even when the asymptotic improvement is less dramatic than in Shor's algorithm [10]. For a broader overview of known quantum algorithms, their applications, and their complexity scaling relative to classical approaches, the reader is referred to the Quantum Algorithm Zoo [11].

A theoretical summary of fundamental building blocks to realize a universal quantum computer device is given by the so-called DiVincenzo criteria [12]. These criteria can be divided into two categories, the first five hold true in general for any quantum computing system, whereas the last two criteria are more relevant for quantum communication and network purposes:

1. The physical system needs to be scalable and provide well-defined qubits. Well-defined qubits imply that the information encoded in the two qubit states must be clearly distinguishable.

2. The ability to initialize the state of the qubits to a simple so-called fiducial state, such as $|00\ldots0\rangle$. This criterion demands that a quantum computer must be able to prepare its qubits reliably in a known initial state. The requirement of a simple fiducial state implies that the fidelity of the initialized state can be confirmed in a convenient and reliable way.

3. Long relevant decoherence times, much longer than the gate operation time: it is of no use to meet all other requirements listed among the DiVincenzo criteria, if the decoherence time is not long enough to let the qubit maintain the encoded information for at least one total sequence of gate operations.

4. A universal set of quantum gate operations: with such a set, arbitrary quantum operations on the computational register can be approximated to desired accuracy.

5. A qubit-specific measurement capability: one needs to be able to measure individual qubits reliably at the end of a computation. In more advanced architectures, mid-circuit measurements can also be used for feedback and error correction.

6. The ability to inter-convert stationary and so-called flying qubits: within a quantum network, information stored in a stationary qubit must be transferable to a flying qubit, such as a photon, and vice versa.

7. The ability to faithfully transmit flying qubits between specified locations: the information carried by the flying qubit must not be lost and be accounted for at all times.

Quantum computers can be realized on different physical platforms, including neutral atoms, ions, superconducting circuits, and photonic systems, with each platform having different advantages, drawbacks, and limitations [13, 14]. Quantum computing with trapped ions offers some advantageous properties that other platforms struggle to reach or may lack completely. In particular, the collectively shared motion of the trapped ions, providing effective all-to-all connectivity, distinguishes this platform from others [15]. Furthermore, the achievable coherence times within ion-trap systems remain among the longest reported to date, with decoherence-free qubit memories in ion traps reaching timescales exceeding 2 hours [16]. Additionally, the electric charge of the ions enables trapping techniques with particularly deep trapping potentials, with typical depths in the range of approximately 0.1 eV to 1 eV. Large trap depths make the confinement robust against losses due to motional excitation and can ease the initial capture of ions during loading, depending on their kinetic energy and the specific trapping approach. Another advantage, which the ion platform in this case shares with the neutral-atom platform, is that ions, as well as neutral atoms, are naturally identical. Since they are identical, the qubits themselves are naturally reproducible, in contrast to many solid-state platforms where fabrication imperfections may lead to device-to-device variations.

Recent continuous progress has enabled quantum-computing systems with increasing qubit numbers and improved operation fidelities. However, present-day processors are still largely described as noisy intermediate-scale quantum (NISQ) devices, where the available number of physical qubits is already large enough to explore non-trivial quantum circuits, but noise and imperfect control limit the circuit depth and computational reliability [17]. In this regime, error suppression techniques aim to reduce the occurrence of errors at the hardware or control level, for example through dynamical decoupling or optimized pulse shaping. Error mitigation techniques, by contrast, aim to reduce the effect of errors on measured observables after the noisy computation, for example through zero-noise extrapolation or probabilistic error cancellation [18]. Although these methods can reduce or compensate the effect of noise, they do not fully eliminate errors and can introduce substantial, in some cases exponential, sampling overhead.

The long-term vision, however, is fault-tolerant quantum computing (FTQC), where quantum error correction (QEC) protects encoded qubits against physical errors. Reaching this regime requires scalable architectures, high-fidelity gates, precise control over individual and collective degrees of freedom, and sufficiently low error rates to make QEC feasible. Therefore, our ion quantum computing experiment aims at demonstrating the highest achievable control over a quantum register of qubits consisting of trapped barium ions. The computational process of every quantum system starts with the initialization of the qubit register through state preparation, followed by the gate sequence implementing the desired quantum algorithm, and ends with measurement and readout. These steps are often summarized as state preparation and measurement (SPAM) together with coherent gate operations.

Contributions to errors, and therefore a decrease of overall process fidelity, can occur during each section of the overall quantum computing process. The origins of these possible errors are diverse and include, among others, environmental interactions with the quantum system, intensity and frequency fluctuations of the involved lasers, cross-talk errors induced by ion addressing, and fundamental error mechanisms of the physical system, such as spontaneous scattering from excited states [19]. Among these contributions, addressing-related errors are particularly relevant for trapped-ion systems, where selected ions must be manipulated without unintentionally perturbing neighboring ions. The optical addressing system allows one to interact with a selection of specific ion(s) via laser light. This thesis focuses on the design, characterization, and implementation of such an optical addressing system, which is therefore directly connected to the control and reduction of addressing-type errors.

The thesis is structured as follows:

- In Chap. 2 an introduction to the basics of ion trap quantum computing is given.
- In the third chapter, Chap. 3, a comparison of different, fundamental qubit properties of the ion species used in our experiment, barium, with those of another commonly used one, calcium, can be found.
- In the following chapter, Chap. 4, the reader finds an overview of the experimental setup of the experiment.
- Then, in Chap. 5, a summary of the addressing unit layout is given, together with a description of the specific purpose of each individual component.
- In Chap. 6 the opto-mechanical characterization of the addressing units as well as the processes of their implementation and optimization are documented.
- Finally, in Chap. 7 the achieved results are consolidated. An outlook for future work is completing this thesis.

Chapter 2

Quantum information with trapped ions

In this chapter, fundamental concepts, tools, and definitions relevant to quantum computing are introduced. The discussion begins with a general overview of quantum information theory and subsequently narrows to the trapped-ion quantum computing platform and its defining characteristics. Optical principles such as Gaussian-beam propagation, which are essential for understanding the experimental methods used within this work, are outlined. The operating principles of radio-frequency (RF) traps are presented, accompanied by the theoretical background and a detailed description of the trapping process. Additionally, the mechanisms of laser cooling, state detection, and SPAM are described. Several theoretical approaches of controlled interactions with trapped ions are reviewed, followed by an explanation of how quantum gate operations are physically implemented on the ionic platform.

2.1 Basics of quantum information processing

The fundamental unit of information in quantum computing is the qubit. A qubit has, in analogy to the classical bit with 'zero' and 'one', two states building up the computational space, $|n\rangle = \{|0\rangle, |1\rangle\}$. However, in contrast to the case of a classical bit, a qubit can occupy a coherent superposition of the computational basis states and can therefore be described as:

$$|\Psi_{\text{qubit}}\rangle = c_0 |0\rangle + c_1 |1\rangle \ , \tag{2.1.1}$$

with c_i being the complex probability amplitudes of respective quantum basis state $|i\rangle$. Eq. 2.1.1 mathematically describes a quantum mechanical two-level system (TLS) [20]. The energetic lower state of a TLS is conventionally defines the ground state, whereas the energetic higher state is called the excited state. One can associate ground and excited states with the computational basis states, $\{|0\rangle, |1\rangle\}$, without loss of generality in arbitrary form, as long as one is consistent in usage. The probability p_i of finding the system in the state $|i\rangle$ can explicitly be found by projection onto this state, with the projector $\hat{P}_i = |i\rangle\langle i|$. This projection then yields the absolute square of the probability amplitude $|c_i|^2$, a property commonly known as Born's rule:

$$p_i = \langle\Psi|i\rangle\langle i|\Psi\rangle = |\langle i|\Psi\rangle|^2 = \text{Tr}\left(|i\rangle\langle i||\Psi\rangle\langle\Psi|\right) = \sum_{i,n=0}^{1} c_i^* c_n \underbrace{\langle i|n\rangle}_{=\delta_{i,n}} = |c_i|^2 \ , \tag{2.1.2}$$

which also can be expressed via the so-called trace (Tr), i.e. the sum over all diagonal matrix elements. Born's rule also requires that all state probabilities are normalized and sum up to one, so that the system always can be found in some state. For a register of N qubits, the total Hilbert space $\mathscr{H}_{\text{total}}$ is spanned by the tensor product of the individual qubit spaces:

$$\mathscr{H}_{\text{total}} = \underbrace{\mathscr{H}_1 \otimes \mathscr{H}_2 \otimes \cdots \otimes \mathscr{H}_N}_{\text{with } N \text{ being \# of qubits}} \ , \tag{2.1.3}$$

with a total complex dimension of $\dim_{\mathbb{C}}(\mathscr{H}_{\text{total}}) = 2^N$. Although classical systems with N bits also possess 2^N possible configurations in their classic state space, they can only occupy one such configuration at a time therein. Quantum systems on the other hand can form superpositions of all 2^N joint computational basis states

simultaneously. If one considers now a quantum system containing two qubits, the overall system state can be expressed using Eq. 2.1.1 as:

$$|\Psi_{\text{total}}\rangle = |\Psi\rangle_A \otimes |\Psi\rangle_B = c_{00}\,|00\rangle + c_{10}\,|10\rangle + c_{01}\,|01\rangle + c_{11}\,|11\rangle \ . \tag{2.1.4}$$

In an idealized situation, qubits are perfectly isolated from their surroundings and can therefore be described and treated in an exact manner using the formalism introduced above. In practice, however, a complete decoupling from the environment is never achievable. Real quantum computers inevitably experience residual interactions with external degrees of freedom. To model and include these effects, a framework capable of describing such open quantum systems is required, namely the density matrix formalism. In this formalism, one associates a quantum state $|\Psi\rangle$ with the corresponding density matrix operator $\hat{\rho}$:

$$\begin{aligned} \hat{\rho} &= \sum_i p_i\,|\Psi_i\rangle\,\langle\Psi_i| \\ &\overset{\text{TLS}}{=} \begin{pmatrix} \rho_{00} & \rho_{01} \\ \rho_{10} & \rho_{11} \end{pmatrix} = \begin{pmatrix} p_0 & c_0 c_1^* \\ c_0^* c_1 & p_1 \end{pmatrix} \ . \end{aligned} \tag{2.1.5}$$

The density matrix $\hat{\rho}$ is a convex combination of rank one density matrices $|\Psi_i\rangle\,\langle\Psi_i|$ and corresponding state probabilities p_i [20]. The density operator is furthermore positive semi-definite, $\hat{\rho} \geq 0$, and therefore Hermitian: $\hat{\rho} = \hat{\rho}^\dagger$, with $\dagger$ denoting the Hermitian adjoint, i.e. complex conjugation followed by transposition. So the density operator has real non-negative eigenvalues only. The trace of $\hat{\rho}$ must equal one to maintain the probability normalization, as the main diagonal elements describe the state populations, as indicated in the second line of Eq. 2.1.5. The off-diagonal matrix elements describe the coherence among the states including the phase relation of a possible superposition state, which can decay through coupling to the system environment. The density operator of pure quantum states is idempotent, $\hat{\rho}^2 = \hat{\rho}$, a characteristic used to define the purity. The purity gives rise to the definition of mixedness M :

$$M = 1 - \text{Tr}(\hat{\rho}^2) \ , \tag{2.1.6}$$

which indicates how pure or, respectively, mixed a given quantum state $|\Psi\rangle \cong \hat{\rho}$ is. Also expectation values of observables can be calculated using either directly the quantum state and the corresponding observable operator $\hat{O}$ or the equivalent density operator formalism alongside the trace:

$$\langle\hat{O}\rangle = \langle\Psi|\,\hat{O}\,|\Psi\rangle \iff \langle\hat{O}\rangle = \text{Tr}(\hat{O}\hat{\rho}) \ . \tag{2.1.7}$$

Every quantum-computing platform follows the same structural procedure during the computational process. First, the system must be initialized in a well-defined state from which the computation begins. This initialization is performed by preparing the system in the desired state and subsequently verifying it through measurement, a combined procedure referred to as state preparation and measurement (SPAM). After initialization, the actual computation is carried out by applying a sequence of quantum gate operations that implement the mathematical structure of the problem under consideration. Once the gate sequence has been completed, the final state of the system is evaluated by performing a readout measurement. The SPAM and readout procedures specific to the trapped-ion quantum-computing platform are discussed in Sec. 2.4, supported by the visual aid of energy level diagrams. The theoretical description of gate operations in general is presented in this section, while the principles underlying their physical realization on the ionic platform are introduced in Sec. 2.6.

2.1.1 Single-qubit gate operations

Manipulations on a qubit that involve unitary state evolution without loss of information are referred to as coherent gate operations [21]. Such operations are described mathematically by unitary operators, i.e. unitary matrices, meaning that their action is both deterministic and reversible [20]. A unitary matrix $\hat{U}$ is mathematically defined by the condition:

$$\hat{U}\hat{U}^\dagger = \mathbb{1} = \hat{U}^\dagger\hat{U} \iff \hat{U}^{-1} = \hat{U}^\dagger \ . \tag{2.1.8}$$

All unitary operators preserve norms when acting upon a state:

$$|||\Psi^{'}\rangle||^2 = ||\hat{U}\,|\Psi\rangle||^2 = \langle\Psi|\,\hat{U}^\dagger\hat{U}\,|\Psi\rangle = |||\Psi\rangle||^2 \ , \tag{2.1.9}$$

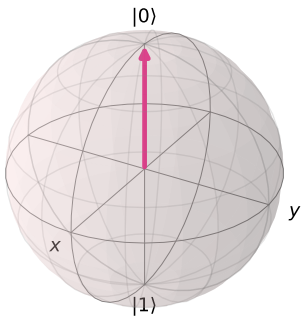


Fig. 2.1: Visualization of the Bloch sphere using the Qiskit quantum programming framework [22]. Any pure single-qubit state can be represented as a point on this sphere, where the north and south poles correspond to the computational basis states $|0\rangle$ and $|1\rangle$, respectively. States on the equator represent equal-population superpositions of the computational basis states with a relative phase defining the azimuthal angle.

therefore the inner products as well as the probabilities and the phase information stored in the coefficients are preserved. One commonly used tool to visualize the quantum state of a single qubit as well as the transformation it undergoes during manipulations is the so-called Bloch sphere, seen in Fig. 2.1. Every action on the qubit can be viewed as a rotation on the Bloch sphere for a certain angle around a specific axis. The geometric Bloch sphere picture follows from the Bloch representation of a qubit state, which holds true for any single-qubit density matrix:

$$\hat{\rho} = \frac{1}{2}(\mathbb{1} + \boldsymbol{a}\cdot\boldsymbol{\sigma}) = \frac{1}{2}\left(\mathbb{1} + \begin{pmatrix} u \\ v \\ w \end{pmatrix} \cdot \begin{pmatrix} \hat{\sigma}_x \\ \hat{\sigma}_y \\ \hat{\sigma}_z \end{pmatrix}\right) = \frac{1}{2}\begin{pmatrix} 1+w & u - i\cdot v \\ u + i\cdot v & 1-w \end{pmatrix} , \tag{2.1.10}$$

where $\boldsymbol{a}$ denotes the Bloch vector specifying the quantum state's position on or inside the Bloch sphere, $(u, v, w)^{\mathrm{T}}$ are its Cartesian components, and $\hat{\sigma}_i$ denote the Pauli matrices [20]. The Pauli matrices:

$$\hat{\sigma}_x = \begin{pmatrix} 0 & 1 \\ 1 & 0 \end{pmatrix} = \hat{X} \qquad \hat{\sigma}_y = \begin{pmatrix} 0 & -i \\ i & 0 \end{pmatrix} = \hat{Y} \qquad \hat{\sigma}_z = \begin{pmatrix} 1 & 0 \\ 0 & -1 \end{pmatrix} = \hat{Z} , \tag{2.1.11}$$

play a central role in quantum mechanics and perform a characteristic dual function: they serve as the fundamental observables of any two-level quantum system and form the generators of all single-qubit unitary operators. Each Pauli matrix is both Hermitian and unitary.

Pure quantum states are represented by Bloch vectors with absolute magnitude of 1, meaning their positions can be found on the surface of the Bloch sphere. Mixed states, on the other hand, lie strictly within the boundaries of the sphere, with the origin of the Bloch sphere describing a maximally mixed qubit state with no preferred direction. A derivation of this circumstance is provided by the purity condition $\hat{\rho}^2 = \hat{\rho}$. Since $\mathrm{Tr}(\hat{\rho}) = 1$ always needs to be fulfilled in a physically meaningful context, for pure qubit states $\|\boldsymbol{a}\| = 1$ is thus enforced. Because the Bloch sphere is a unit sphere and therefore spherically symmetric, it is natural to parameterize the Bloch vector of a pure qubit state in spherical coordinates. In this parametrization, the Bloch vector takes the form:

$$\boldsymbol{a} = \begin{pmatrix} u \\ v \\ w \end{pmatrix} = \begin{pmatrix} \sin(\theta)\,\cos(\phi) \\ \sin(\theta)\,\sin(\phi) \\ \cos(\theta) \end{pmatrix} = \begin{pmatrix} \langle\hat{\sigma}_x\rangle \\ \langle\hat{\sigma}_y\rangle \\ \langle\hat{\sigma}_z\rangle \end{pmatrix} , \tag{2.1.12}$$

with polar angle θ and azimuthal angle ϕ. As indicated in the third line of Eq. 2.1.12 the individual components of the Bloch vector, a_i, equal the expectation value of corresponding Pauli matrix, $\hat{\sigma}_i$, which is true for arbitrary qubit states. The definition of a rotation around a specific axis i by an angle α:

$$\hat{R}_i(\alpha) := \exp(-i\alpha\hat{\sigma}_i/2) = \sum_{n=0}^{\infty} \frac{(-i\alpha\hat{\sigma}_i/2)^n}{n!} , \tag{2.1.13}$$

allows to directly compute the explicit matrix representations of rotations on the Bloch sphere about the three

Cartesian axes. These rotation operators take the following forms:

$$\hat{R}_x(\alpha) = \begin{pmatrix} \cos(\alpha/2) & -i\sin(\alpha/2) \\ -i\sin(\alpha/2) & \cos(\alpha/2) \end{pmatrix} \qquad \hat{R}_y(\beta) = \begin{pmatrix} \cos(\beta/2) & -\sin(\beta/2) \\ \sin(\beta/2) & \cos(\beta/2) \end{pmatrix}$$
$$\hat{R}_z(\gamma) = \begin{pmatrix} e^{-i\gamma/2} & 0 \\ 0 & e^{+i\gamma/2} \end{pmatrix} . \tag{2.1.14}$$

It can be rigorously shown that with this description any arbitrary single-qubit gate operation can be decomposed and expressed as:

$$\begin{aligned} \hat{U} &= e^{i\alpha}\, \hat{R}_z(\phi)\, \hat{R}_y(\theta)\, \hat{R}_z(\lambda) \\ &= e^{i\alpha} \begin{pmatrix} \cos(\theta/2) & -e^{i\lambda}\sin(\theta/2) \\ e^{i\phi}\sin(\theta/2) & e^{i(\phi+\lambda)}\cos(\theta/2) \end{pmatrix} , \end{aligned} \tag{2.1.15}$$

with $\{\phi, \theta, \lambda\}$ being the three so-called Euler angles [20]. Technically one would say that the unitary evolution, $\hat{U}$, ignoring the irrelevant global phase α, is element of a 3D Lie-group embedded in SU(2):

$$\mathrm{SU}(2) = \left\{ \hat{U} \in \mathbb{C}^{2\times 2} | \hat{U}^\dagger \hat{U} = \mathbb{1} \wedge \det(\hat{U}) = 1 \right\} , \tag{2.1.16}$$

with the difference to general unitaries being the additional requirement $\det(\hat{U}) = 1$, which removes physically irrelevant global phases. The special unitary group is particularly convenient because it is a Lie group: it has both the algebraic structure of a group and the smooth structure of a manifold, allowing one to use differential calculus, infinitesimal generators, and other geometric tools in its analysis.

Besides the Pauli operators, one additional single-qubit gate operator of particular relevance, the Hadamard $\hat{H}$, is useful to introduce:

$$\begin{aligned} \hat{H} &= \frac{1}{\sqrt{2}}(\hat{X} + \hat{Z}) = \frac{1}{\sqrt{2}} \begin{pmatrix} 1 & 1 \\ 1 & -1 \end{pmatrix} \\ &= e^{i\pi/2} \hat{R}_z(\pi) \hat{R}_y(\pi/2) . \end{aligned} \tag{2.1.17}$$

The Hadamard operation is a rotation by π around an axis lying in the x–z plane and oriented at 45° relative to both axes. When applied to either computational basis state, it generates an equal superposition of states $|0\rangle$ and $|1\rangle$. Moreover, it naturally functions as a basis transformation:

$$\hat{H}\,|0\rangle_z = \frac{|0\rangle + |1\rangle}{\sqrt{2}} \coloneqq |0\rangle_x = |+\rangle \qquad \hat{H}\,|1\rangle_z = \frac{|0\rangle - |1\rangle}{\sqrt{2}} \coloneqq |1\rangle_x = |-\rangle \ . \tag{2.1.18}$$

Thus the Hadamard gate operator provides the standard superposition required for generating entanglement in many quantum computing experiments as well as in theoretical considerations.

2.1.2 Two-qubit gate operations

For the extension of coherent gate operations to the case of two qubits, the essential principles remain the same: gate operations are still required to be unitary. The only structural difference is the dimensionality of the underlying Hilbert space, which becomes the tensor product of the two single-qubit spaces, resulting in a four-dimensional system. Consequently, any 4×4 unitary matrix represents a valid two-qubit gate operation. Within this space, one may distinguish between local (single-qubit) operations and genuinely entangling two-qubit gate operations:

$$\mathrm{SU}(4) = \left\{ \hat{U} \in \mathbb{C}^{4\times 4} | \hat{U}^\dagger \hat{U} = \mathbb{1} \wedge \det(\hat{U}) = 1 \right\} . \tag{2.1.19}$$

Controlled gate operations such as the C-NOT and the controlled-phase form particularly important representatives of genuinely entangling two-qubit gate operations, as they can be used in combination with single-qubit operations to approximate any unitary operation. A general controlled operation acting on qubits of subsystems A (control) and B (target) can be written as:

$$\hat{C}_{\hat{U}} = |0\rangle\langle 0|_A \otimes \mathbb{1}_B + |1\rangle\langle 1|_A \otimes \hat{U}_B . \tag{2.1.20}$$

For $\hat{U} = \hat{X}$, one obtains the controlled-$\hat{X}$ also known as controlled-not (C-NOT):

$$\hat{C}_{\mathrm{NOT},0\to1} = |0\rangle\langle 0|_A \otimes \mathbb{1}_B + |1\rangle\langle 1|_A \otimes \hat{X}_B = \begin{pmatrix} 1 & 0 & 0 & 0 \\ 0 & 1 & 0 & 0 \\ 0 & 0 & 0 & 1 \\ 0 & 0 & 1 & 0 \end{pmatrix} , \tag{2.1.21}$$

which flips the target qubit if and only if the control qubit is in the state $|1\rangle$. For the choice of $\hat{U} = \hat{Z}$ in Eq. 2.1.20, the expression becomes the controlled-phase operator:

$$\hat{C}_{\mathrm{Phase},0\to1} = |0\rangle\langle 0|_A \otimes \mathbb{1}_B + |1\rangle\langle 1|_A \otimes \hat{Z}_B = \begin{pmatrix} 1 & 0 & 0 & 0 \\ 0 & 1 & 0 & 0 \\ 0 & 0 & 1 & 0 \\ 0 & 0 & 0 & -1 \end{pmatrix} , \tag{2.1.22}$$

that leaves the computational basis invariant except for the state $|11\rangle$, whose amplitude acquires a phase factor of -1.

A set of coherent gate operations that can approximate an arbitrary unitary operation, and thus also a sequence of gate operations, to within an arbitrarily small error ϵ, using only a finite number of repetitions, is referred to as universal gate set. The existence of such sets, and their property of allowing efficient approximation of arbitrary unitaries, is established by the Solovay–Kitaev theorem [23]. For quantum computing, this theorem implies that with a finite set of gate operations any unitary on a finite-dimensional Hilbert space can be approximated, and thus any pure qubit state on the surface of the Bloch sphere can be prepared to arbitrary precision.

Although many different universal gate operation sets exist, the concepts introduced above naturally motivate using the continuous universal gate set as a working example — which is also the set implemented in the experiment. This universal set consists solely of arbitrary single-qubit rotations together with the C-NOT. On the trapped-ion quantum computing platform the C-NOT is synthesized with the controlled-phase operation, as explained in more detail in Sec. 2.6. Because the single-qubit rotations allow continuous control around all three spatial axes, this gate set enables pure quantum states to reach any point on the Bloch sphere exactly. Continuous parameters also provide access to non-Clifford operations, which are essential for achieving quantum computational universality and, ultimately, quantum supremacy.

The need for non-Clifford operations follows from the Gottesman–Knill theorem, which proves that quantum circuits composed exclusively of operations from the Clifford group can be efficiently simulated on a classical computer [24]. The Clifford group consists of all unitary operations that map Pauli operators to Pauli operators under conjugation. Mathematically, it is defined as:

$$\mathcal{C}_n = \left\{ U \in \mathrm{U}(2^n) \,\middle|\, U\mathcal{P}_n U^\dagger = \mathcal{P}_n \right\} , \tag{2.1.23}$$

with $\mathcal{P}_n$ being the Pauli group, $\mathcal{P}_n = \{\pm 1, \pm i\} \times \{\mathbb{1}, \hat{X}, \hat{Y}, \hat{Z}\}^{\otimes N}$. The Clifford group is useful because many relations for Pauli matrices are directly applicable. However, there is no quantum supremacy possible using only these elements and therefore at least one non-Clifford gate operation within the universal gate set is needed to access the power available to quantum computers only.

2.1.3 Entanglement and fidelity

The application of a Hadamard gate operation $\hat{H}$ on the control qubit followed by a C-NOT operation generates a maximally entangled quantum state, more precisely one of the four Bell states $|\Phi^+\rangle$. This process can be visualized with a quantum circuit seen in Fig. 2.2. Mathematically the process can be described as:

$$\begin{aligned} \hat{C}_{\mathrm{NOT},A\to B}\, \hat{H}_A\, |00\rangle_{AB} &= \hat{C}_{\mathrm{NOT},A\to B}\, \hat{H}_A\, |0\rangle_A \otimes |0\rangle_B \\ &= \hat{C}_{\mathrm{NOT},A\to B} \left(\frac{|0\rangle_A + |1\rangle_A}{\sqrt{2}} \otimes |0\rangle_B \right) \\ &= \frac{|00\rangle_{AB} + |11\rangle_{AB}}{\sqrt{2}} =: |\Phi^+\rangle \ . \end{aligned} \tag{2.1.24}$$

The single qubits correspond to the subsystems A and B, which together form the Hilbert space of the composite bipartite system $\mathscr{H}_{AB} = \mathscr{H}_A \otimes \mathscr{H}_B$. The principle behind creating this Bell state can be extended

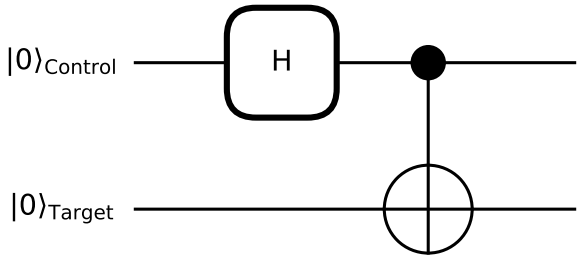


Fig. 2.2: Quantum circuit for preparing the Bell state $|\Phi^+\rangle$ using a Hadamard $\hat{H}$ on the control qubit followed by a C-NOT gate operation. The circuit was drawn using the PennyLane quantum programming framework for Python [25].

to N qubits without any obstacles by adding as many $C_{\mathrm{NOT},A\to q_N}$ operations as subsystems are added. In a bipartite system, a pure state is called entangled if it cannot be written as a product state:

$$|\Psi\rangle_{AB} \neq |\Psi\rangle_A \otimes |\Psi\rangle_B \ . \tag{2.1.25}$$

The degree of entanglement, for pure bipartite quantum systems, is quantified by the so-called Schmidt decomposition, which always exists for pure states:

$$|\Psi\rangle_{\mathrm{Pure}} = \sum_{m=1}^{r} \lambda_m \ |i_m\rangle_A \otimes |j_m\rangle_B \ . \tag{2.1.26}$$

The Schmidt decomposition is a sum over orthonormal basis pairs $|i_m\rangle_A$ and $|j_m\rangle_B$ with non-negative real coefficients λ_m. The number of non-zero Schmidt coefficients, given by the magnitude of r, is the so-called Schmidt rank and satisfies $r \leq \min(\dim_{\mathbb{C}}(\mathcal{H}_{\mathrm{A}}), \dim_{\mathbb{C}}(\mathcal{H}_{\mathrm{B}}))$. The pure bipartite state is entangled if and only if $r > 1$, which is equivalent to the statement of definition given in Eq. 2.1.25. The squared Schmidt coefficients λ_m^2 are the eigenvalues of the reduced density matrices $\hat{\rho}_A = \hat{\rho}_{AB|B} = \mathrm{Tr}_B(\hat{\rho}_{AB})$ and $\hat{\rho}_B = \hat{\rho}_{AB|A} = \mathrm{Tr}_A(\hat{\rho}_{AB})$, which completely quantify entanglement for pure states. The pure bipartite state is maximally entangled if its Schmidt rank reaches the maximum value allowed by the subsystem dimensions, $r = \min(\dim_{\mathbb{C}}(\mathcal{H}_{\mathrm{A}}), \dim_{\mathbb{C}}(\mathcal{H}_{\mathrm{B}}))$, and all Schmidt coefficients are equal and given by $\lambda_m = 1/\sqrt{r}$.

Equivalently, for a maximally entangled pure bipartite state, the reduced density matrices are maximally mixed, i.e. $\hat{\rho}_A \propto \mathbb{1}_A$ and $\hat{\rho}_B \propto \mathbb{1}_B$, which means that each subsystem, considered individually, carries no information about the total state. Nevertheless, measurements performed on one subsystem determine the corresponding outcome on the other subsystem with perfect correlations, even though each local result is individually completely random. One says, in the context of maximally entangled quantum states, that the information is de-localized. Genuinely quantum phenomena such as entanglement and interference of entangled states enable quantum computers to explore and exploit the full structure of the Hilbert space $\mathscr{H}_{\mathrm{total}}$ in ways that are inaccessible to classical devices, potentially providing drastic reductions in computational resources for certain kinds of problems.

For pure systems partitioned into more than two subsystems, i.e. pure multipartite systems, the Schmidt decomposition does not, in general, provide a complete characterization of entanglement, since it applies only to bi-partitions of the total state. Instead, one typically analyzes entanglement across all relevant bi-partitions via corresponding reduced density matrices. Furthermore, the degree of entanglement of multipartite systems cannot be described by one single quantity, but is described by classes of genuine multipartite entanglement, which are defined by transformations under stochastic local operations and classical communication (SLOCC). For a more rigorous treatment of pure multipartite system entanglement the reader is referred to Ref. [26].

For mixed states, entanglement is defined analogously: a bipartite density operator is entangled if it cannot be written as a classical mixture of product states:

$$\hat{\rho}_{AB} = \sum_k p_k \cdot \hat{\rho}_A^{(k)} \otimes \hat{\rho}_B^{(k)} \qquad \text{, with } p_k \geq 0 \wedge \sum_k p_k = 1 \ . \tag{2.1.27}$$

However, the quantification of entanglement in mixed states is significantly more complex, since mixedness may arise not only from quantum correlations but also from classical statistical uncertainty.

In realistic experimental settings, quantum operations cannot be implemented with perfect accuracy. The deviation of the experimentally obtained final state from the theoretically intended target state can be quantified using the fidelity. The most general formulation is given by the Uhlmann fidelity, which assumes arbitrary mixed states for both the experimentally prepared state, $\hat{\rho}$, and the intended target state, $\hat{\varsigma}_{\text{Target}}$ [20]:

$$F(\hat{\rho}, \hat{\varsigma}_{\text{Target}}) = \left(\text{Tr} \sqrt{\sqrt{\hat{\rho}}\, \hat{\varsigma}_{\text{Target}}\, \sqrt{\hat{\rho}}} \right)^2 . \tag{2.1.28}$$

In most experimental scenarios, however, the target state is well described as a pure state $|\Psi\rangle$. In this case, the Uhlmann fidelity defined in Eq. 2.1.28 reduces to:

$$F(\hat{\rho}, |\Psi\rangle_{\text{Target}}) = \langle \Psi | \hat{\rho} | \Psi \rangle . \tag{2.1.29}$$

While the Uhlmann fidelity, and its reduced form for pure target states, quantify the full state overlap including both population and coherence, direct experimental determination in a single measurement is not feasible. Instead, quantum state tomography must be performed, in which the state is re-prepared and measured repeatedly in multiple bases in order to reconstruct the full density matrix [20]. For Greenberger–Horne–Zeilinger (GHZ)-type target states of the form:

$$|\text{GHZ}\rangle = \frac{|0 \ldots 0\rangle + |1 \ldots 1\rangle}{\sqrt{2}} , \tag{2.1.30}$$

the fidelity can instead be estimated from population measurements and parity oscillations. For this class of states, the total fidelity estimator can be written as:

$$\mathcal{F}_{\text{total}} = \frac{1}{2} \left(\mathcal{F}_{\text{population}} + \mathcal{F}_{\text{parity}} \right) . \tag{2.1.31}$$

For the parity contribution $\mathcal{F}_{\text{parity}}$, the final state $\hat{\rho}$ is re-prepared and a collective $\pi/2$ analysis pulse is applied to all qubits. For the two-qubit case considered here, the rotated state is given by [1]:

$$\hat{\rho}'(\phi) = \hat{R}_\phi \left(\frac{\pi}{2} \right)^{\otimes 2} \hat{\rho}\, \hat{R}_\phi^\dagger \left(\frac{\pi}{2} \right)^{\otimes 2} . \tag{2.1.32}$$

The phase ϕ of this analysis pulse determines the rotation axis in the equatorial plane of the Bloch sphere:

$$\hat{R}_\phi \left(\frac{\pi}{2} \right) = \exp\left[-i \frac{\pi}{4} \left(\cos(\phi)\, \hat{\sigma}_x + \sin(\phi)\, \hat{\sigma}_y \right) \right] . \tag{2.1.33}$$

The parity operator is defined, in general for N qubits, as:

$$\hat{\Pi} = \bigotimes_{k=1}^{N} \hat{\sigma}_z^{(k)} , \tag{2.1.34}$$

which characterizes definite parity of a quantum state when it fulfills the eigenvalue equation $\hat{\Pi}\,|\Psi\rangle = \pm\,|\Psi\rangle$. The expectation value of the parity operator is measured as a function of the analysis-pulse phase ϕ. The resulting parity oscillation maps the coherence between the two components of the Bell state onto measurable even- and odd-parity populations, which contribute with corresponding eigenvalues of $+1$ and -1, respectively:

$$\langle \hat{\Pi} \rangle = P_{00} + P_{11} - P_{01} - P_{10} . \tag{2.1.35}$$

A scan of the analysis-pulse phase produces therefore an oscillation between even- and odd-parity contributions after the analysis pulse. For the two-qubit case, the parity signal is given by [15]:

$$\begin{aligned} \langle \hat{\Pi}(\phi) \rangle &= \text{Tr}\left[\hat{\Pi}\, \hat{R}_\phi \left(\frac{\pi}{2} \right)^{\otimes 2} \hat{\rho}\, \hat{R}_\phi^\dagger \left(\frac{\pi}{2} \right)^{\otimes 2} \right] \\ &= C \cos(2\phi + \phi_0) . \end{aligned} \tag{2.1.36}$$

[1] Parity oscillations can also be obtained by applying $\hat{R}_x(\theta)$ rotations instead, with the rotation angle θ used as the continuous scan variable.

Here, C denotes the parity-oscillation contrast, while the phase offset ϕ_0 depends on the phase convention of the prepared Bell state as well as of the analysis pulse. The contrast reveals the magnitude of the relevant off-diagonal density-matrix elements and thereby quantifies the coherence between the two Bell-state components. A contrast value of $C = 1$ corresponds to full coherence and an ideal Bell state. For the specific target state $|\Phi^+\rangle$, the total fidelity estimator becomes:

$$\mathcal{F}_{\text{total}} = \frac{1}{2}\big(P_{00} + P_{11} + C\big) \,, \tag{2.1.37}$$

where P_{00} and P_{11} denote the populations of the desired even-parity basis states. The population probabilities are obtained from the measurement outcomes according to Eq. 2.1.7:

$$P_{ii} = \langle ii|\hat{\rho}|ii\rangle = \mathrm{Tr}(\hat{\rho}\,|ii\rangle\,\langle ii|) = \frac{N_{ii}}{N_{\text{shots}}} \,. \tag{2.1.38}$$

Together, the population term verifies that the state occupies the desired computational-basis components, while the parity-oscillation contrast confirms that these components are coherently superposed.

2.2 Optical concepts

In this section, the reader is familiarized with several optical concepts that are essential for understanding and describing the work presented in this thesis. In particular, the fields of Gaussian optics, the Jones formalism, and the Nijboer–Zernike diffraction theorem are introduced.

2.2.1 Gaussian optics

The fundamental Gaussian beam corresponds to the lowest-order solution of the paraxial Helmholtz equation:

$$\nabla_\perp^2 E + 2ik\frac{\partial E}{\partial z} = 0 \,, \qquad \nabla_\perp^2 := \left(\frac{\partial^2}{\partial x^2} + \frac{\partial^2}{\partial y^2}\right), \tag{2.2.1}$$

where $E(x, y, z)$ denotes the scalar electric-field envelope and $k = 2\pi n/\lambda$ is the wavenumber corresponding to the wavelength λ in a medium with refractive index n. A detailed derivation of this lowest-order paraxial solution is presented in Ref. [27], in which it is shown that the field can be written as:

$$E(x, y, z) = E_0\,\frac{w_0}{w(z)}\exp\!\left(-\frac{r^2}{w(z)^2}\right)\exp\!\left(-i\left[kz + \frac{kr^2}{2R(z)} - \zeta(z)\right]\right). \tag{2.2.2}$$

with E_0 being the complex field amplitude, $w(z)$ the beam radius at propagation distance z, and w_0 the minimum beam radius, referred to as the beam waist. Furthermore, $r^2 = x^2 + y^2$ defines the radial coordinate, $R(z)$ denotes the wavefront curvature, and $\zeta(z)$ represents the Gouy phase, which is absent for plane waves. From geometrical considerations, the Rayleigh length is obtained as:

$$z_R = \frac{1}{2}\,\frac{k w_0^2}{M^2} = \frac{\pi w_0^2}{M^2 \lambda}, \tag{2.2.3}$$

where M^2 denotes the beam quality factor, with $M^2 = 1$ corresponding to an ideal Gaussian beam. The Rayleigh length characterizes the beam divergence and corresponds to the propagation distance at which the beam radius increases from w_0 to $\sqrt{2}\,w_0$. Using this definition of Eq. 2.2.3, the beam radius can be written in compact form as:

$$w(z) = w_0\sqrt{1 + \left(\frac{z}{z_R}\right)^2} \,. \tag{2.2.4}$$

If the paraxial Helmholtz equation is separable, such that:

$$E(x, y, z) = u_n(x, z) \cdot u_m(y, z) \,, \tag{2.2.5}$$

higher-order solutions than the fundamental mode can be derived. Depending on the type of coordinates used to describe Eq. 2.2.1, the Laguerre-Gaussian beams (spherical coordinates), or the Hermite-Gaussian beams

(Cartesian coordinates) are obtained [28, 29]. The Hermite-Gaussian modes that are relevant for this work, take the following form of field distributions (up to the phase evolution of the propagating beams):

$$E_{nm}(x,y,z) \propto E_0 \frac{w_0}{w(z)} H_n\left(\frac{\sqrt{2}x}{w(z)}\right) H_m\left(\frac{\sqrt{2}y}{w(z)}\right) \exp\left(-\frac{x^2+y^2}{w(z)^2}\right) . \tag{2.2.6}$$

The Hermite polynomials, $H_{n/m}$, create the distributions according to the specific Hermite-Gaussian mode. When both the electric and magnetic fields oscillate perpendicular to the direction of propagation, the field distribution is referred to as a transverse electromagnetic ($\mathrm{TEM_{nm}}$) mode [30]. This theoretical description implies for the Hermite-Gaussian $\mathrm{TEM_{10}}$ mode a field distribution proportional to:

$$\begin{aligned} E_{10}(x,y,z) &\propto E_0 \frac{w_0}{w^2(z)} H_1\left(\frac{\sqrt{2}x}{w(z)}\right) H_0\left(\frac{\sqrt{2}y}{w(z)}\right) \exp\left(-\frac{x^2+y^2}{w(z)^2}\right) \\ &= E_0 \frac{w_0}{w^2(z)} \sqrt{2}x \exp\left(-\frac{x^2+y^2}{w(z)^2}\right) \end{aligned} \tag{2.2.7}$$

For an arbitrary Hermite–Gaussian $\mathrm{TEM_{nm}}$ mode, a general relation can be derived that connects its waist size to that of the fundamental $\mathrm{TEM_{00}}$ mode [30]:

$$w_{n,m}(z) = w(z) \cdot \sqrt{2n+1} \cdot \sqrt{2m+1} = w_0 \cdot \sqrt{1+\left(\frac{z}{z_R}\right)^2} \cdot \sqrt{2n+1} \cdot \sqrt{2m+1} . \tag{2.2.8}$$

Another formula describing the resulting, final waist size w_{fin}, when a beam with initial waist w_{ini} is focused down by a focusing lens of focal length f, is given by [27]:

$$w_{\mathrm{fin}} = \frac{\lambda f}{\pi w_{\mathrm{ini}}} . \tag{2.2.9}$$

A Gaussian beam cannot be focused arbitrarily tightly, but is fundamentally limited by diffraction due to the finite aperture of the focusing optics. For an optical system with a circular aperture, the diffraction limit is commonly characterized by the Airy disk, which arises from the diffraction of a uniformly illuminated aperture [31]. The minimal achievable spot size is therefore bounded by the Airy disk diameter, given by:

$$d_{\mathrm{min}} = 1.22 \frac{\lambda}{n \sin(\theta)} = 1.22 \frac{\lambda}{\mathrm{NA}}, \tag{2.2.10}$$

where $\mathrm{NA} = n \sin(\theta)$ defines the numerical aperture. The NA characterizes the maximum acceptance angle and thus the focusing capability of the optical system. Small diffraction-limited spot sizes can be achieved using collimated beams together with high-NA systems that are fully illuminated across the entrance aperture. A collimated beam is characterized by a negligibly small angular divergence and approximately planar wavefronts.

2.2.2 Jones formalism

A formal description of linear polarization optics is provided by the Jones matrix formalism, also referred to as Jones calculus. Within this framework, the Jones vector $\boldsymbol{J}$ represents the complex amplitudes of the two orthogonal transverse components of a monochromatic plane wave propagating along the z-direction. The definition of the Jones vector follows from writing the electric field $\mathbf{E}$ as:

$$\mathbf{E}(z,t) = \begin{pmatrix} E_x\, e^{i(kz-\omega t+\phi_x)} \\ E_y\, e^{i(kz-\omega t+\phi_y)} \end{pmatrix} = \begin{pmatrix} E_x e^{i\phi_x} \\ E_y e^{i\phi_y} \end{pmatrix} e^{i(kz-\omega t)} = \begin{pmatrix} \tilde{E}_x \\ \tilde{E}_y \end{pmatrix} e^{i(kz-\omega t)} := \boldsymbol{J}\, e^{i(kz-\omega t)} , \tag{2.2.11}$$

where $\tilde{E}_x$ and $\tilde{E}_y$ denote the complex field amplitudes of the transverse electric-field components. Different polarization states are described by the corresponding entries of the Jones vector, as illustrated by the following normalized examples:

$$|\mathrm{H}\rangle = \begin{pmatrix} 1 \\ 0 \end{pmatrix} \text{, linear x} \qquad |\mathrm{V}\rangle = \begin{pmatrix} 0 \\ 1 \end{pmatrix} \text{, linear y} \qquad |\mathrm{R}\rangle = \frac{1}{\sqrt{2}} \begin{pmatrix} 1 \\ -i \end{pmatrix} \text{, right-handed circular .} \tag{2.2.12}$$

With corresponding Jones matrices M_i for different optical elements i one can calculate the resulting field of the plane wave:

$$\boldsymbol{E}(z,t)_{\mathrm{resulting}} = M_i \cdot \boldsymbol{E}(z,t)_{\mathrm{initial}} . \tag{2.2.13}$$

The Jones matrices for H and V polarization filters as well as for a general δ-phase-retarding wave plate are given by:

$$\underbrace{\begin{pmatrix} 1 & 0 \\ 0 & 0 \end{pmatrix}}_{\text{H pol. filter}} \qquad \underbrace{\begin{pmatrix} 0 & 0 \\ 0 & 1 \end{pmatrix}}_{\text{V pol. filter}} \qquad \underbrace{\begin{pmatrix} 1 & 0 \\ 0 & e^{i\delta} \end{pmatrix}}_{\delta\text{-retarding wave plate}} \quad . \tag{2.2.14}$$

Together with a rotatable mount the δ-phase-retardation enables the control of the output after a polarizing beam splitter cube (PBC).

2.2.3 Nijboer-Zernike diffraction theorem

As a final optical concept, the Nijboer–Zernike diffraction theorem is introduced. Within this framework, an infinite set of even and odd Zernike polynomials forms an orthogonal basis on a two-dimensional pupil function, such as that of a lens. These polynomial basis functions are used to quantify optical aberrations, which may arise due to defects or misalignment of optical elements [32]. An aberration-free image is obtained when all Zernike coefficients vanish except for the lowest-order term. This first basis function corresponds to a uniform phase offset and describes a light field that propagates through the lens without distortion. The Zernike polynomials $Z_n^m(\rho, \phi)$, defined as:

$$Z_n^m(\rho, \phi) := \begin{cases} R_n^m(\rho)\, \cos(m\phi), & \text{for} \quad m \geq 0 \\ R_n^{|m|}(\rho)\, \sin(|m|\phi), & \text{for} \quad m < 0 \ , \end{cases} \tag{2.2.15}$$

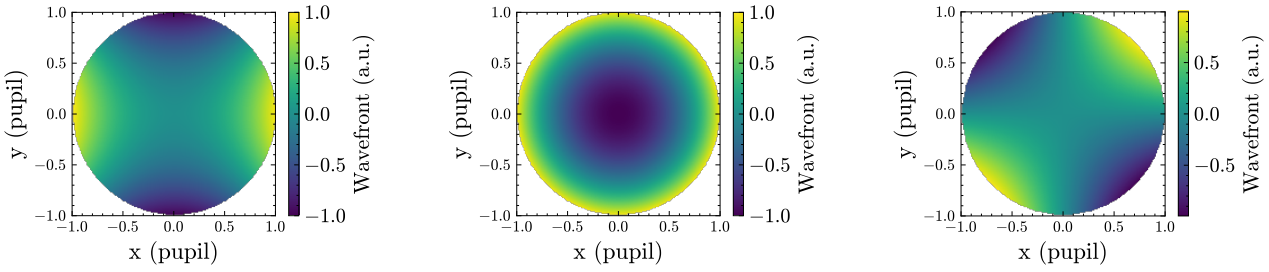
depend on the radial coordinate ρ, which for the normalized case equals 1 for the edge of the pupil, on the angular (azimuthal) coordinate ϕ, which relates the angle with respect to the optical axis in radians, on the radial order n controlling the number of radial oscillations, on the azimuthal order m determining the number of angular lobes, and on the radial Zernike polynomials R_n^m, which are given by:

$$R_n^m(\rho) = \sum_{k=0}^{\frac{n-m}{2}} (-1)^k \frac{(n-k)!}{k!\, \left(\frac{n+m}{2} - k\right)!\, \left(\frac{n-m}{2} - k\right)!} \rho^{n-2k} \ . \tag{2.2.16}$$

The radial order n must be an even, non-negative integer, whereas the azimuthal order must satisfy:

$$|m| \leq n \qquad \text{with} \qquad n - |m| = \text{even integer} \ , \tag{2.2.17}$$

and may be negative. The visualization of the total Zernike polynomials $Z_n^m(\rho, \phi)$ of second radial order, $n = 2$, can be seen in Fig. 2.3. Higher radial orders of the Zernike polynomials include aberrations due to coma and spherical distortions.



(a) (b) (c)

Fig. 2.3: Second radial-order Zernike polynomials $Z_n^m(\rho, \phi)$ representing low-order wavefront aberrations. The functions are displayed on the normalized circular aperture, and the color scale denotes the relative optical path difference. (a) astigmatism (Z_2^2), which results from different curvature along orthogonal pupil axes and produces two line-shaped focus spots in perpendicular orientations; (b) defocus (Z_2^0), introducing a uniform radial curvature and thereby shifting the best-focus position symmetrically; (c) astigmatism (Z_2^{-2}), identical in origin and physical effect to (a), but rotated by 45° in spatial orientation.

2.3 Paul trap and general trapping procedure

The radio-frequency (RF) trap, or multipole trap, is commonly known as the Paul trap, in honor of Wolfgang Paul. In the 1950s, he and his co-workers developed the device and realized ion trapping for the first time worldwide. For this invention, he was awarded a shared Nobel prize in 1989 [33]. This achievement enables physicists today to use individually trapped ions as qubits, a concept that was once considered unfeasible. The following subsections introduce the theory behind RF trapping as well as aspects of its physical realization.

2.3.1 Paul trap

Both electrostatic and electrodynamic laws must be satisfied for successful trapping of charged particles. This condition implies that Maxwell's equations, which constitute the fundamental framework of classical electromagnetism, must hold throughout the trapping region. Of particular relevance in this context is the first Maxwell equation, commonly referred to as Gauss's law and originally formulated by Karl Friedrich Gauss [34]. Gauss's law is presented here in its differential form:

$$\nabla \cdot \mathbf{E} = \frac{\rho}{\epsilon_0} \ . \tag{2.3.1}$$

The first Maxwell equation identifies the cause of an electric field $\mathbf{E}$ to be charges, or more specifically the spatial distribution of charges ρ. In the original works of Gauss, the vacuum permittivity ϵ_0 did not appear, but was added later by Maxwell in the 1860s to uniform electrodynamics, electrostatics, and the units used therein. Gauss' law is the foundation for Coulomb's law and together with it, the whole of electrostatics. Considering the relation between the electric gradient field $\mathbf{E}$ and its scalar potential Φ, given by:

$$-\nabla\Phi = \mathbf{E} \ , \tag{2.3.2}$$

as well as the Gauss law itself, Eq. 2.3.1, one recovers the Poisson equation of electrostatics:

$$\nabla \cdot \mathbf{E} = -\nabla^2\Phi = \underbrace{-\Delta\Phi = \frac{\rho}{\epsilon_0}}_{\text{Poisson equation}} \ . \tag{2.3.3}$$

In the case of using electrostatic fields alone to attempt trapping charged particles, the electrostatic scalar field-potential Φ must obey Laplace's equation of electrostatics:

$$-\Delta\Phi = 0 \ , \tag{2.3.4}$$

everywhere except at the exact position of the electrically charged particle to be trapped. The Laplace equation of electrostatics is a special case of Poisson's equation with vanishing charge density, $\rho = 0$, which applies inside an ion trap apart from the negligible contribution of the trapped ion itself, such that the shape of the electrostatic trapping field is essentially determined by the trapping electrodes alone. As a consequence, a three-dimensional electrostatic trapping potential cannot exhibit local extrema in free space, since Laplace's equation requires the sum of the second spatial derivatives to vanish:

$$-\Delta\Phi = 0 \iff \left(\frac{\partial^2}{\partial x^2} + \frac{\partial^2}{\partial y^2} + \frac{\partial^2}{\partial z^2}\right)\Phi = 0 \ , \tag{2.3.5}$$

implying that at least one curvature must have the opposite sign to the others. Only saddle points are therefore possible. A stable trapping point or region, however, would require a potential minimum with a finite depth such that a restoring force acts in all spatial directions when the ion is displaced from equilibrium. Consequently, trapping ions using electrostatic potentials alone is not possible. These considerations were already addressed by Samuel Earnshaw, who combined the theoretical foundations established by Laplace and Gauss to formulate what is now known as Earnshaw's theorem, proving the impossibility of stable ion trapping with static electric fields alone.

There are multiple approaches by which ion trapping can be realized, such as the Penning trap, which employs a combination of static electric potentials and a static magnetic field. The design of a Penning trap, however, often limits optical access to the ions and imposes additional experimental challenges [35, 36, 37]. For this reason, the Paul (RF) trap is preferred for most applications. The linear Paul trap, which is discussed in detail in the following, employs a static electric potential along the axial direction and time-dependent electric fields (RF multipole potentials) in the remaining two dimensions, which by symmetry define the radial directions.

The Paul trap exploits what Laplace's equation does not prohibit: although only saddle points and no static extrema are allowed, a saddle potential may rotate in time. At an appropriate rotation frequency, the trapped ion experiences a time-averaged, effective harmonic confinement in the radial direction. Since this effective potential approximates a static harmonic potential that is forbidden by electrostatics alone, it is commonly referred to as a pseudopotential, as illustrated in Fig. 2.4.

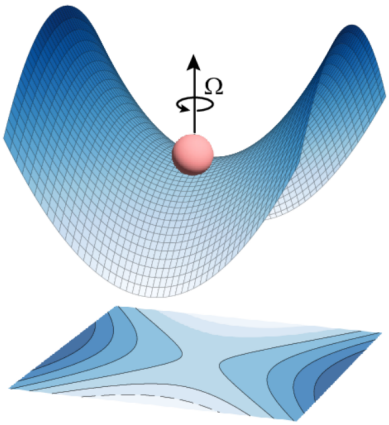


Fig. 2.4: Instantaneous RF quadrupole saddle potential of a linear Paul trap, rotating at the drive frequency Ω_{RF} around a single trapped ion. The corresponding 2D contour representation of the same potential in the radial plane is shown below the saddle potential. Time-averaging of this rapidly rotating saddle results in the RF pseudo-potential that provides the radial confinement. Illustration taken from [38].

A truly rotating saddle potential in the radial trapping plane can be described by:

$$\Phi_{\text{rot}}(\boldsymbol{r}, t) = \frac{V_{RF}}{2r_0^2} \left[\sin(\Omega_{\text{rot}} t) \cdot (x^2 - y^2) + 2xy \cdot \cos(\Omega_{\text{rot}} t)\right] , \tag{2.3.6}$$

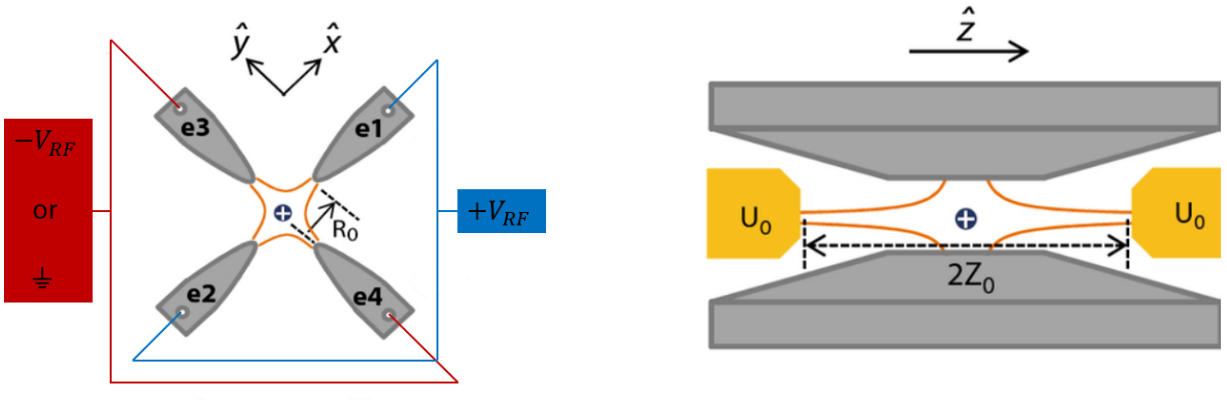
where V_{RF} denotes the applied RF voltage amplitude, r_0 is the characteristic radial electrode distance, and Ω_{rot} is the angular rotation frequency of the saddle potential [39]. This potential corresponds to a quadrupolar field whose principal axes rotate continuously in the radial plane.

In a linear Paul trap, by contrast, the electrode geometry is fixed in space and no physical rotation of the saddle potential occurs. Instead, radial confinement is generated by a time-periodic modulation of a quadrupole potential, such that the potential curvature is modulated along the two radial directions. While the confinement strength along one radial axis is reduced, the confinement along the orthogonal axis is increased. This alternating modulation leads to a time-dependent oscillation of the radial potential, often described as a "flapping" motion. At all times, the potential retains a quadrupolar form, with a curvature whose sign alternates between the two radial axes. The radial contribution to the total trapping potential is therefore described by a sinusoidal time dependence of the quadrupolar term:

$$\Phi(\boldsymbol{r}, t) = \frac{V_{RF}}{2r_0^2} \sin(\Omega t) \cdot (x^2 - y^2) + \frac{U_0}{2z_0^2} \cdot (2z^2 - x^2 - y^2) , \tag{2.3.7}$$

where U_0 denotes the static voltage applied to the axial electrodes, z_0 is the characteristic axial electrode spacing, and Ω is the drive frequency of the RF quadrupole potential [40]. Both the rotating and the oscillating saddle potentials lead, in a time-averaged sense, to an effective harmonic confinement of the ion. The pseudopotential approximation is valid in either case provided that the ion motion can be separated into a rapidly oscillating motion (micromotion) and a slower one (secular motion). Under this condition, the detailed temporal structure of the saddle potential becomes irrelevant for the effective confinement. For a more comprehensive discussion of the pseudopotential regime, the reader is referred to Refs. 41, 38.

Fig. 2.5 shows a schematic of a linear RF trap in all three spatial dimensions with the relevant geometrical parameters for the theoretical description indicated therein. The four RF blades, labeled $e1$ to $e4$, are connected pairwise. In many implementations, only one pair of blades is driven by an RF voltage, while the opposing pair is either held at ground potential or biased with a static voltage. If the second pair is grounded, the RF-driven blades induce a mirrored charge distribution on the grounded electrodes. Since the blades and their mechanical mounts can only be fabricated within finite machining tolerances, a small residual mechanical asymmetry is generally present, which leads to deviations from an ideal quadrupole field. Such asymmetries, and the resulting imbalance in the radial trapping frequencies, can be partially compensated by applying a static offset voltage to the second blade pair instead of grounding it.



(a) (b)

Fig. 2.5: Schematic of a linear Paul trap with RF blades (adapted from Ref. [42]). (a): Axial perspective of the trap, showing the wiring configuration between the electrode blade pairs (e1–e2 and e3–e4), along with the applied potential possibilities and the radial electrode distance parameter r_0. (b): Radial perspective, illustrating the axial electrode spacing parameter z_0. Specific parameter values relevant to the experiment are $r_0 = 0.57(1)\,\mathrm{mm}$ and $z_0 = 2.25(4)\,\mathrm{mm}$.

The confining, static potential along the axial (z) direction takes for a linear Paul trap a harmonic form:

$$\Phi(z) = +U_0 \left(\frac{z}{z_0}\right)^2 , \tag{2.3.8}$$

with $+U_0$ being the applied voltage to the end-cap electrodes and z_0 the characteristic axial length of the trap. The potential energy of an ion in the trap, with respect to the axial dimension, is given by the product of the charge e and the potential itself, $E_{pot}(z) = e \cdot \Phi(z)$. The resulting force is the negative derivative of the potential energy:

$$F(z) = -\frac{dE_{pot}(z)}{dz} = -e\frac{d\Phi(z)}{dz} = -\frac{2eU_0}{z_0^2} z, \tag{2.3.9}$$

combined with Newtons second law, $F(z) = m\ddot{z}$, and the knowledge about the ion's mass m, one can derive the axial trap frequency:

$$0 = \ddot{z} + \underbrace{\frac{2eU_0}{mz_0^2}}_{=\omega_{axial}^2} z \quad \Longrightarrow \quad \omega_{axial} = \sqrt{\frac{2eU_0}{mz_0^2}} . \tag{2.3.10}$$

The coupled equations of motion of multiple trapped ions cannot be diagonalized in their original coordinates. Instead, the system is transformed into a set of independent collective coordinates by decomposing the motion into normal modes. In the axial spatial dimension, this procedure yields N independent equations for a chain of N ions, each corresponding to a collective axial normal mode with a characteristic oscillation frequency ω_j ($j = 1, \ldots, N$). The harmonic axial confinement of the trap causes these collective modes to be harmonically quantized, such that each axial mode is described by a quantum harmonic oscillator with discrete energy eigenstates [43]. Fig. 2.6 shows the energetically lowest axial eigenmodes of oscillation for three ions.

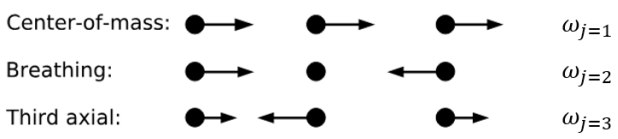


Fig. 2.6: Lowest energetic normal oscillation modes for 3 ions. Adapted from [15].

For the radial confinement, which is governed by a time-dependent oscillating quadrupole field, an equivalent approach can be taken. Owing to the symmetry of the two radial directions, which differ only by a sign, the following considerations are restricted to a single representative dimension without loss of generality. The time-dependent potential along the x direction then reads:

$$\Phi(x) = \frac{1}{2}\left(\frac{-U_0}{z_0^2} + \frac{V_{RF}\sin(\Omega t)}{x_0^2}\right)x^2 \ , \tag{2.3.11}$$

with $x_0 \equiv r_0$ being the radial electrode distance parameter in the simplified 1-dimensional case. The potential energy of an ion with the charge $+e$ in respect to the x-dimension equals $\mathrm{E}_{pot}(x) = e\Phi(x)$. The resulting force is given by the negative gradient of the potential multiplied with the charge:

$$F(x) = -e \cdot \frac{d\Phi(x)}{dx} = -e\left(\frac{U_0}{z_0^2} - \frac{V_{RF}\sin(\Omega t)}{x_0^2}\right)x \ , \tag{2.3.12}$$

from which using Newton's second law again and after rearranging, the equation of motion with respect to the radial dimension is derived:

$$\ddot{x} + \frac{e}{m}\left(\frac{-U_0}{z_0^2} + \frac{V_{RF}\sin(\Omega t)}{x_0^2}\right)x = 0 \ . \tag{2.3.13}$$

Thus, the radial motion is governed by the Mathieu equations [44]. For this class of equations, no closed-form analytical solution exists for the general case. Instead, their behavior is commonly analyzed using numerical simulations or suitable analytical approximations. One such approach is the secular approximation, which separates the equation of motion into a rapidly oscillating component driven by the RF potential and a slowly varying component associated with the effective spatial confinement. This procedure effectively decomposes the ion motion into two distinct contributions:

$$x(t) = \underbrace{\bar{x}(t)}_{\text{slow}} + \underbrace{\zeta(t)}_{\text{fast}} \ . \tag{2.3.14}$$

Without loss of generality the static axial potential may be set to zero, $U_0 = 0$. The ion's position changes only incrementally small during a fast RF-oscillation, so that one can neglect the spatial dependency and solve directly for the fast part $\zeta(t)$. The solution:

$$\zeta(t) = \frac{eV_{RF}}{m\Omega^2 x_0^2}\bar{x}(t)\sin(\Omega t) \ , \tag{2.3.15}$$

describes the equation of motion caused by the rapidly oscillating RF-field with frequency Ω, which is commonly referred to as micromotion. For the solution of the slow dynamics, $\bar{x}(t)$, the secular approximation assumes a regime where the micromotion averages out over time. With the addition of Newton's second law, one can solve the whole problem:

$$\begin{aligned}
\bar{F}(x_t) = \langle F(x_t)\rangle &= \left\langle \frac{-eV_{RF}}{x_0^2}[\bar{x} + \zeta(t)]\sin(\Omega t)\right\rangle \\
&= -\frac{eV_{RF}}{x_0^2}\bar{x}\ \underbrace{\langle\sin(\Omega t)\rangle}_{=0} - \frac{eV_{RF}}{x_0^2}\frac{eV_{RF}}{m\Omega^2 x_0^2}\bar{x}\ \underbrace{\langle\sin^2(\Omega t)\rangle}_{=1/2} \\
&= -\frac{e^2V_{RF}^2}{2m\Omega^2 x_0^4}\bar{x} = m\ddot{\bar{x}} \implies \omega_{\text{sec}} = \frac{eV_{RF}}{\sqrt{2}m\Omega x_0^2} =: \frac{q}{\sqrt{8}}\Omega \ .
\end{aligned} \tag{2.3.16}$$

The overall solution for the radial dimension yields the slow, secular frequency ω_{sec}, also known as the macromotion frequency. In the last line of Eq. 2.3.16, the dimensionless Mathieu q-parameter is introduced, which is written out explicitly in Eq. 2.3.18 and explained in more detail thereafter. It follows for the radial equation of the ion motion, represented in general in Eq. 2.3.14, the solution:

$$\bar{x} = x_0\sin(\omega_{sec}t) \implies x(t) = x_0\sin(\omega_{sec}t)\cdot\left(1 + \frac{eV_{RF}}{m\Omega^2 x_0^2}\sin(\Omega t)\right). \tag{2.3.17}$$

For a chain of N ions confined in a linear Paul trap, the full motional spectrum consists of $3N$ normal modes. These comprise $2N$ modes associated with the radial trap dimensions, whose classical dynamics are governed by Mathieu equations due to the time-dependent RF confinement, and an additional N modes along the axial trap direction.

The secular approximation and the resulting solution for the radial ion trajectory can be used for a direct comparison between the full ion motion and the secular motion alone can be made in the radial trapping plane. Fig. 2.7 illustrates this comparison.

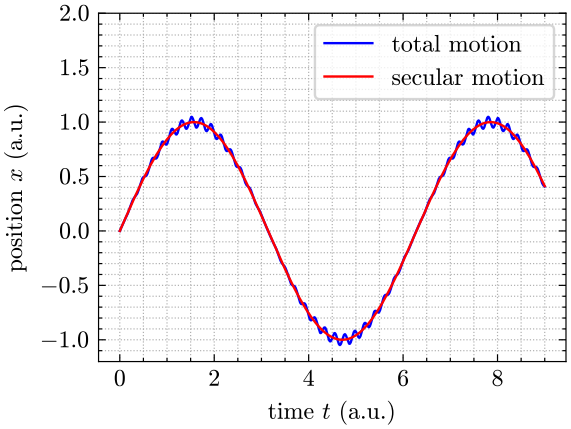


Fig. 2.7: Comparison of total ion motion (secular and micromotion) vs. secular motion alone. The direct comparison is visualized using the solution the secular approximation provides in Eq. 2.3.17 with a q-value of $q = 0.1$ and a frequency ratio between drive frequency Ω and the secular frequency ω_{sec} of $\Omega/\omega_{sec} = 30$. The separation of secular and micromotion is clearly visible.

As shown in Eq. 2.3.16 the solution that the secular approximation provides can be related to the dimensionless Mathieu q-parameter, that is explicitly given by:

$$q = \frac{2eV_{RF}}{m\Omega^2 x_0^2} \ , \tag{2.3.18}$$

relating the secular frequency ω_{sec} to the drive frequency of the RF-potential Ω. If $q \ll 1$ the time scales between driven micromotion and resulting secular motion are well separated and the pseudopotential approximation holds true. Taking a numerical approach to solve the equation of motion in each dimension, one also can use the general Mathieu equation:

$$\frac{d^2x}{d\tau^2} + (a - 2q\cos(2\tau))x = 0 \ , \tag{2.3.19}$$

and relate it by mathematical transformation and direct comparison to the resulting force of the confining potential (respective spatial, negative derivative of Eq. 2.3.7). This direct comparison introduces another parameter, the Mathieu a-parameter. The direct relation to the Mathieu equation yields the following expressions for the a- and q-parameters in all three spatial dimensions:

$$\begin{aligned} a_x &= -\frac{4eU_0}{mz_0^2\Omega^2} = a_y = a_{radial} & \qquad a_z &= \frac{8eU_0}{mz_0^2\Omega^2} = -2a_{radial} \\ q_x &= -\frac{4eV_{RF}}{mr_0^2\Omega^2} = -q_y & \qquad q_z &= 0 \ . \end{aligned} \tag{2.3.20}$$

Similar to the q-parameter, which relates the secular motional frequency of the ions to the effects of the oscillating RF field, the a-parameter relates the ion motion to effects caused by the static field providing axial confinement. Together, these parameters determine the stability region of the linear Paul trap, as shown in Fig. 2.8. The q-parameter governs the stability of the radial confinement: small values yield stable motion with weak micromotion, whereas larger values increase micromotion and heating, ultimately leading to loss of confinement, as shown in Fig. 2.9.

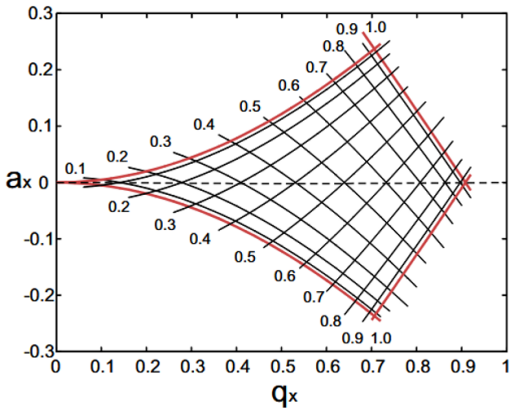


Fig. 2.8: First stability region of a linear Paul trap in the (q_x, a_x) plane, as obtained from the Mathieu equation. The red curves mark the stability boundaries for ion confinement. The black contour lines indicate combinations of trap parameters that lead to equal secular motional frequencies in the radial directions. Stable trapping is achieved only for parameter sets located inside the enclosed region [44]. Illustration adapted from Ref. 45.

.

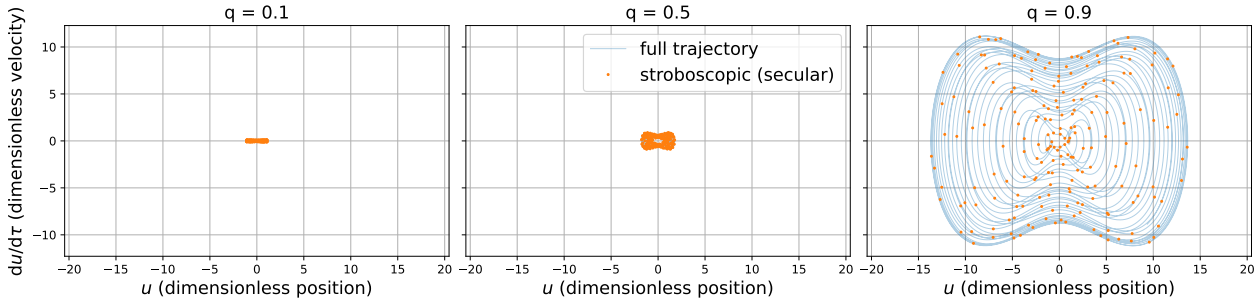


Fig. 2.9: Visualization of trapped ion trajectory with respect to radial dimension using the numerically solved Mathieu equation in a dimensionless phase-space picture. From left to right the Mathieu q-parameter increases from $q = 0.1$ to $q = 0.5$ and finally to $q = 0.9$. The Mathieu a-parameter was kept at $a = 0$, so that there is no contribution from the axial static field so that the radial dynamics are emphasized.

2.3.2 General trapping procedure

The reader will now be familiarized with the general trapping procedure used within the experiment. It shall be noted that the following procedure is not the only method for loading ions into a trap. Other procedures can include an atomic source that is heated in a special oven until emission of an effusive atomic beam through a small aperture occurs. This type of source for ion traps is the most common and very reliable, but can have drawbacks. For example an oven-type source must be heated to a certain temperature to work properly, which takes time. If the oven is kept running to avoid reheating, a continuous stream of particle clouds flows constantly into the trap, increasing background pressure and noise. Furthermore, collisions with already trapped ions cause additional heating. For cryogenic environments the oven-type source and the heat it produces are in constant conflict with the cryostat (the device cooling the system), which may prevent one from reaching the lowest possible temperatures.

The ionization step can also differ between experiments since it need not be performed via photoionization (PI). Another option is the process of electron impact ionization, in which a beam of electrons is sent toward the neutral atom cloud. In this concept an individual electron then collides with an atom, effectively knocking an electron out of the atom shell and therefore ionizing the atom according to the reaction equation:

$$A + e^- \rightarrow A^+ + 2e^- \ . \tag{2.3.21}$$

In reality the same atom can be hit by more than just the one electron intended, leading to double ionization. Furthermore the technique of electron impact ionization is very broadband and non-selective, meaning every species it hits gets ionized and may end up trapped. Additionally the beam of electrons can induce charges on metallic surfaces inside the trap, i.e. the blades, which even can be damaged by this process in the worst case.

Therefore, we use an ablation laser targeted at a sample of barium alongside the isotope-selective method of PI, which together provide our trap with high density plumes of ionized specimen, only when needed.

i) Ablation:

The first step of the trapping sequence is the provision of a neutral atom supply, which ideally consists of the target species only. For that purpose ultrapure, solid samples are commercially available, which can also be enriched with specific isotopes if desired. Usually these samples are sealed with an indium cap to maintain and guarantee purity. Nonetheless a certain amount of an oxide layer on the surface of the solid sample is hardly avoidable. The ablation laser, targeted at such a sample, must remove the indium-oxide layer first, before the trap can be reliably loaded with the desired species. The need for a controllable source of pure specimen is imperative. If the atomic source is in place, we use an ablation laser[2] and send short, high-intensity pulses at it to bring a cloud of neutral atoms across the trapping site. Many parameters play a crucial role in the process of laser ablation loading, such as the spot size, optical power of ablation laser, number of shots, the alignment, as well as the angle of incidence [46].

ii) Photoionization (PI):

Once the ablation pulse has been sent and the trapping region is reliably supplied with the initially neutral target species, the next step of the trapping procedure follows, namely photoionization (PI). For the PI process, the trap zone is illuminated by the laser fields used for the two-photon ionization process, 553 nm and 416 nm, aligned as shown in Fig. 4.3. The trapping pseudopotential is active during the whole time and does not act on neutral particles. If the newly ionized particles are slow enough to not escape pseudopotential well, they are effectively trapped at the moment of ionization. For a more detailed description and additional information the reader is referred to Ref. 47.

2.4 Cooling, readout and SPAM of $^{138}Ba^{+}$ qubits

This section provides the reader with an overview of two different techniques used in the experiment to cool the motional state of $^{138}Ba^{+}$ ions. The fundamentally relevant concepts of state preparation and measurement (SPAM) as well as the readout sequence as method of measurement is explained in detail.

2.4.1 Cooling methods

For cooling $^{138}Ba^{+}$ ions two methods are used: Doppler cooling and resolved sideband cooling (SBC). Fig. 2.10 illustrates the relevant energy levels of $^{138}Ba^{+}$ for both cooling methods.

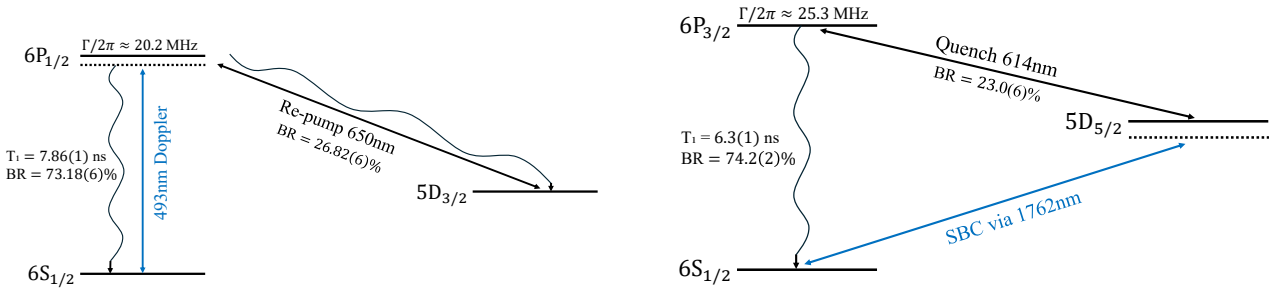


Fig. 2.10: (a) Illustration of $^{138}Ba^{+}$ energy levels used for the Doppler cooling process including relevant branching ratios (BR), lifetime T_1, and corresponding linewidth Γ [48]. The red detuning of the Doppler beam is indicated by the dotted line. (b) Diagram showing the energy levels involved in the process of sideband cooling (SBC), also including relevant BR, lifetime T_1, and corresponding linewidth Γ [49]. The red sideband of the motional mode structure is indicated by the dotted line.

Doppler cooling is based on the resonant absorption of photons by an ion, followed by spontaneous emission. The spontaneous emission is assumed to be isotropic, as random changes of the ion's internal angular momentum

[2] Cobolt FLARE NX at 532 nm

lead to radiation over the full solid angle 4π. The Doppler cooling beam is red-detuned from the atomic resonance and therefore becomes resonant only if the ion moves toward the laser beam, effectively compensating the detuning via the Doppler effect, which gives this cooling method its name. Upon absorption, the ion experiences a momentum kick along the propagation direction of the laser beam. During the subsequent spontaneous emission process, momentum conservation does not yield a net momentum transfer, since the time-averaged momentum associated with spontaneous emission vanishes.

The excitation induced by the Doppler beam does not decay exclusively back to the fluorescing ground state but can also populate the $5D_{3/2}$ manifold. This behavior is probabilistically described by the branching ratio (BR), which quantifies the relative probabilities of all allowed decay channels from a given excited state. In the context of Doppler cooling, the branching ratio directly influences the cooling efficiency. The re-pump beam at 650 nm returns population from the $5D_{3/2}$ manifold into the fluorescence cycle, making the ion available again for Doppler cooling after decay to the ground state. While a red-detuned Doppler beam preferentially couples to ions moving toward the laser and thus cools them, it also weakly couples to ions moving away from the beam, which results in heating. At sufficiently low temperatures, the cooling and heating rates balance each other. The lowest temperature achievable by Doppler cooling, known as the Doppler limit, is reached when the cooling rate equals the heating rate:

$$\underbrace{2\frac{\hbar^2k^2}{m}\frac{\Gamma}{4}S}_{\text{heating rate}} = \underbrace{-\frac{2\hbar k^2}{m}SE_{kin}}_{\text{cooling rate}} \implies T_D = \frac{\hbar\Gamma}{2k_B}\ , \tag{2.4.1}$$

with S corresponding to the saturation parameter (I/I_{sat}), m being the mass of the species, Γ the linewidth of the transition used, and k_B the Boltzmann constant [50]. The choice of transition is therefore relevant regarding the Doppler limit.

The principles behind resolved SBC are derived and explained in Sec. 2.5. For the SBC process, one uses the ladder structure of the Jaynes-Cummings Hamiltonian on the red sideband. Every cooling cycle consists of excitation on the red sideband, which reduces the mean phonon number, $\bar{n}$, about one. Afterwards, a short-lived state is coupled into the process ($6P_{3/2}$ with a lifetime of 6.3 ns), increasing efficiency because one does not need to wait as long until the electronic state spontaneously decays to the ground state manifold and thus is available for the next cooling cycle to further reduce the phonon number [51]. This method is referred to as quenching as it shortens the duration significantly. The SBC method counts among the sub-Doppler cooling methods, since it can reach temperatures below the Doppler limit. SBC also has a limit, which is typically much lower than the Doppler limit. Main contributions to residual heating are due to off-resonant excitation of the blue sideband, which increase the phonon number, and recoil heating through the spontaneous emission and the momentum transfer accompanied by it. Eq. 2.4.2 shows the theoretical limit for SBC, assuming the Lamb Dicke regime (explained in detail in Sec. 2.5) and a transition linewidth Γ much smaller than the axial trap frequency ω_{trap} [52].

$$\langle\bar{n}\rangle_{\text{SBC}} \simeq \left(\frac{\Gamma}{4\,\omega_{\text{trap}}}\right)^2 \tag{2.4.2}$$

2.4.2 State preparation and measurement via readout (SPAM)

The used energetic levels of $^{138}Ba^+$ for the process of SPAM, which includes state preparation and the readout sequence as method of measurement, are illustrated in Fig. 2.11. State preparation is achieved by removing population ('pumping out') from the undesired $6S_{1/2}$ state with $m_j = +\frac{1}{2}$ through coherent driving of the electric–quadrupole transition to the $5D_{5/2}$ state with $m_j = -\frac{3}{2}$ via resonant 1762 nm light. Population in the metastable $5D_{5/2}$ state is subsequently quenched to the short-lived $6P_{3/2}$ manifold. From this excited state, spontaneous decay proceeds via allowed electric–dipole transitions, predominantly back to the $6S_{1/2}$ ground-state manifold, while additional decay channels into the $5D_{3/2}$ and $5D_{5/2}$ states are also present [53].

Population transferred into the D manifolds is recycled by the corresponding re-pumping lasers (614 nm and 650 nm), such that repeated application of the sequence efficiently accumulates population in the intended ground-state Zeeman sublevel $6S_{1/2}$, $m_j = -\frac{1}{2}$. Under the assumption of an equal population of the Zeeman sublevels of the $6P_{3/2}$ state and neglecting the less likely D manifold decay channels, the branching ratio for decay into the desired and undesired ground-state Zeeman substates is equal, yielding a probability of 50 % for each outcome. Therefore, the cycle must be repeated to ensure high ground-state preparation fidelity. With an initial ground-state population a and a probability b of ending in the ground state per cycle, the probability to

correctly prepare the desired ground state is (in this example) given by:

$$\begin{aligned} p_{\text{correct}} &= 1 - (1-a)\cdot(1-b)^N \\ &= 1 - (1-0.5)\cdot(1-0.5)^N \ , \end{aligned} \tag{2.4.3}$$

which indicates that one needs 16 cycles to prepare the ground state with a population fidelity of 99.999 %. This number of cycles corresponds to approximately 100 ns when considering only the lifetime of the short-lived $6P_{3/2}$ state. In the experiment, however, the quench laser prepares predominantly a $6P_{3/2}$ with $m_j = +3/2$ and to a lesser extent the same state with $m_j = +1/2$ due to the specific magnitudes of the so-called Clebsch–Gordan coefficients, which determine the branching ratio of different Zeeman sublevels [54]. So the total BR equals not 50 % but is in favor of preparing the correct state, which implies even fewer cycles are needed in the example. As this simplified example neglects decay channels via the D manifold and ignores finite laser pulse durations as well as rise times of the electronic control components, the value obtained here constitutes a lower bound, with realistic experimental values being orders of magnitude larger.

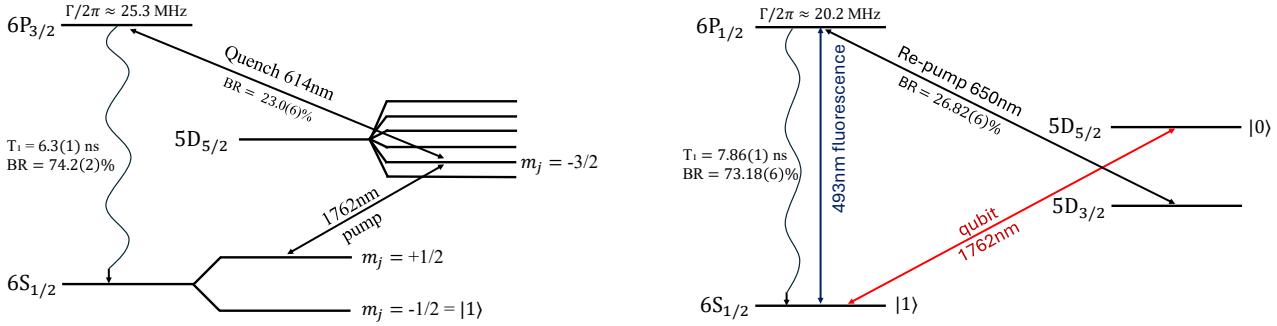


Fig. 2.11: (a) Energy levels of $^{138}Ba^+$ involved in the process of state preparation including relevant branching ratios (BR), lifetime T_1, and corresponding linewidth Γ [49]. (b) Energy levels used for the readout process in $^{138}Ba^+$ including relevant branching ratios (BR), lifetime T_1, and corresponding linewidth Γ [48]. These procedures of state preparation and readout together define the process of SPAM.

State readout is performed via fluorescence detection by selectively driving an electronic transition, namely the $6S_{1/2} \leftrightarrow 6P_{1/2}$ transition, as indicated in Fig. 2.11(b) [43]. The excited electronic state, $|0\rangle$, is referred to as the dark state, since it is decoupled from the fluorescence cycle and therefore does not emit photons unless it spontaneously decays. In contrast, when the electron occupies the ground state, $|1\rangle$, driving the 493 nm fluorescence transition induces resonant excitation cycles (see Sec. 2.5), causing the ion to emit photons. The ground state is therefore referred to as the bright state.

Bayes' theorem provides a consistent framework for updating the probability of a hypothesis by combining prior probabilities with likelihood functions, resulting in posterior probabilities [55]. The photon-count statistics of the bright and dark states are modeled by the corresponding conditional probability mass functions (PMFs) $P_i(n) \coloneqq P(n \mid i)$. The probabilities for misidentifying the bright state as dark and vice versa are given by:

$$\epsilon_{\text{bright}\to\text{dark}}(n_{\text{th}}) = \sum_{n=0}^{n_{\text{th}}} p_{\text{bright}}\, P_{\text{bright}}(n) \qquad \epsilon_{\text{dark}\to\text{bright}}(n_{\text{th}}) = \sum_{n=n_{\text{th}}+1}^{\infty} p_{\text{dark}}\, P_{\text{dark}}(n) \ , \tag{2.4.4}$$

where p_i denotes the prior occupation probability of the respective electronic state. Neglecting spontaneous decay during the detection interval, the photon-count statistics of the bright and dark states are described by Poisson PMFs conditioned on the state:

$$P_i(n) \coloneqq P(n \mid i) = \frac{\mu_i^n}{n!}\, e^{-\mu_i}, \tag{2.4.5}$$

where $n \in \mathbb{N}_0$ denotes the detected photon number and μ_i is the mean photon number of the bright and dark states, respectively [55]. This approach reflects the discrete nature of fluorescence detection and the assumption that the two state-dependent distributions are well separated, thereby allowing each distribution to be evaluated independently.

When spontaneous decay during the detection interval is taken into account, an ion prepared in the dark state may decay into the bright manifold at a time t within the detection window $[0, t_{\text{det}}]$. Conditioned on a

decay event occurring at time t, the expected photon number is modeled as a weighted mean of the dark and bright contributions:

$$\mu(t) = \mu_d \frac{t}{t_{\text{det}}} + \mu_b \left(1 - \frac{t}{t_{\text{det}}}\right) , \tag{2.4.6}$$

with μ_d and μ_b being the mean photon numbers associated with the dark and bright states, respectively. As a consequence, the photon-count distribution of the dark state is modified and can be described by an effective PMF:

$$P^{\text{eff}}_{\text{dark}}(n) = (1 - p_{\text{dec}})\, P_{\text{dark}}(n) + p_{\text{dec}}\, P_{\text{decay}}(n) , \tag{2.4.7}$$

where $p_{\text{dec}} = 1 - e^{-t_{\text{det}}/\tau}$ is the probability for spontaneous decay during the detection interval, τ denotes the lifetime of the dark state, $P_{\text{dark}}(n)$ is the Poisson PMF of a non-decaying dark ion, and $P_{\text{decay}}(n)$ is the photon-count PMF associated with decay events [56]. The latter is given by:

$$P_{\text{decay}}(n) = \frac{1}{p_{\text{dec}}} \int_0^{t_{\text{det}}} \frac{1}{\tau} e^{-t/\tau} \frac{\mu(t)^n}{n!} e^{-\mu(t)}\, dt . \tag{2.4.8}$$

The possible occurrence of spontaneous decay during the readout sequence causes the dark-state photon-count distribution to develop a shoulder toward the bright distribution, effectively reducing the separation between the two PMFs and increasing the overall readout error. An increase of the exposure time to collect more photons is only beneficial to a limited extent, since the probability of spontaneous decay increases simultaneously. Furthermore, the two distributions can no longer be modeled independently but must be treated as a combined mixture, as they become effectively coupled. In both approaches, with and without considering the spontaneous decay, the total readout error is then given by the overlap of the two PMFs modeling bright and dark distributions:

$$\epsilon_{\text{RO}} \coloneqq \epsilon_{\text{bright}\to\text{dark}} + \epsilon_{\text{dark}\to\text{bright}} . \tag{2.4.9}$$

The Bayes-optimal threshold:

$$n^{\text{Bayes}}_{\text{th}} \coloneqq \arg\min_{n\in\mathbb{N}_0} [\epsilon_{\text{RO}}(n)] \tag{2.4.10}$$

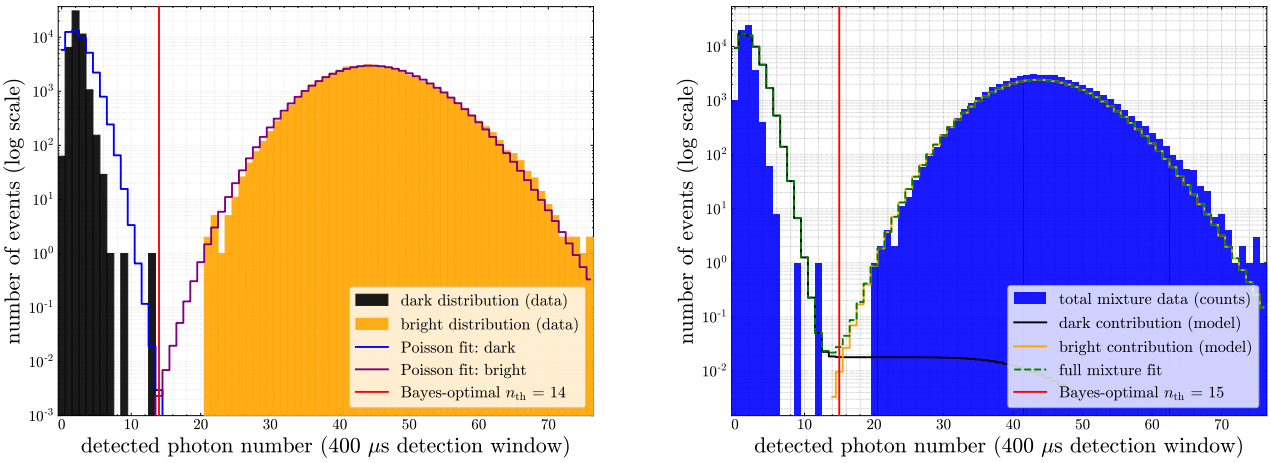
is defined as the photon-count threshold that minimizes the average readout error. This criterion assigns each photon-count outcome to the electronic state with the larger posterior probability, thereby accounting for both the photon-count statistics and the prior state populations. The Bayes-optimal threshold therefore corresponds to the decision boundary at which the weighted PMFs intersect, yielding the minimal achievable readout error [55].

Repeated measurements of approximately equally prepared bright and dark states provide the stochastic data required to construct normalized photon-count histograms, to evaluate the corresponding PMFs, and to quantify the overall readout error. The emitted fluorescence photons are collected by an imaging system based on an electron-multiplying charge-coupled device (EMCCD), resulting in a discrete photon-count distribution. Readout is performed by applying the Bayes-optimal threshold discriminator n_{th} to the detected photon number n: outcomes with $n \leq n_{\text{th}}$ are assigned to the dark state, while outcomes with $n > n_{\text{th}}$ are identified as bright. Fig. 2.12 shows a representative data set recorded with a detection time of 400 µs together with the corresponding analysis.

Strictly speaking, the detector efficiency η_{Det} must also be taken into account when assessing the readout error, as it directly influences the separation between the two photon-count distributions. The overall detector efficiency η_{Det} can be decomposed into three contributions:

$$\begin{aligned} \eta_{\text{Det}} &= (\text{collection efficiency}) \times (\text{optical transmission}) \times (\text{quantum efficiency of the detector}) \\ &= \eta_{\text{coll}}\, \eta_{\text{opt}}\, \eta_{\text{QE}} , \end{aligned} \tag{2.4.11}$$

where the collection efficiency η_{coll} quantifies how efficiently fluorescence photons emitted by the ion are collected, predominantly determined by the NA of the optical imaging system. The optical transmission efficiency η_{opt} describes the fraction of photons transmitted through the optical elements along the detection path, while the detector quantum efficiency η_{QE} denotes the probability that an incident photon is successfully converted into a detectable signal by the sensor array [15].



(a) (b)

Fig. 2.12: Normalized photon-count histograms of bright and dark states together with the intersection of the fitted probability mass functions. (a) Without considering spontaneous decay during the detection interval, a Bayes-optimal threshold of $n_{\mathrm{th}} = 14$ is obtained, corresponding to a minimal readout error of $\epsilon_{\mathrm{RO}} = 3.8 \times 10^{-8}$. (b) When spontaneous decay is taken into account, the Bayes-optimal threshold shifts to $n_{\mathrm{th}} = 15$, resulting in a minimal readout error of $\epsilon_{\mathrm{RO}} = 5.2 \times 10^{-6}$. The plateau observed in the dark-state contribution arises from spontaneous decay during the detection interval and reflects the corresponding decay probability.

2.5 Ion-light interactions with a harmonically confined ion

This section provides an overview of different interaction mechanisms for trapped ions. The interactions presented and partially derived here include the Hamiltonian of a single light field as well as that of two light fields interacting with an ion. In addition, the concept of optical forces is introduced.

2.5.1 Single-light-field interaction Hamiltonian

A single ion and its axial harmonic confinement are considered in the following. The general form of the total Hamiltonian $\hat{\mathcal{H}}_{\mathrm{total}}$ of a two-level system (TLS) in one spatial dimension reads:

$$\begin{aligned}\hat{\mathcal{H}}_{\mathrm{total}}(x) &= \underbrace{\frac{\hat{p}_x^2}{2m} + \hat{V}(x) + \frac{\hbar\omega_0}{2}\hat{\sigma}_z}_{=\hat{\mathcal{H}}_0} \underbrace{- \hat{\boldsymbol{\mu}} \cdot \hat{\mathbf{E}}}_{=\hat{\mathcal{H}}_1} \\ &= \hat{\mathcal{H}}_0 + \hat{\mathcal{H}}_1 \ , \end{aligned} \tag{2.5.1}$$

with $\hat{p}_x$ denoting the momentum operator along the considered spatial dimension, m the ion mass, $\hat{V}(x)$ the trapping potential, $\hbar$ the reduced Planck constant, and $\omega_0 = 2\pi\nu_0$ the angular frequency of the internal transition encoding the qubit. Furthermore, $\hat{\sigma}_z$ denotes the Pauli operator, while $\hat{\boldsymbol{\mu}}$ and $\hat{\mathbf{E}}$ represent the electric dipole operator and the electric field operator, respectively [20].

The Hamiltonian $\hat{\mathcal{H}}_0$ describes the internal and motional degrees of freedom of the ion. The first two terms correspond to the kinetic and potential energy associated with the harmonic motion in the trapping potential, while the third term describes the internal electronic two-level structure used to encode the qubit. Fig. 2.13 illustrates the internal and motional subsystems described by $\hat{\mathcal{H}}_0$. Coupling between these degrees of freedom arises only through the interaction of the trapped ion with the laser light field, which is described by the Hamiltonian $\hat{\mathcal{H}}_1$.

The total Hamiltonian $\hat{\mathcal{H}}_{\mathrm{total}}$ is based on the dipole approximation [57]. The potential energy in the axial trap dimension is of harmonic form:

$$\hat{V}(\hat{x}_j) = \frac{1}{2} m\, \omega_j^2\, \hat{x}_j^2, \tag{2.5.2}$$

where ω_j denotes the oscillation frequency of the axial normal mode labeled j, $\hat{x}_j$ is the corresponding normal-mode coordinate, and m represents the particle mass. Fig. 2.6 in Sec. 2.3 illustrates the energetically lowest axial normal modes for a 3-ion chain. With the quantum mechanical ladder operators, introduced by Paul

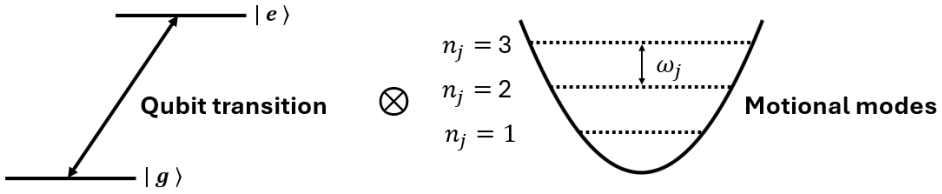


Fig. 2.13: The internal electronic two-level system (TLS) and the quantized harmonic motional mode with frequency ω_j described by the Hamiltonian $\hat{\mathcal{H}}_0$ are illustrated. Coupling between these degrees of freedom occurs only via the interaction Hamiltonian $\hat{\mathcal{H}}_1$.

Dirac:

$$\hat{a}_j = \sqrt{\frac{m\,\omega_j}{2\hbar}}\left(\hat{x}_j + \frac{i}{m\,\omega_j}\,\hat{p}_j\right) \qquad \hat{a}_j^\dagger = \sqrt{\frac{m\,\omega_j}{2\hbar}}\left(\hat{x}_j - \frac{i}{m\,\omega_j}\,\hat{p}_j\right)\ , \tag{2.5.3}$$

the Hamiltonian $\hat{\mathcal{H}}_0$ can be re-written as:

$$\hat{\mathcal{H}}_0 = \hbar\,\omega_j\left(\hat{a}_j^\dagger\,\hat{a}_j + \frac{1}{2}\right) + \frac{\hbar\,\omega_0}{2}\hat{\sigma}_z = \hbar\,\omega_j\left(\hat{n}_j + \frac{1}{2}\right) + \frac{\hbar\,\omega_0}{2}\hat{\sigma}_z\ , \tag{2.5.4}$$

with $\hat{n}_j = \hat{a}_j^\dagger\,\hat{a}_j$ being the quantum mechanical number operator counting the phonon number, that quantifies the energy of the ion oscillation of mode frequency ω_j [6, 58]. While the harmonic-oscillator description is valid for all motional excitation numbers in a harmonic trap, the treatment of the motional and internal degrees of freedom as approximately decoupled is justified only in the Lamb–Dicke regime. In this regime, the spatial extent of the ion's wave packet is small compared to the wavelength of the applied radiation, which is typically realized close to the motional ground state [43].

For the interaction Hamiltonian $\hat{\mathcal{H}}_1$, the electric dipole moment is described by the dipole operator $\hat{\boldsymbol{\mu}}$, which can be expanded in the basis of internal electronic states as:

$$\hat{\boldsymbol{\mu}} = \sum_{m,n}\mu_{m,n}\,|m\rangle\,\langle n| \overset{\text{TLS}}{=} \mu_{0,1}\,|0\rangle\,\langle 1| + \mu_{1,0}\,|1\rangle\,\langle 0|\ , \tag{2.5.5}$$

where, in the second step, the restriction to a two-level system (TLS) is applied. The diagonal matrix elements vanish because the electric dipole operator is odd under spatial inversion, such that $\mu_{i,i} = 0$ for states of definite parity [57]. A specific dipole matrix element characterizing the coupling strength between two internal states is given by $\mu_{n,m} = \langle n|\,\hat{\boldsymbol{\mu}}\,|m\rangle$. For a TLS, the dipole operator can therefore be expressed in terms of the atomic raising and lowering operators:

$$\hat{\sigma}_+ = |e\rangle\,\langle g| = |0\rangle\,\langle 1| = \begin{pmatrix}0 & 1\\ 0 & 0\end{pmatrix} \qquad \hat{\sigma}_- = |g\rangle\,\langle e| = |1\rangle\,\langle 0| = \begin{pmatrix}0 & 0\\ 1 & 0\end{pmatrix}\ , \tag{2.5.6}$$

in the ordered basis $\{|e\rangle, |g\rangle\}$. The laser light field is treated in the semiclassical approximation as:

$$\mathbf{E}(\hat{x}_j, t) = E_0\,\boldsymbol{\epsilon}_L\,e^{i(k_x\,\hat{x}_j - \omega_L\,t + \phi_L)} + E_0^*\,\boldsymbol{\epsilon}_L^*\,e^{-i(k_x\,\hat{x}_j - \omega_L\,t + \phi_L)}\ , \tag{2.5.7}$$

where E_0 denotes the complex field amplitude, $\boldsymbol{\epsilon}_L$ is the (generally complex) polarization unit vector, k_x is the projection of the laser wave vector onto the $\hat{x}$ direction, the spatial phase of the field is evaluated at the eigenmode-dependent ion position operator $\hat{x}_j$, ω_L is the angular frequency of the laser field, and ϕ_L denotes its optical phase. The second term corresponds to the complex conjugate, ensuring that the electric field is real. The term for the dipole operator in combination with the classical electric field yields an explicit expression for the interaction Hamiltonian $\hat{\mathcal{H}}_1$ in the electric-dipole approximation:

$$\hat{\mathcal{H}}_1 = -\hat{\boldsymbol{\mu}}\,\mathbf{E}(\hat{x}_j, t) = -(\mu_{0,1}\,\hat{\sigma}_- + \mu_{1,0}\,\hat{\sigma}_+)\cdot\left(E_0\,\boldsymbol{\epsilon}_L\,e^{i(k_x\,\hat{x}_j - \omega_L\,t + \phi_L)} + E_0^*\,\boldsymbol{\epsilon}_L^*\,e^{-i(k_x\,\hat{x}_j - \omega_L\,t + \phi_L)}\right)\ . \tag{2.5.8}$$

Switching to the interaction picture with respect to the uncoupled atomic and motional Hamiltonian $\hat{\mathcal{H}}_0$:

$$\hat{\mathcal{H}}_{int} = \hat{U}^\dagger\,\hat{\mathcal{H}}_1\,\hat{U} \qquad \text{with } \hat{U} = e^{-i\,\hat{\mathcal{H}}_0\,t/\hbar}\ , \tag{2.5.9}$$

the operators evolve under $\hat{\mathcal{H}}_0$, while the state vectors evolve under the interaction Hamiltonian $\hat{\mathcal{H}}_{int}$. The resulting interaction picture Hamiltonian under the semi-classical electric-dipole interaction reads:

$$\begin{aligned}\hat{\mathcal{H}}_{int} &= -(\mu_{0,1}\,\hat{\sigma}_-\,e^{-i\omega_0 t} + \mu_{1,0}\,\hat{\sigma}_+\,e^{+i\omega_0 t})\cdot\left(E_0\,\boldsymbol{\epsilon}_L\,e^{i(k_x\,\hat{x}_j-\omega_L\,t+\phi_L)} + E_0^*\,\boldsymbol{\epsilon}_L^*\,e^{-i(k_x\,\hat{x}_j-\omega_L\,t+\phi_L)}\right)\\ &= -\mu_{0,1}\,\hat{\sigma}_-\left(E_0\,\boldsymbol{\epsilon}_L\,e^{i(k_x\,\hat{x}_j-(\omega_L+\omega_0)t+\phi_L)} + E_0^*\,\boldsymbol{\epsilon}_L^*\,e^{-i(k_x\,\hat{x}_j-(\omega_L-\omega_0)t+\phi_L)}\right) + \text{h.c.}\end{aligned} \tag{2.5.10}$$

where "h.c." denotes the Hermitian conjugate of the preceding term. Owing to the Hermiticity of the dipole operator, the off-diagonal matrix elements satisfy $\mu_{1,0} = \mu_{0,1}^*$, such that their magnitudes are equal and may be written as $\mu \coloneqq |\mu_{0,1}| = |\mu_{1,0}|$. The Rabi frequency is defined as:

$$\Omega \coloneqq \left|\frac{-2\mu\boldsymbol{\epsilon}_L E_0}{\hbar}\right| , \tag{2.5.11}$$

and, together with the rotating-wave approximation (RWA), which neglects terms oscillating at $\omega_L + \omega_0$, it can be used to reduce the interaction Hamiltonian to:

$$\begin{aligned}\hat{\mathcal{H}}_{int} &\overset{\text{RWA}}{=} -\mu\,\hat{\sigma}_-\,E_0^*\,\boldsymbol{\epsilon}_L^*\,e^{-i(k_x\,\hat{x}_j-(\omega_L-\omega_0)t+\phi_L)} - \mu\,\hat{\sigma}_+ E_0\,\boldsymbol{\epsilon}_L\,e^{i(k_x\,\hat{x}_j-(\omega_L-\omega_0)t+\phi_L)}\\ &= \frac{\hbar\Omega}{2}\left(\hat{\sigma}_+\,e^{i(k_x\,\hat{x}_j-(\omega_L-\omega_0)t+\phi_L)} + \hat{\sigma}_-\,e^{-i(k_x\,\hat{x}_j-(\omega_L-\omega_0)t+\phi_L)}\right) .\end{aligned} \tag{2.5.12}$$

The RWA is valid in the regime $\Omega \ll \omega_L, \omega_0$, in which the states in the rotating frame evolve slowly with respect to the optical timescale [20, 58]. Furthermore, in the interaction picture the ladder operators acquire an explicit time dependence:

$$\hat{a}_j(t) = \hat{a}_j\cdot e^{-i\omega_j t} \qquad\qquad \hat{a}_j^\dagger(t) = \hat{a}_j^\dagger\cdot e^{+i\omega_j t} . \tag{2.5.13}$$

With the detuning defined as $\Delta \coloneqq \omega_L - \omega_0$, and expressing the position operator in terms of ladder operators:

$$\hat{x}_j = \sqrt{\frac{\hbar}{2m\omega_j}}\left(\hat{a}_j + \hat{a}_j^\dagger\right) \equiv x_{0,j}\left(\hat{a}_j + \hat{a}_j^\dagger\right) \qquad \text{with } x_{0,j} \coloneqq \sqrt{\frac{\hbar}{2m\omega_j}} , \tag{2.5.14}$$

Eq. 2.5.12 can be re-written as:

$$\begin{aligned}\hat{\mathcal{H}}'_{int} &= \frac{\hbar\Omega}{2}\left(\hat{\sigma}_+\,e^{-i(\Delta t-\phi_L)}\,e^{i\eta_j\,(\hat{a}_j(t)+\hat{a}_j^\dagger(t))} + \hat{\sigma}_-\,e^{+i(\Delta t-\phi_L)}\,e^{-i\eta_j\,(\hat{a}_j(t)+\hat{a}_j^\dagger(t))}\right)\\ &= \frac{\hbar\Omega}{2}\left(\hat{\sigma}_+\,e^{-i(\Delta t-\phi_L)}\,e^{i\eta_j\,(\hat{a}_j\cdot e^{-i\omega_j t}+\hat{a}_j^\dagger\cdot e^{+i\omega_j t})} + \hat{\sigma}_-\,e^{+i(\Delta t-\phi_L)}\,e^{-i\eta_j\,(\hat{a}_j\cdot e^{-i\omega_j t}+\hat{a}_j^\dagger\cdot e^{+i\omega_j t})}\right) ,\end{aligned} \tag{2.5.15}$$

where the Lamb–Dicke parameter η_j is also introduced, which itself is defined, in the most general case, as:

$$\eta_j = \left|\mathbf{k}\cdot\hat{\mathbf{e}}_j\right| x_{0,j} = k\,|\cos(\theta_j)|\,x_{0,j} = \frac{2\pi}{\lambda}\,|\cos\theta_j|\sqrt{\frac{\hbar}{2m\omega_j}} , \tag{2.5.16}$$

with k the magnitude of the laser wave vector, θ_j the angle between the laser propagation direction and motional mode j, $\hat{\mathbf{e}}_j$ the corresponding mode unit vector, and $x_{0,j}$ the ground-state extent of the harmonic oscillator. The Lamb–Dicke parameter η_j compares the wavelength of the applied laser field, λ, to the spatial extent of the ion's motional wave packet, which for the ground state of motional mode j is given by $x_{0,j}$. In squared form, this parameter may equivalently be interpreted as a comparison between the photon recoil energy and the energy spacing between the motional ground and first excited harmonic-oscillator states:

$$\eta_j^2 = \frac{E_{\text{rec}}}{\hbar\omega_j} . \tag{2.5.17}$$

In trapped-ion experiments, one typically operates in the Lamb–Dicke regime, determined by the Lamb–Dicke criterion:

$$\eta_j\sqrt{2\bar{n}_j + 1} \ll 1 , \tag{2.5.18}$$

which ensures that the spatial extent of the ion's motional wave packet is small compared to the wavelength of the applied laser field. In this regime, the position-dependent laser phase may be expanded perturbatively, and the coupling between internal and motional degrees of freedom becomes weak to lowest order. As a result,

the internal and motional dynamics are approximately separable, with motional sideband transitions strongly suppressed. The Lamb–Dicke regime can be reached either by sufficiently tight confinement (small η_j) or by cooling the ion close to the motional ground state (small $\bar{n}_j$), such that Eq. 2.5.18 is satisfied. Under these conditions, the exponential term involving the Lamb–Dicke parameter η_j can be Taylor expanded as:

$$e^{i\eta_j(\hat{a}_j e^{-i\omega_j t}+\hat{a}_j^\dagger e^{+i\omega_j t})} \approx 1 + i\eta_j(\hat{a}_j e^{-i\omega_j t} + \hat{a}_j^\dagger e^{+i\omega_j t}) + \mathcal{O}(\eta_j^2) \ . \tag{2.5.19}$$

Physically, the Lamb–Dicke regime corresponds to the situation where the momentum transferred by absorption or emission of a photon is insufficient to significantly perturb the ion's motional state. While ground-state cooling represents the most favorable case, the Lamb–Dicke criterion can also be fulfilled for finite phonon occupation provided that the confinement is sufficiently tight. In practice, sub-Doppler cooling techniques are often employed to ensure the validity of the perturbative expansion. Within the Lamb–Dicke regime, the zeroth-order term of the Taylor expansion gives rise to the Hamiltonian describing the carrier transition, which occurs on resonance at zero detuning, $\Delta = 0$:

$$\hat{\mathcal{H}}_{\text{car}} = \frac{\hbar\Omega}{2}(\hat{\sigma}_+ e^{-i\phi_L} + \hat{\sigma}_- e^{+i\phi_L}) = \frac{\hbar\Omega}{2}(\hat{\sigma}_x \cos(\phi_L) + \hat{\sigma}_y \sin(\phi_L)) \ . \tag{2.5.20}$$

If the detuning is chosen to be blue-detuned by the angular motional mode frequency, $\Delta = +\omega_j$, blue sideband transitions can be driven, whereas red sideband transitions occur for a red detuning, $\Delta = -\omega_j$. The first-order term of the Taylor expansion in the Lamb–Dicke parameter gives rise to the interaction Hamiltonians describing the blue and red sidebands, respectively, which read:

$$\hat{\mathcal{H}}_{\text{blue}} = \frac{i\hbar\eta\Omega}{2}(\hat{a}_j^\dagger \hat{\sigma}_+ e^{+i\phi_L} - \hat{a}_j \hat{\sigma}_- e^{-i\phi_L}) \qquad \hat{\mathcal{H}}_{\text{red}} = \frac{i\hbar\eta\Omega}{2}(\hat{a}_j \hat{\sigma}_+ e^{+i\phi_L} - \hat{a}_j^\dagger \hat{\sigma}_- e^{-i\phi_L}) \ . \tag{2.5.21}$$

Application of the blue sideband Hamiltonian leads to excitation with an increase in phonon number, and de-excitation with a decrease in phonon number. For the red sideband Hamiltonian it is vice versa: excitation of electronic state with decrease in phonon number, and de-excitation with enhancing the phonon number. The possible processes of blue and red sideband can be visualized in a ladder form, as seen in Fig. 2.14, and forms the basis for the Jaynes–Cummings model [57].

$$\begin{aligned}
\hat{\mathcal{H}}_{\text{red}} |g,n\rangle &= \frac{i\hbar\eta_j\Omega}{2}\sqrt{n}\,|e,n-1\rangle & \hat{\mathcal{H}}_{\text{red}} |e,n\rangle &= \frac{i\hbar\eta_j\Omega}{2}\sqrt{n+1}\,|g,n+1\rangle \\
\hat{\mathcal{H}}_{\text{blue}} |g,n\rangle &= \frac{i\hbar\eta_j\Omega}{2}\sqrt{n+1}\,|e,n+1\rangle & \hat{\mathcal{H}}_{\text{blue}} |e,n\rangle &= \frac{i\hbar\eta_j\Omega}{2}\sqrt{n}\,|g,n-1\rangle
\end{aligned} \tag{2.5.22}$$

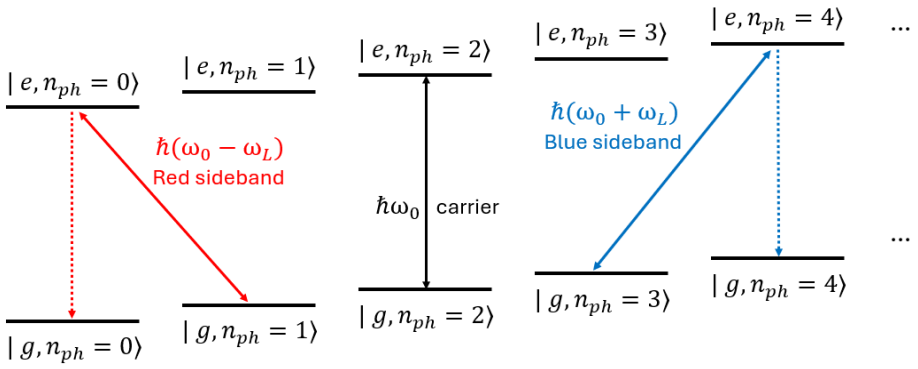


Fig. 2.14: Jaynes–Cummings energy-level ladder, showing the coupled ion–motion states $|g, n_{ph}\rangle$ and $|e, n_{ph}\rangle$. The carrier transition with a zero change in phonon number ($\Delta n_{ph} = 0$) is driven at the angular resonance frequency ω_0 and thus with zero detuning ($\Delta = 0$), while the first red and blue sidebands ($\Delta n_{ph} = \pm 1$) are driven at a detuning $\Delta = \omega_0 \mp \omega_j$, i.e., detuned by the angular motional mode frequency ω_j.

The interaction mechanism described by the Jaynes–Cummings Hamiltonian forms the basis of resolved red sideband cooling (SBC). For the carrier transition, the time-dependent Schrödinger equation associated with the Hamiltonian in Eq. 2.5.20 leads to the optical Bloch equations (OBEs). The solution of the OBEs for a single monochromatic light field interacting with a free two-level ion at arbitrary detuning yields the time-dependent probabilities of finding the system in the respective internal states:

$$p_e(t) = \frac{\Omega^2}{\Omega_{\text{eff}}^2} \sin^2\left(\frac{\Omega_{\text{eff}}\, t}{2}\right), \qquad p_g(t) = 1 - p_e(t) = 1 - \frac{\Omega^2}{\Omega_{\text{eff}}^2} \sin^2\left(\frac{\Omega_{\text{eff}}\, t}{2}\right) \ , \tag{2.5.23}$$

with the generalized Rabi frequency:

$$\Omega_{\text{eff}} \coloneqq \sqrt{(\omega_L - \omega_0)^2 + \frac{|V_{eg}|^2}{\hbar^2}} = \sqrt{\Delta^2 + \Omega^2} \tag{2.5.24}$$
$$\text{with } V_{eg} = \langle e|\hat{\mathcal{H}}_{\text{int}}|g\rangle = -\mu\,\boldsymbol{\epsilon}_L E_0, \qquad |V_{eg}| = \frac{\hbar\Omega}{2}\ .$$

The quantity V_{eg} denotes the off-diagonal matrix element of the electric-dipole interaction Hamiltonian between the internal states $|g\rangle$ and $|e\rangle$, and therefore quantifies the coupling strength of the driven transition. A step-by-step derivation using an explicit matrix formalism can be found in Ref. [59]. In the Lamb–Dicke regime, the internal dynamics can be treated independently of the motional degree of freedom to lowest order, such that the resulting state populations coincide with those of a freely driven TLS. On resonance, $\omega_L = \omega_0$ (i.e., $\Delta = 0$), the generalized Rabi frequency reduces to the on-resonance Rabi frequency, $\Omega_{\text{eff}} = \Omega$, as defined in Eq. 2.5.11. For $\omega_L \neq \omega_0$, off-resonant Rabi oscillations are obtained, whose excited-state amplitude is suppressed for large detunings, $|\Delta| \gg \Omega$, by a factor of $1/\Delta^2$. Fig. 2.15 visualizes the resulting population transfer using the analytical expression in Eq. 2.5.23 for an initial ground state and different ratios of detuning to Rabi frequency (resonant and off-resonant cases).

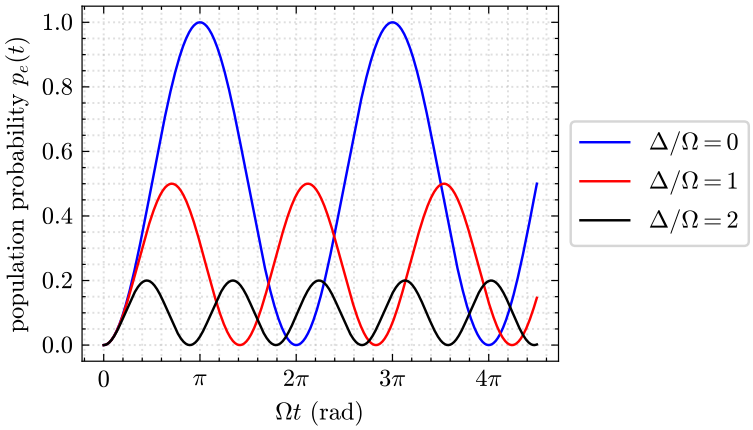


Fig. 2.15: Excited-state population as a function of time for different ratios of detuning over Rabi frequency. The system is initially prepared in the ground state, and the resulting Rabi oscillations illustrate how increasing detuning reduces contrast and modifies the oscillation frequency.

Off-resonant light fields modify the energies of the internal states via virtual excitation processes. This effect is known as the AC-Stark shift (or light shift) and constitutes a coherent shift of the atomic transition frequency induced by the interaction between the dipole moment and the oscillating electric field [58]. In the rotating frame (and within the RWA), the driven TLS is described by:

$$\hat{\mathcal{H}}_{\text{int}}^{\text{AC}} = \frac{\hbar}{2}\left(\Delta\,\hat{\sigma}_z + \Omega\,\hat{\sigma}_x\right) = \frac{\hbar}{2}\begin{pmatrix}\Delta & \Omega\\ \Omega & -\Delta\end{pmatrix}\ . \tag{2.5.25}$$

The solution of corresponding eigenvalue equation:

$$\hat{\mathcal{H}}_{\text{int}}^{\text{AC}}\,|v\rangle = \delta\,|v\rangle\ , \tag{2.5.26}$$

yields the dressed-state energies [20]. The resulting energy shifts relative to the uncoupled case ($\Omega = 0$) are given by:

$$\begin{aligned}\delta_\pm &= \pm\frac{\hbar}{2}\sqrt{\Delta^2 + \Omega^2} \mp \frac{\hbar\Delta}{2}\\ &\approx \pm\frac{\hbar\Omega^2}{4\Delta}, \qquad (|\Delta| \gg \Omega)\ .\end{aligned} \tag{2.5.27}$$

In the far-detuned regime, $|\Delta| \gg \Omega$, the transverse coupling term proportional to $\hat{\sigma}_x$ can be adiabatically eliminated, resulting in an effective AC-Stark Hamiltonian in the interaction picture:

$$\hat{\mathcal{H}}_{\text{eff}}^{\text{AC}} = \frac{\hbar\delta_{\text{AC}}}{2}\,\hat{\sigma}_z \qquad \text{, with } \delta_{\text{AC}} = -\frac{\Omega^2}{2\Delta} \tag{2.5.28}$$

being the transition shift, implying that in the far-detuned regime no Rabi oscillations are driven, and the interaction leads solely to a modification of the energetic level spacing via the AC-Stark shift. The corresponding unitary operator of the AC-Stark shift is given by:

$$\hat{U}_{\mathrm{AC}}(t) = e^{-it\hat{\mathcal{H}}^{\mathrm{AC}}_{eff}/\hbar} = e^{-i\delta_{\mathrm{AC}}\hat{\sigma}_z t/2} = \begin{pmatrix} e^{-i\delta_{\mathrm{AC}}t/2} & 0 \\ 0 & e^{+i\delta_{\mathrm{AC}}t/2} \end{pmatrix} . \tag{2.5.29}$$

The sign of the energy shift depends on the sign of the detuning Δ: for blue detuning ($\Delta > 0$) the ground-state energy is shifted upwards while the excited-state energy is shifted downwards, effectively reducing the transition frequency, whereas for red detuning ($\Delta < 0$) the opposite behavior is observed, as illustrated in Fig. 2.16.

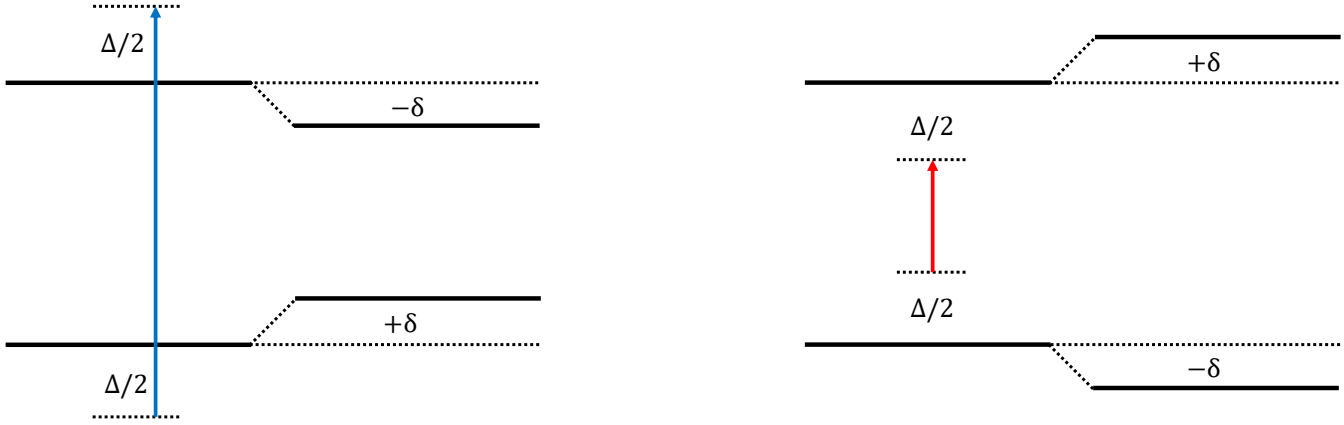


Fig. 2.16: AC-Stark shift of a two-level ion induced by an off-resonant laser field. Shown on the left is the case of blue detuning ($\Delta > 0$), for which the energetic lower state is shifted upward while the excited state is shifted downward, resulting in a reduced transition energy. For red detuning ($\Delta < 0$), shown on the right, the shifts occur in the opposite direction, increasing the energy splitting. The dressed eigenstates (solid lines), relative to the uncoupled states (dashed lines), exhibit level shifts of $\pm\delta$ depending on the sign of the detuning.

2.5.2 Raman interaction Hamiltonian

The starting point and general approach remain the same as in the single-light-field case. However, the interaction Hamiltonian $\hat{\mathcal{H}}_1$ in Eq. 2.5.1 now involves two light fields, $\hat{\mathcal{H}}_1 = -\hat{\boldsymbol{\mu}} \cdot (\mathbf{E}_1 + \mathbf{E}_2)$. These fields couple the electronic ground and excited states of the ion via a virtual intermediate state, thereby defining a stimulated Raman transition. Transformations analogous to those leading to Eq. 2.5.10 (a detailed derivation can be found in Ref. 58), yield the effective interaction-picture Hamiltonian of a Raman scheme:

$$\hat{\mathcal{H}}_{\mathrm{eff}} = \frac{\hbar}{2}\left(-\delta_R\,\hat{\sigma}_z + \Omega_{\mathrm{R}}\,\hat{\sigma}_x\right) = \frac{\hbar}{2}\begin{pmatrix} -\delta_{\mathrm{R}} & \Omega_{\mathrm{R}} \\ \Omega_{\mathrm{R}} & \delta_{\mathrm{R}} \end{pmatrix} , \tag{2.5.30}$$

with δ_R being the so-called Raman two-photon detuning, defined by the angular frequencies ω_{L_1} and ω_{L_2} of the respective light field:

$$\delta_R = (\omega_{L_1} - \omega_{L_2}) - \omega_0 . \tag{2.5.31}$$

The definition of the Rabi frequency is accordingly modified for the Raman case and becomes:

$$\Omega_{\mathrm{R}} = \frac{\Omega_1 \Omega_2^*}{2\Delta} , \tag{2.5.32}$$

where Ω_1 and Ω_2 denote the resonant single-photon Rabi frequencies of the two light fields, and $\Delta := \Delta_1 = \omega_{L_1} - \omega_0 \approx \omega_{L_2} - \omega_0 = \Delta_2$ is the common one-photon detuning. The generalized Raman-Rabi frequency is then given by:

$$\Omega_{\mathrm{eff,R}} = \sqrt{\delta_R^2 + \Omega_{\mathrm{R}}^2} . \tag{2.5.33}$$

In general, the time-dependent state populations for Raman-driven transitions are given by:

$$p_e(t) = \frac{\Omega_{\mathrm{R}}^2}{\Omega_{\mathrm{eff,R}}^2}\sin^2\left(\frac{\Omega_{\mathrm{eff,R}}\,t}{2}\right), \qquad p_g(t) = 1 - p_e(t) = 1 - \frac{\Omega_{\mathrm{R}}^2}{\Omega_{\mathrm{eff,R}}^2}\sin^2\left(\frac{\Omega_{\mathrm{eff,R}}\,t}{2}\right) . \tag{2.5.34}$$

Furthermore, the Lamb–Dicke parameter relevant for Raman schemes is modified to:

$$\eta_j = |\Delta\mathbf{k} \cdot \mathbf{e}_j| \; x_{0,j} \; , \tag{2.5.35}$$

reflecting its dependence on the difference of the wave vectors of the two laser fields, $\Delta\mathbf{k}$. This dependence can be exploited experimentally: using counter-propagating Raman beams maximizes the difference and thus enhances the coupling to motional sidebands, while co-propagating beam geometries minimize η_j and largely suppress motional coupling. Carrier transitions ($\delta_R = 0$) can be driven in either configuration, whereas efficient excitation of motional sidebands ($\delta_R = \pm\omega_j$) requires a sufficiently large wave-vector difference, as provided by counter-propagating Raman beams. In both cases, coherent Raman-driven Rabi oscillations can be realized even though both light fields are individually far detuned from the optical transition.

2.5.3 Optical forces

Light fields also exert mechanical forces on a trapped ion. Two principal types of light-induced forces can be distinguished: the optical dipole force, also referred to as the optical gradient force, and the scattering (radiation pressure) force. Both forces can be derived rigorously by assuming a time-dependent induced dipole moment $\boldsymbol{\mu}(t)$ and analyzing the resulting equations of motion. A detailed derivation of both forces can be found in Ref. [50].

The complex polarizability α relates the induced dipole moment to the electric field amplitude according to:

$$\boldsymbol{\mu}(t) = \alpha \, \mathbf{E}(t) \; . \tag{2.5.36}$$

This approach leads to a dipole potential of the form:

$$U_{\text{dip}} = -\frac{1}{2} \langle \boldsymbol{\mu}(t) \cdot \mathbf{E}(t) \rangle = \frac{1}{2\epsilon_0 c} \, \text{Re}\{\alpha\} \, I \; , \tag{2.5.37}$$

where ϵ_0 denotes the vacuum permittivity, c the speed of light, and I the light-field intensity. The resulting force is given by the negative gradient of the dipole potential and defines the optical dipole force:

$$\begin{aligned} \mathbf{F}_{\text{dip}}(\mathbf{r}) &= -\nabla U_{\text{dip}} = \frac{1}{2\epsilon_0 c} \, \text{Re}\{\alpha\} \, \nabla I(\mathbf{r}) \\ &= -\frac{3\pi c^2}{2\omega_0^3} \frac{\Gamma\Delta}{\Delta^2 + \Gamma^2/4} \, \nabla I(\mathbf{r}) \; , \end{aligned} \tag{2.5.38}$$

where ω_0 is the angular resonance frequency of the atomic transition, Γ its natural linewidth, Δ the laser detuning from resonance, and $I(\mathbf{r})$ the position-dependent intensity. The optical dipole force acts along the direction of the intensity gradient.

The scattering force, on the other hand, arises from momentum transfer associated with photon absorption and spontaneous emission and acts along the gradient of the optical phase $\phi(\mathbf{r})$ of the light field:

$$\mathbf{F}_{\text{SC}}(\mathbf{r}) = \frac{1}{\epsilon_0 c} \, \text{Im}\{\alpha\} \, I \, \nabla\phi(\mathbf{r}) = \frac{3\pi c^2}{2\omega_0^3} \frac{\Gamma}{\Delta^2 + \Gamma^2/4} \, I \, \nabla\phi(\mathbf{r}) \; . \tag{2.5.39}$$

2.6 Physical realization of gate operations

This section summarizes how the ion–light interactions introduced in the preceding sections can be exploited to realize the gate operations presented in Sec. 2.1. Both single-qubit and entangling two-qubit gate operations are discussed for the trapped-ion quantum computing platform. As a final topic, the recently developed transverse approach for implementing an entangling two-qubit geometric phase operation is introduced.

2.6.1 Single-qubit gate operations

Gate operations on single ions can be physically realized using one or more of the methods listed below, as well as combinations thereof.

i) Rabi oscillations:

After preparing the ion in either the ground state or the excited state, the application of a resonant or near-resonant laser field leads to coherent Rabi oscillations, as introduced in Sec. 2.5. Rabi oscillations enable coherent population transfer between the ground and excited states, either completely or partially. A complete population transfer from one state to the other is referred to as a π pulse or a π Rabi flop, while a transfer corresponding to half of this population change is known as a $\pi/2$ pulse. On resonance, these transfers correspond to interaction times of $t = \pi/\Omega$ for a π pulse and $t = \pi/(2\Omega)$ for a $\pi/2$ pulse, respectively.

Resonant and off-resonant Rabi oscillations can be driven using electromagnetic radiation over a wide frequency range, including visible light (10^{14}–10^{15} Hz), microwaves (300 MHz–300 GHz), and radio-frequency radiation (3 Hz–300 MHz), depending on the specific energy splitting and the type of TLS. For example, a Zeeman qubit is directly driven via magnetic-dipole transitions, while optical transitions are directly driven by visible light via electric-dipole coupling. While the underlying physical mechanism is identical in all cases, these regimes are commonly distinguished by terminology, which directly reflects the radiation frequency and the corresponding energy scale involved.

ii) Stimulated Raman transitions:

If the qubit is encoded in a transition that cannot be directly addressed within the spectrum of visible light, but optical manipulation is nevertheless desired, off-resonant stimulated Raman transitions provide a viable alternative [60]. A description of the Raman transition scheme is given in Sec. 2.5. The resulting population dynamics are closely analogous to those of Rabi oscillations driven by a single interacting light field, albeit with modified definitions of the effective detuning and Rabi frequency.

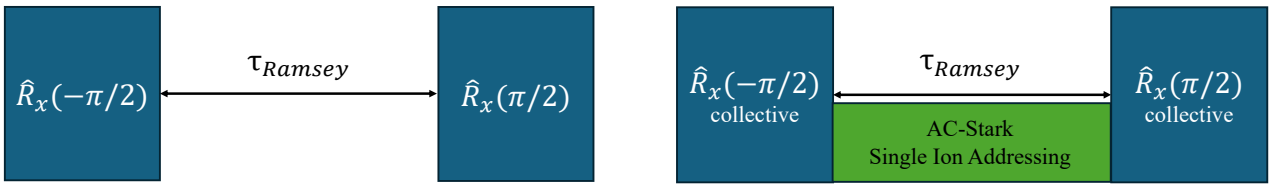
For Raman transitions satisfying the resonance condition $\delta_{\mathrm{R}} = 0$, the resulting population dynamics are identical to those shown in Fig. 2.15 for corresponding ratios $\delta_{\mathrm{R}}/\Omega_{\mathrm{R}}$. Consequently, the terminology of π and $\pi/2$ pulses remains unchanged.

iii) Composite pulse sequences:

As emphasized in Sec. 2.1, all single-qubit manipulations can be viewed as rotations on the Bloch sphere. Consequently, the various possible interactions with and evolutions of an ion can be mapped onto rotations within the Bloch sphere picture. By combining single-qubit rotations with periods of free precession in the equatorial plane of the Bloch sphere, composite pulse sequences can be constructed to realize effective π pulses. The mathematical equivalence of realizing a $\hat{\sigma}_x$ bit-flip gate operation for a single ion in the register using a composite pulse sequence (up to a global phase) is demonstrated by:

$$\begin{aligned} \hat{\sigma}_x \left|0\right\rangle &= i\, \hat{R}_x(\pi) \left|0\right\rangle \\ &= \hat{R}_z(-\pi)\, \hat{R}_x(-\pi/2)\, \hat{R}_z(\pi)\, \hat{R}_x(\pi/2) \left|0\right\rangle \\ &= \left|1\right\rangle . \end{aligned} \tag{2.6.1}$$

Thus, the bit-flip operation can either be implemented directly by driving resonant Rabi oscillations corresponding to a π rotation about the x axis, as shown in the first line of Eq. 2.6.1, or alternatively by bringing the qubit state to the equator of the Bloch sphere via a $\hat{R}_x(\pi/2)$ rotation. The state then undergoes free precession corresponding to an effective π rotation about the z axis, followed by a $\hat{R}_x(-\pi/2)$ rotation. The final $\hat{R}_z(-\pi)$ rotation compensates the phase accumulated during the free evolution. An equivalent operation is obtained for a free evolution of 2π, as well as for any even integer multiple of such free-evolution periods. Moreover, $\hat{R}_y$ rotations may be used instead of $\hat{R}_x$ to realize the same class of gate operations. Care must be taken, however, with respect to possible phase factors, which depend on the direction of evolution and the specific rotation sequence applied. The sequential $\pi/2$ rotations in Eq. 2.6.1 can be viewed as a Ramsey scheme, whose working principle is illustrated in Fig. 2.17(a).



(a) (b)

Fig. 2.17: (a): Ramsey scheme for implementing single-qubit gate operations on a single ion in the register. (b): Ramsey-like scheme with additional induced AC Stark shift on an addressed ion, enabling single-qubit gate operations in a multi-ion register.

Ramsey schemes are widely used in high-resolution spectroscopy, calibration in atomic clocks, and in the field of trapped-ion quantum computing, where they serve both to realize quantum gate operations and to perform quantum-metrology experiments [61]. The appropriate choice of the Ramsey waiting time, τ_{Ramsey}, is essential for such gate operations and must be calibrated for the specific energy splitting of the addressed transition.

As qubit registers necessarily consist of more than a single ion, it is essential to be able to perform operations in multi-ion registers. In addition to collective single-qubit manipulations, such a situation requires a means of individual addressing, typically realized using a far off-resonant addressing beam that induces an AC Stark shift on the selected ion [15]. Collective (global) manipulation acts uniformly on all qubits in the register. After all ionic qubits are brought into the equatorial plane of the Bloch sphere by a collective, resonant $\pi/2$ pulse, the selectively addressed ion undergoes the single-qubit gate operation.

During the Ramsey waiting time, the off-resonant addressing beam induces an AC-Stark shift on the addressed ion, thereby modifying its qubit transition frequency. In the rotating frame defined by the unshifted qubit frequency, the addressed ion therefore acquires an additional relative phase with respect to the unaddressed ions. The Ramsey waiting time τ_{Ramsey} and the addressing-beam intensity are calibrated such that this differential phase equals $\Delta\phi = \pi/2$, corresponding to an effective single-qubit $\hat{R}_z(\pi/2)$ rotation. A subsequent collective $\hat{R}_x(-\pi/2)$ pulse returns all unaddressed ions to their initial states, while the relative π phase accumulated by the addressed ion transfers it to the opposite pole of the Bloch sphere, corresponding to a population inversion with an additional phase factor. A final $\hat{R}_z(-\pi)$ rotation compensates this phase and completes the gate operation. The corresponding expression for describing the gate operation thus changes from Eq. 2.6.1 to:

$$\begin{aligned}\hat{\sigma}_x^{(i)}\,|00\ldots0\rangle &= \hat{R}^{(i)}_{z,\text{addressed}}(-\pi)\,\hat{R}_{x,\text{collective}}(-\pi/2)\,\hat{R}^{(i)}_{z,\text{addressed}}(\pi)\,\hat{R}_{x,\text{collective}}(\pi/2)\,|00\ldots0\rangle \\ &= |00\ldots01\rangle\ ,\end{aligned} \tag{2.6.2}$$

where, for illustrative purposes, the i-th addressed ion is chosen to be the last ion in the qubit register. A schematic representation of this procedure is shown in Fig. 2.17(b), in which the single-ion addressing induced AC-Stark shift during the Ramsey wait time corresponds to the rotation about the z axis. Alternatively, similar sequences can be realized using established techniques such as the Hahn echo sequence, which includes a spin-echo pulse centered within the waiting time and can significantly enhance coherence times [62].

2.6.2 Two-qubit gate operations

Entangling two-qubit gate operations require the state of one qubit to conditionally influence the evolution of a second qubit. In trapped-ion systems, this conditional interaction is mediated by the collective motional modes of the ion crystal, which couple the internal states of different ions. Depending on the physical mechanism by which this coupling is realized, three distinct approaches for implementing two-qubit operations are known and have been experimentally demonstrated to date. Specifically, these approaches comprise sideband gate schemes of the Cirac–Zoller type, geometric phase gate operations based on state-dependent optical forces such as the Mølmer–Sørensen (MS) gate, and gate operations exploiting qubit-state-dependent AC-Stark light shifts, which can be understood as a subclass of geometric phase gates in a broader sense [63].

Although Cirac–Zoller–type gate schemes allow the direct realization of a C-NOT operation through resolved sideband interactions, this approach relies on population transfer via the motional degrees of freedom and stringent cooling requirements [43]. In contrast, contemporary trapped-ion experiments predominantly employ symmetric geometric phase gates, which act identically on the participating qubits and therefore do not directly implement the asymmetric C-NOT gate operation commonly used in abstract quantum circuit representations. As a consequence, the C-NOT must be synthesized from a combination of platform-native entangling two-qubit gate operations and single-qubit rotations. This synthesis is illustrated in Fig. 2.18, which presents the standard C-NOT circuit depicted in Fig. 2.18(a), together with several equivalent circuit decompositions based on local basis transformations and gate operation identities, shown in Fig. 2.18(b)–2.18(d). These equivalences highlight that different entangling primitives can be combined with single-qubit rotations to realize the same two-qubit operation.

For light-shift (LS) gate implementations in trapped-ion quantum computing, the C-NOT operation is realized via a controlled-phase (C-Z) operation sandwiched between Hadamard operations on the target qubit, as shown in Fig. 2.18(c). Consequently, the following discussion focuses on this implementation, which directly reflects the experimentally realized entangling operation. The equivalence between the C-NOT gate and the Hadamard-transformed C-Z gate can be demonstrated using Eq. 2.1.20 in Sec. 2.1. Whenever the control qubit is in the state that activates the conditional operation, the target qubit undergoes the transformation:

$$\hat{\sigma}_x = \hat{H}\,\hat{\sigma}_z\,\hat{H}\ , \tag{2.6.3}$$

which maps the controlled-phase interaction onto a C-NOT operation. The C-Z gate constitutes a native two-qubit operation on the trapped-ion platform and can be realized via a geometric phase gate. LS gates directly generate a C-Z-type interaction proportional to $\hat{\sigma}_z \otimes \hat{\sigma}_z$, whereas MS gates implement an entangling interaction of the $\hat{\sigma}_x \otimes \hat{\sigma}_x$ form. Despite their different physical realizations, both gate schemes are locally equivalent and can be mapped onto a C-Z or C-NOT operation by applying appropriate single-qubit rotations [64, 65].

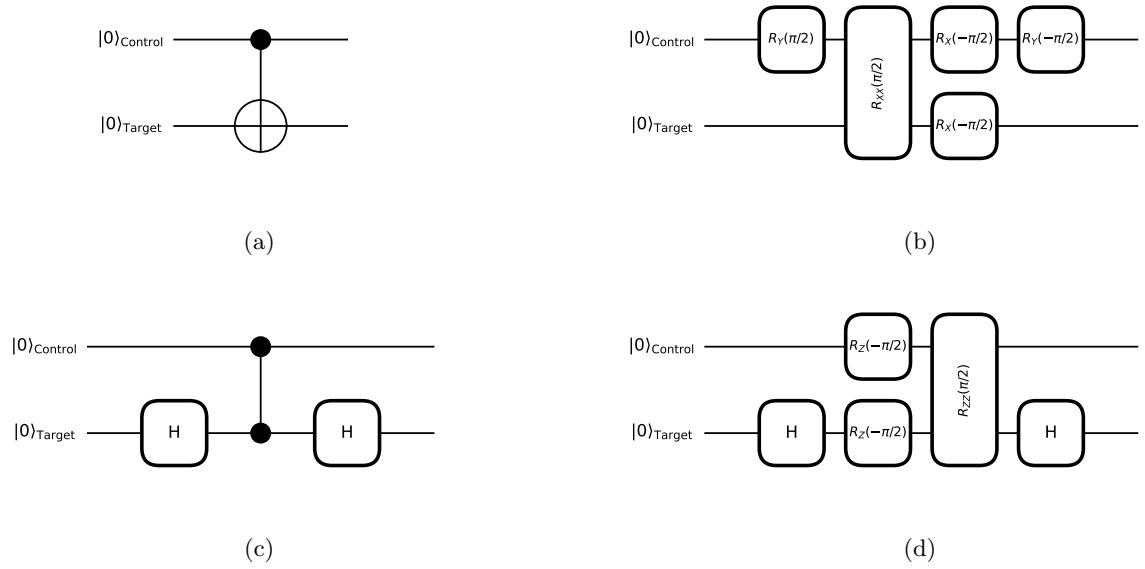


Fig. 2.18: Entangling C-NOT gate operation and equivalent circuit decompositions visualized using the PennyLane Python package [25]. (a): Standard quantum circuit representation of the C-NOT gate operation. (b): Equivalent realization of the C-NOT decomposed into a sequence of single-qubit rotations and a two-qubit $\hat{X}\hat{X}$ entangling interaction, which is typically used in a MS scheme. (c): Alternative equivalent implementation of the C-NOT gate using a CZ gate operation sandwiched between Hadamard operations on the target qubit. (d): Explicit rotation-based decomposition of the CZ gate seen in panel (c), highlighting the underlying two-qubit entanglement arising from a $\hat{Z}\hat{Z}$ interaction mechanism.

In both geometric phase gate schemes, a collective motional mode of the ion string is off-resonantly excited, giving rise to a qubit-state-dependent force that displaces the motional state from equilibrium in phase space. When the associated phase-space trajectories are closed, the motional degrees of freedom disentangle while specific two-qubit basis states acquire a conditional phase. In the MS scheme, this force is generated by simultaneously driving the red and blue motional sidebands in an off-resonant, bichromatic configuration. In contrast, in the LS scheme the force arises from qubit-state-dependent AC-Stark shifts induced by off-resonant addressing beams, which imprint the conditional phase via the shared motion of the ion crystal. The Hamiltonian of the LS gate can be written as

$$\hat{\mathcal{H}}_{\mathrm{LS}}(t) = \frac{\hbar\Omega\eta_j}{2}\left(\hat{a}_j e^{-i\delta_j t} + \hat{a}_j^\dagger e^{i\delta_j t}\right)\hat{S}_z \qquad \text{with } \hat{S}_z := \left(\hat{\sigma}_z^{(A)} + \hat{\sigma}_z^{(B)}\right) , \tag{2.6.4}$$

where δ_j denotes the detuning from the motional mode j [43]. From Eq. 2.6.4 it follows that the state-dependent force generated by the LS interaction is proportional to the eigenvalues of the spin operator $\hat{S}_z$:

$$\begin{aligned} \hat{S}_z\,|00\rangle &= +2\,|00\rangle & \hat{S}_z\,|01\rangle &= 0 \\ \hat{S}_z\,|11\rangle &= -2\,|11\rangle & \hat{S}_z\,|10\rangle &= 0\ . \end{aligned} \tag{2.6.5}$$

Consequently, only the even-parity states $|00\rangle$ and $|11\rangle$ experience a non-zero, qubit-state-dependent force, while the odd-parity states $|01\rangle$ and $|10\rangle$ remain unaffected by the spin operator. The opposite signs for $|00\rangle$ and $|11\rangle$ lead to phase-space displacements of opposite direction, which is the hallmark of the state-dependent force underlying the LS geometric phase gate.

The motional dynamics can be described using the displacement operator:

$$\hat{D}(\alpha_j(t)) = \exp\left(\alpha_j(t)\hat{a}_j^\dagger - \alpha_j^*(t)\hat{a}_j\right) , \tag{2.6.6}$$

where the complex time-dependent displacement amplitude $\alpha_j(t)$ traces a trajectory in a phase-space picture rotating at the detuning frequency δ_j [43]. For a time-dependent Rabi frequency $\Omega(t)$, the displacement

amplitude depending on motional mode j is in general given by:

$$\alpha_j(t) = \frac{\eta_j}{2} \int_0^t \Omega(t')\, e^{-i\delta_j t'}\, dt' \ . \tag{2.6.7}$$

The resulting phase-space trajectory, as well as the geometric phase accumulated along it during the LS gate operation, can be visualized in a frame of reference rotating at the detuning frequency δ_j, as shown in Fig. 2.19. By choosing the gate duration such that the motional displacement returns to the origin of phase space, the trajectory forms a closed loop, thereby ensuring disentanglement of the motional degrees of freedom at the end of the interaction. The colored and hatched areas enclosed by the loop correspond to the integral over the trajectory in phase space, which defines the entangling phase $\Theta(t)$, also called gate angle. This entangling phase has equal magnitude but opposite sign for the two even-parity states. The arrows indicate the direction of the phase-space trajectory $\alpha(t)$ along the loop.

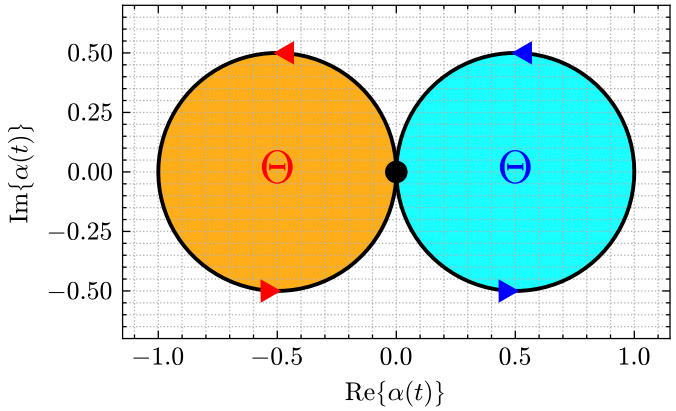


Fig. 2.19: Closed loops of displacement in rotating phase-space picture, through which motion disentangles. The accumulated phase is denoted by the gate angle Θ, which corresponds to the integral over the phase-space trajectory $\alpha(t)$.

The unitary LS gate-operator, $\hat{U}_{\mathrm{LS}}(t)$, can be derived from the time-dependent Schrödinger equation using the Magnus expansion for time-dependent Hamiltonians:

$$\hat{U}_{\mathrm{LS}}(t) = \exp\left(-\frac{i}{\hbar} \int_0^t \hat{\mathcal{H}}_{\mathrm{LS}}(t_1)\, dt_1 - \frac{1}{2\hbar^2} \int_0^t dt_1 \int_0^{t_1} dt_2 \left[\hat{\mathcal{H}}_{\mathrm{LS}}(t_1), \hat{\mathcal{H}}_{\mathrm{LS}}(t_2)\right] \right), \tag{2.6.8}$$

which accounts for the non-commuting nature of the Hamiltonian at different times and terminates exactly at second order, since all higher-order nested commutators vanish [43]. Eq. 2.6.8 evaluates to:

$$\hat{U}_{\mathrm{LS}}(t) = e^{i\Phi(t)\hat{S}_z^2}\, \hat{D}\Big(\alpha(t)\hat{S}_z\Big) \ , \tag{2.6.9}$$

where the first-order Magnus expansion provides an analytical expression for the phase-space trajectory:

$$\alpha_j(t) = \frac{\eta_j \Omega}{2\delta_j}\Big(1 - e^{i\delta_j t}\Big), \tag{2.6.10}$$

and the second-order term yields the geometric entangling (Magnus) phase function:

$$\Phi(t) = \left(\frac{\eta_j \Omega}{2\delta_j}\right)^2 \Big(\delta_j t - \sin(\delta_j t)\Big) \ . \tag{2.6.11}$$

At gate times $t_G = 2\pi/\delta_j$ the motional degree of freedom disentangles because $\alpha(t_G) = 0$, such that:

$$\hat{U}_{\mathrm{LS}}(t_G) = \exp\Big(i\Phi(t_G)\hat{S}_z^2\Big) = \exp\Big(i\Phi(t_G)\big[2\mathbb{I} + 2\,\hat{\sigma}_z^{(A)}\hat{\sigma}_z^{(B)}\big]\Big) \propto \exp\left(-i\frac{\Theta(t_G)}{2}\ \hat{\sigma}_z^{(A)} \otimes \hat{\sigma}_z^{(B)}/2\right)$$

$$= \begin{pmatrix} e^{-i\Theta(t_G)/2} & 0 & 0 & 0 \\ 0 & e^{+i\Theta(t_G)/2} & 0 & 0 \\ 0 & 0 & e^{+i\Theta(t_G)/2} & 0 \\ 0 & 0 & 0 & e^{-i\Theta(t_G)/2} \end{pmatrix} = \hat{U}_{\mathrm{LS}}(\Theta(t_G)) \ , \tag{2.6.12}$$

with the (time-dependent) geometric entangling phase defined as $\Theta(t) \coloneqq -4\Phi(t)$, such that $\Theta(t_G)$ is the accumulated two-qubit gate angle at the end of the gate interaction. The LS gate operator is implemented via an AC-Stark shift interaction, as described by Eq. 2.5.29.

The state evolution during the LS gate operation can be investigated numerically or analytically. Since the LS and MS gates are locally equivalent entangling operations, analytical expressions derived for the MS gate can be applied to the LS interaction after appropriate $\pi/2$ basis rotations, which map the $\hat{\sigma}_x$ interaction of the MS gate onto the $\hat{\sigma}_z$ interaction underlying the LS gate. For an idealized gate operation in the Lamb–Dicke regime, the time-dependent populations of the two-qubit basis states can then be written as:

$$\begin{aligned} P_{gg}(t) &= \frac{3}{8} + \frac{1}{2}e^{-2|\alpha(t)|^2}\cos\big(\Theta(t)\big) + \frac{1}{8}e^{-8|\alpha(t)|^2} \\ P_{ee}(t) &= \frac{3}{8} - \frac{1}{2}e^{-2|\alpha(t)|^2}\cos\big(\Theta(t)\big) + \frac{1}{8}e^{-8|\alpha(t)|^2} \\ P_{ge}(t) &= P_{eg}(t) = \frac{1}{8}\left(1 - e^{-8|\alpha(t)|^2}\right) \ , \end{aligned} \tag{2.6.13}$$

where $|\alpha(t)|$ denotes the magnitude of the motional displacement, and the logical basis is defined as $|0\rangle \equiv |e\rangle$ and $|1\rangle \equiv |g\rangle$. These expressions for the quantum state populations are derived explicitly in Ref. 66. In the analytical simulation, applying the LS gate operation to a pair of ions prepared in the electronic state $|gg\rangle \equiv |11\rangle$ results in the state evolution shown in Fig. 2.20. After one and three gate times, the trajectories of the spin-dependent displacement in the rotated phase space form closed loops. At these times, the motional degrees of freedom disentangle from the internal states, and the effective entangling operation underlying the C-NOT decomposition shown in Fig. 2.18(c) is physically realized.

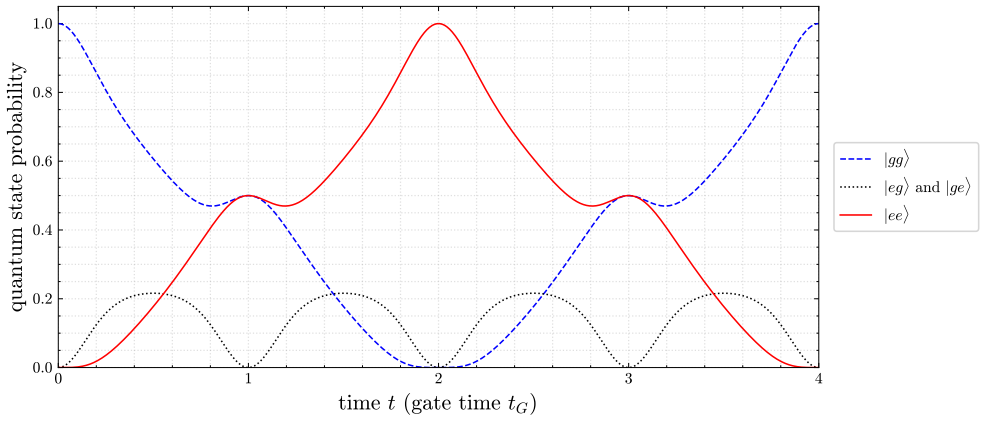


Fig. 2.20: Analytical simulation of the quantum-state evolution during an LS gate operation. Parameters: $\eta_j = 0.05$, $\Omega/2\pi = 100\,\text{kHz}$, and detuning from the considered motional mode $\delta = 20\,\text{kHz}$. At one and three gate times respectively, the system ideally reaches the Bell state $|\Phi^+\rangle$ and is decoupled from the motion, since the displacement trajectories in the phase-space representation form closed loops.

The complementary pair of odd-parity quantum states can be driven by modifying the LS gate operation such that the qubit of subsystem B is flipped before the LS interaction and mapped back immediately afterwards. This mapping corresponds to conjugating the LS gate operator of Eq. 2.6.12 by a Pauli-$\hat{X}$ operation on qubit B:

$$\begin{aligned} \hat{U}_{\text{LS,odd}}(\Theta) &= (\hat{I} \otimes \hat{X})\,\hat{U}_{\text{LS}}(\Theta)\,(\hat{I} \otimes \hat{X}) \\ &= \exp\left(+i\,\frac{\Theta}{2}\,\hat{\sigma}_z^{(A)}\hat{\sigma}_z^{(B)}\right) \ . \end{aligned} \tag{2.6.14}$$

The pairs of quantum states that are not actively driven by the LS gate operation, for which the displacement magnitude remains zero, still acquire a geometric phase during the interaction. At gate times corresponding to maximal entanglement, this accumulated phase leads to destructive interference in the population amplitudes of the non-driven states, such that their probabilities theoretically vanish and experimentally are suppressed.

2.6.3 Transverse light-shift gate operation

This approach is based on the optical dipole (gradient) force, Eq. 2.5.38, and thus relies on the same physical principle as optical tweezers and earlier implementations based on intensity gradients [67, 65]. As a minimal example of how a transverse gradient force can be generated relative to the propagation direction of the addressing beam, one may consider a single Gaussian TEM_{00} addressing beam incident along the radial trap direction. Fig. 2.21 illustrates the relative alignment between the optical addressing field and a single ion for this basic configuration, which enables axial gate operations orthogonal to a radially propagating addressing beam via the optical gradient force. Since the axial motional modes are more widely spaced than their radial counterparts, the spectral overlap between the addressed mode and neighboring modes is reduced, which allows for higher gate fidelities due to suppressed addressing errors of motional modes [68].

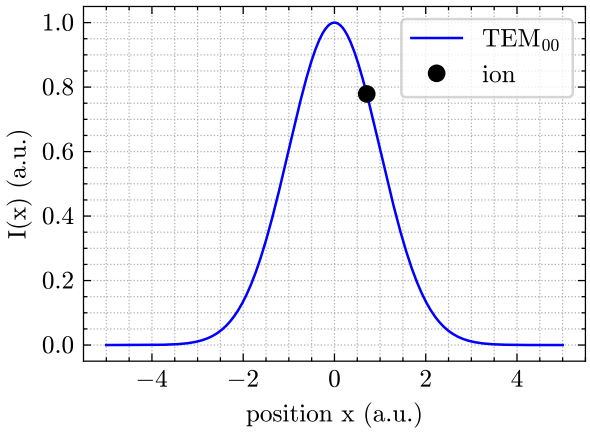


Fig. 2.21: Alignment used to realize transverse gate operations. The ion is positioned at the point of maximal intensity gradient, enabling axial manipulation via the optical dipole (gradient) force. For a single fundamental Gaussian addressing beam, the point of strongest gradient occurs at $z = z_0 \pm \sigma = \pm\sigma$ ($z_0 = 0$).

For a red-detuned optical dipole force, the ion is pulled toward the point of highest intensity, whereas for blue detuning it is pushed away from this point. Since the radial addressing beam is far off-resonant, it induces an AC-Stark shift whose sign depends on both the detuning and the local intensity gradient. A periodical intensity modulation of the TEM_{00} addressing beam makes the ion experiences a time-dependent AC-Stark shift, allowing controlled coupling to the axial motional modes.

In the new, transverse LS gate implementation, no collective standing wave is generated across the ion chain [69]. Instead, a superposition of TEM_{00} and TEM_{10} modes is employed, which locally forms an effective standing wave only at the position of the addressed ion(s). This configuration enables fully orthogonal addressing, motivating the term transverse.

By detuning the relative frequencies of the involved laser fields, the superposition beats at the sum of the axial trap frequency and an additional detuning from the selected motional mode j, $\omega_{\mathrm{beat}} = \omega_{\mathrm{axial}} + \delta_j$. This approach maximizes the achievable intensity gradient while requiring less spatial extent than a single-beam configuration, thereby reducing addressing errors caused by overlap with neighboring ions. The superposition creates a field along the axial trap direction (x), transverse to the beam propagation (z):

$$E_{\mathrm{tot}}(x) \propto [E_0 \boldsymbol{\epsilon}_0 + \sqrt{2} E_1 \boldsymbol{\epsilon}_1 (x - x_0) e^{-i\Delta\phi}] \cdot e^{-\frac{(x-x_0)^2}{2\sigma^2}}, \tag{2.6.15}$$

with $\Delta\phi \coloneqq \omega_{\mathrm{beat}}\, t = (\omega_{\mathrm{TEM}_{00}} - \omega_{\mathrm{TEM}_{10}})\, t$ being the relative phase mismatch of involved laser frequencies and $\boldsymbol{\epsilon}_i$ the polarization unit vector of respective light field. In the ideal case both focal planes meet exactly at the plane of the ion chain to form the superposition of TEM_{00} and TEM_{10} Hermite-Gauss modes. A field superposition of the form seen in Eq. 2.6.15 leads to a resulting intensity of:

$$\begin{aligned} I_{\mathrm{tot}}(x) &= |E_{\mathrm{tot}}(x)|^2 \\ &= [|E_0|^2 + 2|E_1|^2 (x - x_0)^2 + 2\sqrt{2} E_0 E_1 (x - x_0) \underbrace{\cos\left(\angle(\boldsymbol{\epsilon}_0, \boldsymbol{\epsilon}_1)\right)}_{\text{overlap in pol.}} \cos(\Delta\phi)] \cdot e^{-\frac{(x-x_0)^2}{\sigma^2}} . \end{aligned} \tag{2.6.16}$$

Additionally, the scattering error is proportional to the ratio of the individual field strengths involved in the superposition ($\propto E_0/E_1$), which provides an additional parameter for minimizing the total error

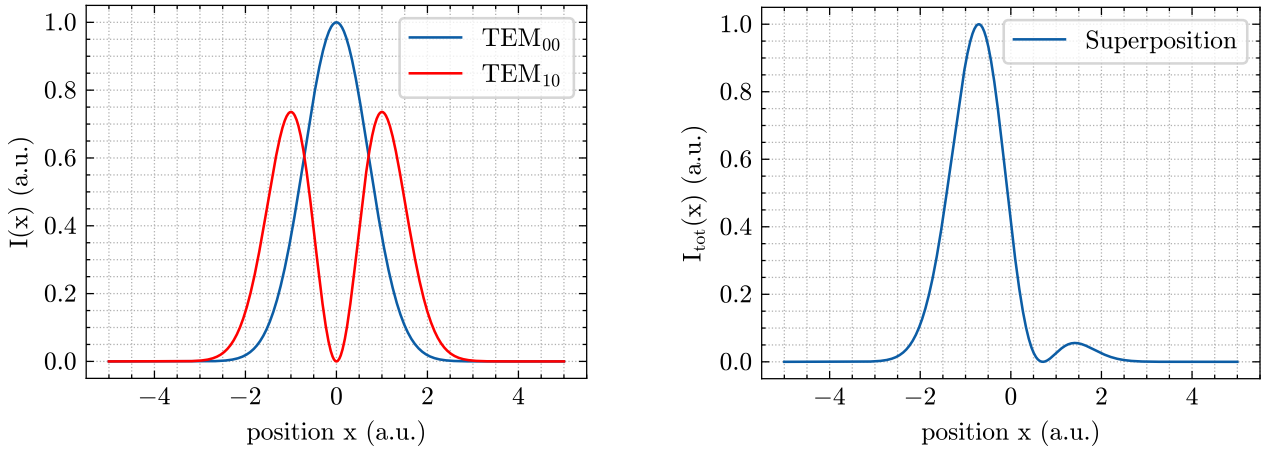
budget, including addressing-related errors such as crosstalk and photon scattering [70, 71]. The ratio of the individual field strengths also determines where the slope reaches the maximum as well as the point of destructive interference to zero. These points of local maxima, minima and strongest gradients are crucial to realize the periodic AC-Stark shifts to generate the intended geometric phase. The points of destructive interference correspond to positions where the local optical field amplitude vanishes. For parallel polarizations ($\cos(\angle(\boldsymbol{\epsilon}_0, \boldsymbol{\epsilon}_1)) = 1$), this condition can be obtained directly from the field superposition in Eq. 2.6.15 by requiring:

$$E_{\text{tot}}(x) = 0 \ . \tag{2.6.17}$$

Neglecting the Gaussian envelope when locating the local extrema and setting $x_0 = 0$ yields:

$$x_{\pm} = \pm \frac{E_0}{\sqrt{2}E_1} \ , \tag{2.6.18}$$

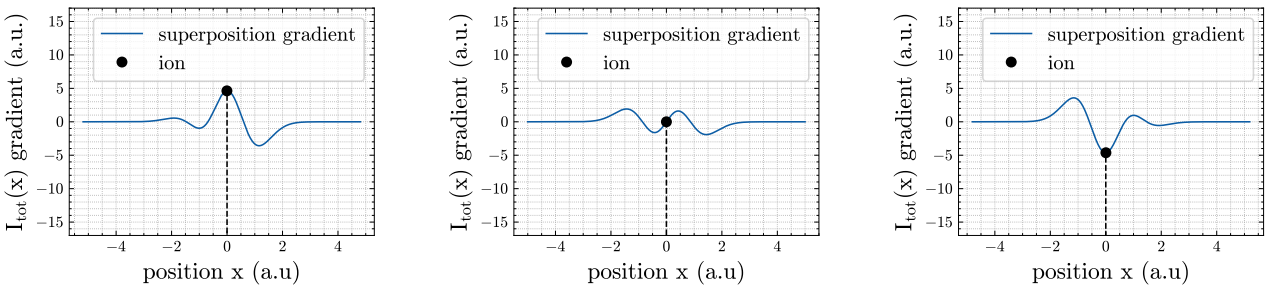
for the positions of destructive interference and relative phase differences $\Delta\phi \in \{0, \pi\}$. At these locations the optical intensity vanishes while the local intensity gradient is maximized for a relative phase shift of π, enabling the generation of a strong state-dependent optical dipole force. Only for the choice $E_0 = E_1$, the point of strongest gradient equals the point of destructive interference with zero intensity for a phase shift of $\Delta\phi = \pi$. Fig. 2.22 shows the individual and the resulting superposition intensities.



(a) (b)

Fig. 2.22: (a) Individual intensities of the TEM_{00} and TEM_{10} modes. (b) Resulting intensity of superposition for a given phase difference of $\Delta\phi = 0$.

The process of the transverse LS gate operation can also be visualized by plotting the gradient of the superposition intensity directly for different moments of time, seen in Fig. 2.23. In Fig. 2.23(a) we are on one extreme of the motion and the ion is pushed with a phase difference between axial trap frequency and beat note of $\Delta\phi = 0$.



(a) (b) (c)

Fig. 2.23: Gradient of the resulting superposition for different relative phase differences, shown in direct correspondence to the ion's axial motion in the trap ($\omega_{\text{beat}} = \omega_{\text{axial}}$). (a): Gradient of superposition with $\Delta\phi = 0$. (b): Gradient of the superposition for $\Delta\phi = \pi/2$. (c): Gradient of the superposition for $\Delta\phi = \pi$.

In the equilibrium position of the ion's axial oscillation, seen in Fig. 2.23(b), the phase difference of the superposition shifts to $\Delta\phi = \pi/2$ and the gradient equals zero. The ion does not experience an AC-Stark shift

gradient and therefore no gradient force. In Fig. 2.23(c) we are on the opposite extreme of the ion's pendulum motion and the phase difference of the superposition intensity equals $\Delta\phi = \pi$. The ion is pulled toward the maximal gradient as the sign of the gradient changed and thus the direction of the optical dipole force. Since the axial motion is quantized, the gradient force directly couples to the motional energy eigenstates.

The action of a LS interaction on the ionic level can be understood by considering the mathematical description of the gate operation sequence as implemented on the experiment, which resembles the circuit in Fig. 2.18(c) but with the Hadamards being replaced by rotations around the x axis of the Bloch sphere:

$$\begin{aligned}
|\Psi\rangle_{\text{final}} &= \left(\hat{R}_x^{(A)}(-\pi/2) \otimes \hat{R}_x^{(B)}(-\pi/2)\right) \hat{U}_{\text{LS}}(\Theta) \left(\hat{R}_x^{(A)}(\pi/2) \otimes \hat{R}_x^{(B)}(\pi/2)\right) |11\rangle_{AB} \\
&= \frac{1}{2} \left(\hat{R}_x(-\pi/2) \otimes \hat{R}_x(-\pi/2)\right) \hat{U}_{\text{LS}}(\Theta) \left[-|00\rangle - i|01\rangle - i|10\rangle + |11\rangle\right] \\
&= \frac{1}{2} \left(\hat{R}_x(-\pi/2) \otimes \hat{R}_x(-\pi/2)\right) \left[e^{-i\Theta/2}\big(|11\rangle - |00\rangle\big) - ie^{+i\Theta/2}\big(|01\rangle + |10\rangle\big)\right] \\
&= \cos(\Theta/2)\,|11\rangle + i\sin(\Theta/2)\,|00\rangle \ . \qquad (2.6.19)
\end{aligned}$$

which for an entangling phase of $\Theta = \pi/2$ yields the Bell state $|\Phi^+\rangle$ of Eq. 2.1.24 up to a correctable phase factor in $|00\rangle$. This erroneous phase originates from the use of $\hat{R}_x$ rotations instead of Hadamards, and although it does not change the population, it must be accounted for further computational processes.

Chapter 3

Qubit considerations

This chapter discusses two ionic species commonly employed in trapped-ion quantum computing, $^{40}Ca^{+}$ and $^{138}Ba^{+}$. The atomic and molecular physics concepts required to evaluate and compare their suitability as qubit encodings are introduced. Certain encoding strategies can substantially enhance coherence and lifetime parameters. A prominent example is qubit encoding in hyperfine ground states, which can exhibit lifetimes extending to many days and may therefore be regarded as effectively infinite on experimental timescales [72, 73]. Despite these advantages, the discussion in this chapter is restricted to optically encoded qubits, that is, qubit encodings based on transitions in the optical domain. This choice reflects the experimental context of the present work, in which optical qubits offer straightforward individual ion addressing, fast gate operations enabled by large transition frequencies [43, 19]. Restricting the discussion to optical encodings therefore allows a direct and consistent comparison between $^{138}Ba^{+}$, which is used in the experiment, and the widely employed $^{40}Ca^{+}$ system.

3.1 Qubits with calcium ions ($^{40}Ca^{+}$)

Hydrogen-like ionic species, i.e. ions that possess a single valence electron after ionization, are commonly used as working species, since they exhibit a comparatively simple electronic level structure. In trapped-ion quantum computing, such hydrogen-like configurations are typically realized using alkaline earth elements (second main group of the periodic table), like calcium or barium, which become hydrogen-like after the removal of a single electron. These ions combine a simple electronic structure with experimentally accessible optical transitions, making them particularly suitable for quantum control.

Although all alkaline earth elements share this electronic structure after single ionization, their physical properties can differ substantially. In particular, the internal electronic states of different ion species exhibit different lifetimes T_1, and therefore different natural linewidths $\Gamma = 1/T_1$. The lifetime T_1, also known as relaxation time, plays a crucial role in quantum information processing, as it sets a fundamental upper bound on the time available for coherent quantum operations: all manipulations must be completed well within this timescale to avoid information loss due to spontaneous decay. The associated natural linewidth Γ directly determines the spectral resolution of optical transitions. Long-lived states correspond to narrow linewidths, which allow for highly frequency-selective addressing of individual transitions and reduce off-resonant excitation of nearby levels [58]. This is particularly important in multi-level atomic systems, where undesired couplings can lead to leakage errors or additional decoherence channels [43]. Conversely, short-lived excited states exhibit broad linewidths, which facilitate fast optical pumping and state preparation, but at the same time limit the achievable coherence and impose stricter constraints on gate durations and laser stability [43]. As a result, the choice of ion species and electronic transition involves a trade-off between long coherence times, spectral selectivity, and practical requirements such as achievable laser power and technical noise. These considerations play a central role in determining the suitability of a given ion species for high-fidelity quantum gate operations.

In addition to population relaxation and linewidth, the coherence time T_2 is a key figure of merit and can vary significantly between ion species. This variation arises, for example, from different sensitivities of the electronic states to magnetic-field fluctuations, which are governed by the coupling of the electronic angular momentum to external magnetic fields [74, 75]. Even for a fixed ion species, the achievable coherence time depends strongly on the experimental environment, including laser phase noise and ambient magnetic-field noise. In the absence of technical noise and for sufficiently long T_1, the coherence time is limited only by pure

dephasing, T_ϕ, according to [76]:

$$\frac{1}{T_2} = \frac{1}{2T_1} + \frac{1}{T_\phi} \ . \tag{3.1.1}$$

A central challenge in trapped-ion quantum computing, shared with the neutral-atom platform, is therefore the careful selection not only of a suitable ion species, but also of the specific electronic states used for qubit encoding and auxiliary operations. The chosen transitions must be experimentally feasible: a long-lived state is of limited practical value if it cannot be reliably addressed with available laser technology. Furthermore, atomic selection rules must be considered to identify whether transitions are electric-dipole allowed, quadrupole allowed, or forbidden, and to determine the possible decay channels of excited states. In this context, branching ratios (BRs) play an important role whenever multiple electronic transitions are available. The electronic configuration of $^{40}Ca^+$ is given by:

$$\begin{aligned} [^{40}_{20}Ca^+] &= 1s^2\, 2s^2p^6\, 3s^2p^6\, 4s^1 \\ &= [^{40}_{18}Ar]\, 4s^1 \end{aligned} \tag{3.1.2}$$

and can be found in standard textbooks or derived using the Bohr–Sommerfeld atomic model, the Pauli principle, and Hund's rules [77]. The configuration gives information about which orbitals are filled, but also about the energetic closest ones that are still unoccupied. Using these insights and concepts like the fine-structure (also commonly known as l-s coupling), one can create an energetic level diagram in order to visualize the possible transitions for the single valence electron [78]. For $^{40}Ca^+$ this leads to an energy-level diagram as shown in Fig. 3.1.

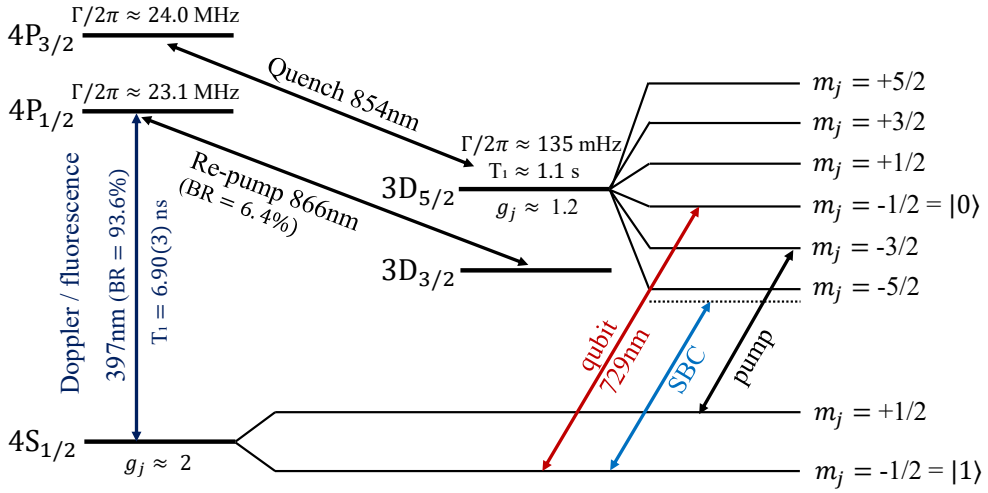


Fig. 3.1: Energy level diagram of $^{40}Ca^+$ with all relevant transitions that are (usually) used. Furthermore all relevant parameters like branching ratios (BR), Landé g-factors (g_j), linewidths (Γ) and thus also relaxation times (T_1) are included therein [79, 80, 81].

The optical qubit is encoded between the ground-state 4S1/2 manifold and the metastable 3D5/2 manifold and is coherently coupled with resonant 729 nm light [82]. The principles of state preparation, readout and cooling stay qualitatively the same as explained in Sec. 2.4 for the case of $^{138}Ba^+$. The specific electronic states used and therefore also linewidths and wavelengths change, however. As $^{40}Ca^+$ is a commonly used ion species for trapped ion quantum computing, there have been numerous investigations of lifetimes as well as coherence times. In Ref. [81] the lifetime of the metastable state was shown to be approximately 1.1 s, which is in good agreement to the theoretical value. The achievable coherence time depends on the specific experimental setup, including the linewidths of the involved lasers and the ambient noise conditions. Reported coherence times T_2 typically lie in the range 10 ms - 100 ms, without spin-echo pulses, which may increase coherence times significantly [62, 83].

For related experiments working with calcium, the chosen transition scheme implies the possibility of radial single ion addressing with coherent 729 nm light directly. With this wavelength, it is still possible to focus the beam to sufficiently small spot sizes ($\approx 1\,\mu m$), such that the addressing beam fits between neighboring ions and no significant addressing error is introduced. The inter-ion spacing is typically of the order of 3 µm to 5 µm, corresponding to axial trap frequencies (in the case of calcium) of approximately 600 kHz to 1.3 MHz [83]. The usage of coherent light for radial addressing generally restricts access to axial motional modes, since momentum

transfer occurs predominantly along the beam propagation direction, unless the radial addressing is realized under an angle that provides access to the axial modes. Another advantage for experiments working with $^{40}Ca^+$ qubits is given by the circumstance that all optical transitions involved have reliable, commercial laser systems available, owing to the long-standing experimental use of $^{40}Ca^+$ in trapped-ion research.

Despite its widespread use and well-understood level structure, $^{40}Ca^+$ also exhibits several disadvantages for scalable trapped-ion quantum computing. Most notably, the optical qubit encoded on the narrow $4S_{1/2}$–$3D_{5/2}$ electric-quadrupole transition at 729 nm is intrinsically sensitive to laser phase noise and magnetic-field fluctuations, thereby limiting the achievable coherence time in the absence of dynamical decoupling techniques [15]. Furthermore, the finite lifetime of the metastable $3D_{5/2}$ state imposes an upper bound on idle times and long gate sequences [81]. From an experimental perspective, the use of a quadrupole transition requires comparatively high optical intensities and excellent beam-pointing stability, which increases technical complexity and sensitivity to alignment drifts. These limitations motivate the investigation of alternative ion species and qubit encodings that offer longer intrinsic coherence times and reduced susceptibility to technical noise [43].

3.2 Qubits with barium ions ($^{138}Ba^+$)

The $^{138}Ba^+$ ion is significantly heavier than $^{40}Ca^+$ and, owing to its higher atomic number, possesses a larger number of electrons that occupy inner atomic shells. Despite this increased electronic complexity of the core, $^{138}Ba^+$ retains a hydrogen-like structure for the valence electron and is therefore well suited for quantum control. The electronic configuration of the $^{138}Ba^+$ ion is given by:

$$\begin{aligned}\left[^{138}_{56}\mathrm{Ba}^+\right] &= 1s^2\,2s^2p^6\,3s^2p^6d^{10}\,4s^2p^6d^{10}\,5s^2p^6\,6s^1 \\ &= \left[^{131}_{54}\mathrm{Xe}\right]\,6s^1\ ,\end{aligned} \tag{3.2.1}$$

where the closed-shell xenon core is inert for the optical transitions relevant to quantum information processing. The resulting energy-level diagram, together with the transitions typically employed for quantum information processing, is shown in Fig. 3.2. The working principles of state preparation, readout, and laser cooling for $^{138}Ba^+$ ions are discussed in detail in Sec. 2.4 and are therefore not repeated here.

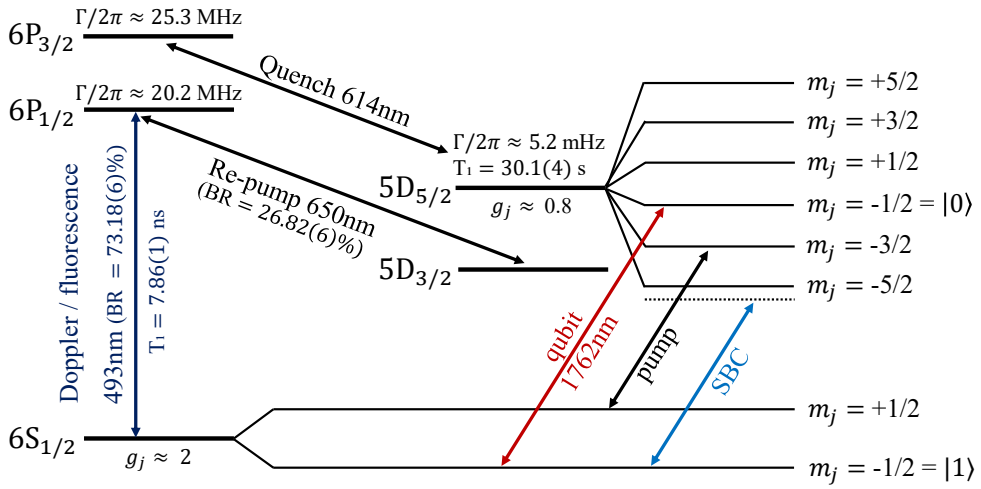


Fig. 3.2: Energy level diagram of $^{138}Ba^+$ with all relevant transitions that are usually used. Furthermore all relevant parameters like branching ratios (BR), Landé g-factors (g_j), linewidths (Γ) and thus also relaxation times (T_1) are included therein [48, 49, 84].

When comparing the energetic level structure and relevant parameters of $^{40}Ca^+$ and $^{138}Ba^+$, pronounced differences emerge within the wavelengths of the employed optical transitions. The Doppler-cooling wavelength of 493 nm in barium, for instance, is significantly less blue than the corresponding transition in calcium. This represents a practical advantage, since laser diodes in the deep-blue spectral range are more challenging to realize and typically exhibit inferior long-term stability compared to diodes operating in other regions of the visible spectrum [43]. Therefore, wavelengths farther from the ultraviolet (UV) spectrum are of interest for scalable integrated photonic systems, as they can facilitate stable long-term light delivery.

A second, more consequential difference concerns the qubit-encoding transition at 1762 nm. The wavelength associated with this transition is comparable to the typical inter-ion spacing in linear ion chains and, owing to the

diffraction limit of the Airy disk, renders efficient radial single-ion addressing via resonant light fundamentally infeasible without incurring substantial addressing errors [85]. Eq. 2.2.10 implies a diffraction-limited spot size of approximately 2.7 µm for 1762 nm. While this value appears sufficiently small at first glance, only about 86 % of the total optical power is contained within the minimal waist w_0 [27, 49]. Consequently, the achievable confinement is insufficient for high-fidelity single-ion addressing. In ion-chain experiments with barium qubits, the use of off-resonant light therefore becomes unavoidable, and gate operations are implemented via Raman transitions or sequential rotations based on the AC-Stark shift rather than coherently driven resonant Rabi oscillations.

A major advantage of barium qubits becomes apparent when considering the relevant relaxation time scales. For $^{138}Ba^+$, the excited-state lifetime T_1 is approximately 31 s, which constitutes an improvement by roughly a factor of 30 compared to $^{40}Ca^+$ [84]. In the present experiment, the coherence time T_2 for $^{138}Ba^+$ is on the order of 200 ms (without spin-echo). Even more favorable lifetimes are found in other barium isotopes. The isotope $^{137}Ba^+$, for example, possesses a non-zero nuclear spin $I = 3/2$, giving rise to hyperfine structure through spin–spin coupling. These hyperfine states can be used for qubit encoding with a practically infinite lifetime and fewer leakage channels, since they exhibit a less complex energy-level structure [77, 72, 73]. However, factors other than the lifetime alone must also be taken into account. For example, $^{133}Ba^+$ also offers hyperfine levels, but this isotope is weakly radioactive, with a half-life time of 10.51 years [86]. As a result, it is subject to regulatory constraints, such as the Austrian "Strahlenschutzverordnung 2020" (StrSchV 2020), which reduces its attractiveness for laboratory research and prospective commercial quantum-computing applications.

The magnetic-field sensitivity of both qubit species discussed in this chapter is, to first order, governed by the linear Zeeman effect. In the presence of an external magnetic field, the coupling of the electron's orbital and spin angular momenta leads to a splitting of the atomic energy levels. The magnitude of this splitting is determined by the Landé g-factor, which characterizes the coupling strength between the ion's total angular momentum and an external magnetic field $\mathbf{B}$ [77]. When the magnetic field defines the quantization axis of the angular momentum, the resulting shift of the transition frequency can be written as:

$$\Delta E = \Delta\mu \, |\mathbf{B}| = (g_{j,0}\, m_0 - g_{j,1}\, m_1)\, \mu_B \, |\mathbf{B}| = h\, \Delta\nu \ , \tag{3.2.2}$$

where $g_{j,i}$ denotes the Landé g-factor of state i, m_i the corresponding magnetic quantum number, μ_B the Bohr magneton, h the unreduced Planck constant, and $\Delta\nu$ the resulting frequency shift. Using the Landé g-factors shown in Fig. 3.1 for $^{40}Ca^+$ and Fig. 3.2 for $^{138}Ba^+$, Eq. 3.2.2 yields the magnetic-field sensitivities illustrated in Fig. 3.3. The slopes of the curves define the transition-frequency sensitivity $\alpha = \partial\nu/\partial B$, expressed in units of MHz G^{-1}. For the chosen encodings, $^{40}Ca^+$ exhibits a smaller sensitivity of $\alpha \approx 0.56$ MHz G^{-1}, while $^{138}Ba^+$ shows a larger value of $\alpha \approx 0.84$ MHz G^{-1}. Consequently, calcium qubits are intrinsically less sensitive to magnetic-field fluctuations, whereas the increased sensitivity of the barium qubit constitutes an important limitation of the chosen encoding.

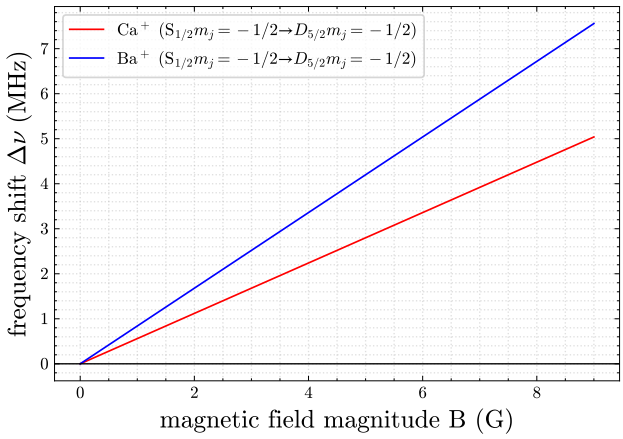


Fig. 3.3: Visualization of the frequency shifts induced by the linear Zeeman effect for the $^{138}Ba^+$ and $^{40}Ca^+$ qubits, using a state encoding shown in Fig. 3.2 and Fig. 3.1, respectively.

The optical linewidths Γ of the qubit transitions in both $^{138}Ba^+$ and $^{40}Ca^+$ are narrow, which is advantageous in terms of long state lifetimes, since these scale inversely with Γ. At the same time, such narrow linewidths impose stringent requirements on the frequency stability of the driving laser fields, as even minute frequency fluctuations translate directly into accumulated phase noise of the optical qubit. The laser systems must therefore ideally address optical transitions at several hundred THz with uncertainties reaching the single-digit mHz regime in the case of $^{138}Ba^+$ [15, 43].

Chapter 4

Experimental setup

This chapter provides an overview of the experimental setup, with particular emphasis on the imaging system and the single-ion addressing, as well as on the alignment of the involved light fields. The acousto-optic deflector (AOD), which enables controlled beam steering for individual-ion addressing, is introduced together with the underlying principles of its operation. The addressing units themselves are described in the following chapter (Chap. 5). Furthermore, the control breadboard responsible for light distribution and for driving the addressing units, thereby enabling qubit manipulations on the ions, is presented.

4.1 Overview and laser alignment

In Fig. 4.1, a schematic of the opto-mechanical setup of the experiment as implemented on the optical table is shown. The two addressing units are arranged symmetrically so that both addressing beams propagate over equal distances before being imaged onto the ions by a high-NA microscope objective.

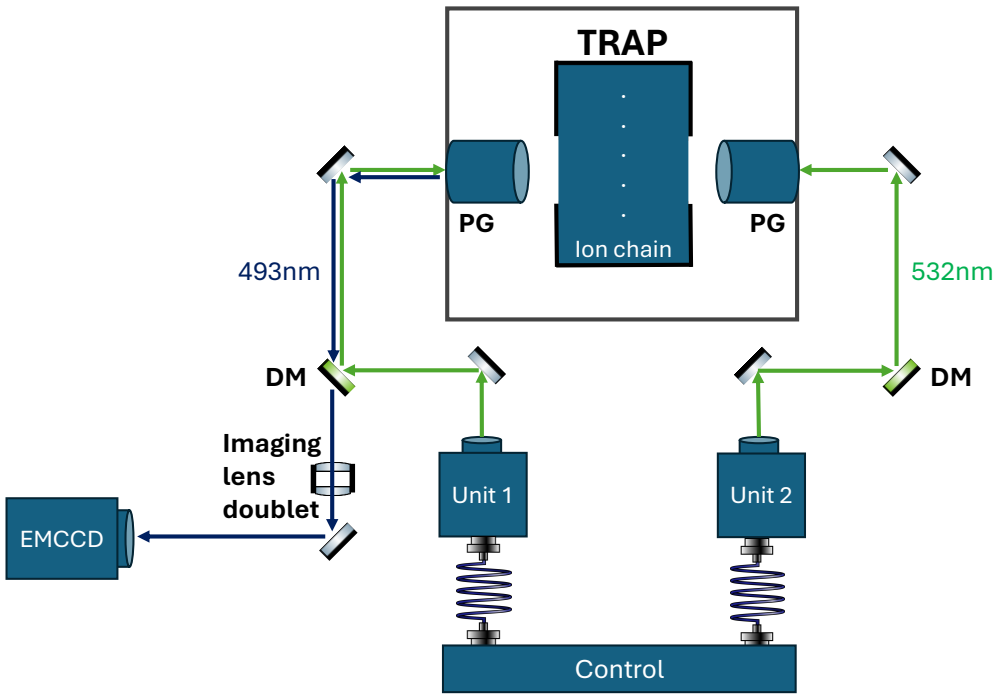
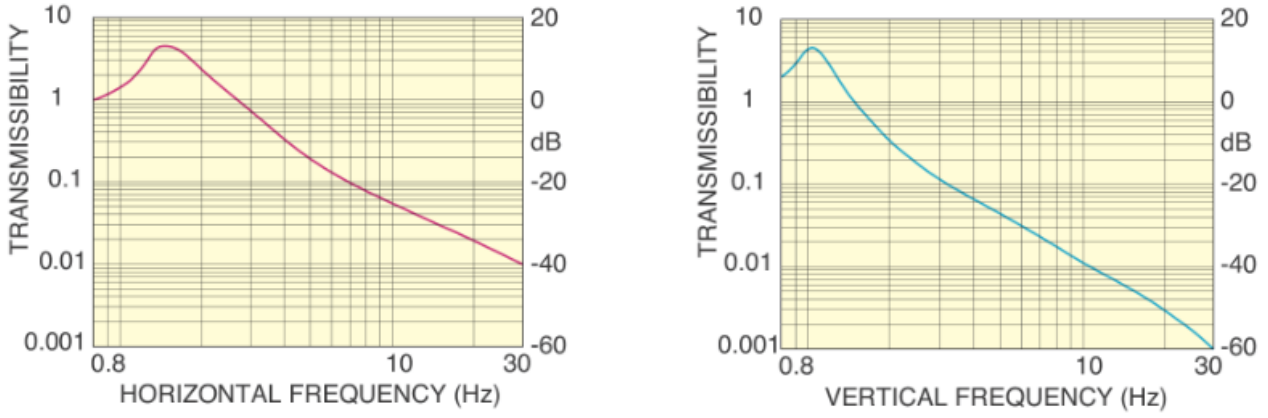


Fig. 4.1: Top-view schematic of the optical layout and trap region of the experiment. The individual addressing beams at 532 nm of the double-sided counter-propagating addressing system, as well as the 493 nm fluorescence used for state-dependent readout, are depicted. Relevant optical components of the addressing and imaging systems, together with their respective beam paths, are indicated by color. The viewports on both sides of the trap are marked by interrupted lines of the trap enclosure. Abbreviations: PG – high-NA microscope objective manufactured by Photon Gear; DM – dichroic mirror; EMCCD – electron-multiplying charge-coupled device.

A dichroic mirror (DM) enables both fluorescence detection and ion addressing from the same direction, allowing parts of the optical paths to be shared. The DM reflects the 532 nm addressing beam while transmitting the 493 nm fluorescence light. Following the DM, a lens doublet focuses the image onto the sensor array, which consists of an electron-multiplying charge-coupled device (EMCCD), completing the opto-mechanical imaging system. The fluorescence photons are detected by the EMCCD camera, which converts the incoming photons into electrons and amplifies them such that the recorded electron counts can be traced back to individual photon events. In this experiment, a commercially available Andor camera[1] is used. The sensor chip of this camera model is cooled to approximately $-90\,^{\circ}\mathrm{C}$ to reduce dark counts, i.e. registered events that are not caused by incident photons.

The external magnetic field defining the quantization axis and lifting the Zeeman degeneracy is oriented along the optical addressing axis (radial trap dimension) [43, 15]. Permanent magnets in a Helmholtz configuration are installed around both viewports to produce a uniform magnetic field of approximately 4.5(1) G. The ion-trap chamber of the experiment is mounted on an air-floated optical table equipped with pneumatic vibration isolators[2]. This mechanical isolation is employed to suppress the transmission of environmental vibrations to the trapping apparatus, thereby stabilizing both the ion positions and the alignment of the optical systems. Fig. 4.2 shows the measured vibration transmission as a function of frequency for both the horizontal and vertical directions, illustrating the effective attenuation provided by the isolation system over the relevant frequency range.



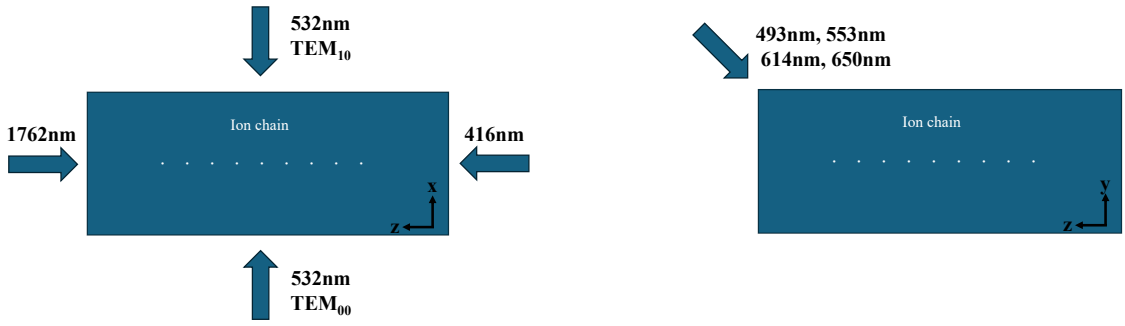
(a) (b)

Fig. 4.2: Quantification of the vibration-isolation performance of the pneumatic isolator system, as provided by the manufacturer on the product webpage [87]. (a) Horizontal isolation response with a resonance frequency of 1.5 Hz and approximately 9 dB amplification at resonance, achieving 95 % isolation at 10 Hz. (b) Vertical isolation response with a resonance frequency of 1 Hz and approximately 10 dB amplification at resonance, achieving 98 % isolation at 10 Hz.

In addition to mechanical isolation, the ion chamber is operated under ultra-high-vacuum (UHV) conditions at a pressure of approximately 1×10^{-11} mbar. The UHV environment suppresses collisions between the trapped ions and the residual background gas, which would otherwise lead to heating, decoherence, or ion loss from the trap. Together, the mechanical vibration isolation and the UHV environment establish a stable experimental platform that is essential for long trapping times and reproducible quantum operations. In many aspects described in this section, the experimental setup is comparable to other ion-trap experiments reported in the literature [19, 82, 88].

Fig. 4.3 illustrates the spatial alignment of all laser fields involved in the experiment, with the exception of the ablation laser. The ablation laser, which operates at a wavelength of 532 nm, is positioned separately from the actual trapping region and is directed onto a solid barium sample. It is employed exclusively during the ion-loading procedure described earlier in Sec. 2.3 and is therefore not co-aligned with the remaining laser beams. The indicated 416 nm and 553 nm beams are used to drive the two-photon photoionization (PI) process. All other laser wavelengths employed in the experiment, together with their specific roles in cooling, state preparation, manipulation, and detection, are described in detail in Sec. 2.4, where the corresponding energy-level diagrams are also provided.

[1] Andor iXon Ultra 897
[2] S-2000 Stabilizer™



(a) (b)

Fig. 4.3: Overview of the laser-beam alignment used in the experiment. (a) Top-view schematic showing the alignment of the radial single-ion addressing TEM_{00} beam together with its counter-propagating TEM_{10} counterpart, both at 532 nm. In addition, the two collectively illuminating beams at 1762 nm, used for coherent ion manipulation, and 416 nm, used for the photoionization (PI) process, are shown. (b) Side-view schematic showing the alignment of the remaining laser fields, each of which illuminates and acts collectively on the full ion chain when active, like for instance the 553 nm beam, which is the second beam used for the two–PI process.

4.2 Optical addressing and imaging

As a first step in constructing the optical system used for addressing and imaging the ions, the expected optical properties were simulated using Zemax software [89]. Fig. 4.4 shows the resulting simulation for the complete addressing system. The simulation begins on the left with a collimated beam entering the beam-expander and ends on the right with the focus created by the Photon Gear microscope objective in the plane of the ions.

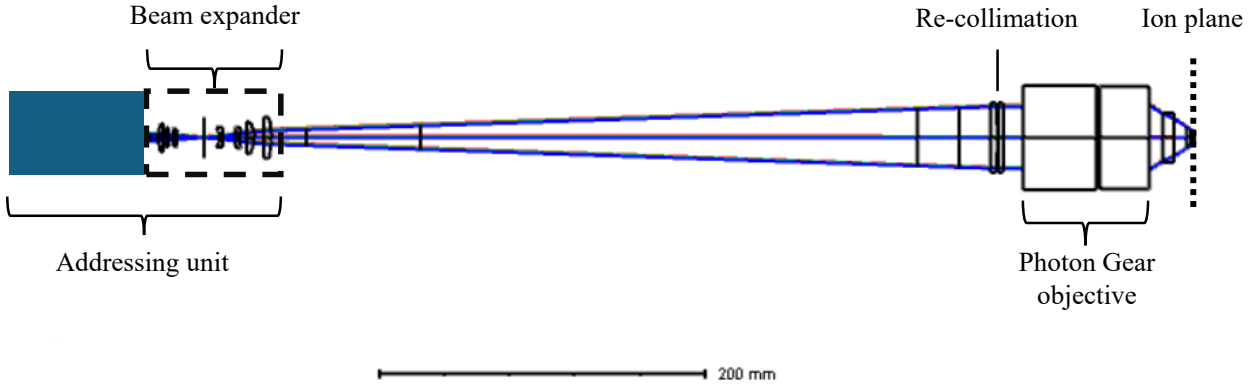


Fig. 4.4: Zemax simulation of the addressing optics. A collimated beam with a diameter of $d = 2$ mm enters the final stage of the addressing unit, the beam-expander objective, which increases the beam divergence to make use of the full numerical aperture (NA) of the Photon Gear objective. A two-lens relay system in front of the Photon Gear objective re-collimates and conditions the beam before it is tightly focused onto the ion plane. Relevant optical components as well as the ion plane position are labeled for clarity.

The most informative outputs of these Zemax simulations were the spot diagrams, which can be evaluated at arbitrary positions along the beam path. Fig. 4.5 shows such a spot diagram of the simulated addressing system, evaluated at the image surface (IMA) in the ion plane. These diagrams provide the calculated spot size using two commonly applied metrics: the root-mean-square (RMS) spot radius, which quantifies the average radial deviation of the traced rays from the reference image point, and the geometric (GEO) spot radius, which corresponds to the maximum distance of any traced ray from that point. These spot diagrams also show how the focus degrades for off-axis field points, parameterized in Zemax by the object-space field angle (OBJ). With increasing OBJ, the spot becomes asymmetric and elongated, revealing off-axis aberrations such as coma and the influence of field curvature. The associated axial shift of the best-focus position is indicated by the IMA values below each subfigure. Thus, the spot diagrams provided both quantitative spot size information and insight into how off-axis aberrations affect the focal quality in the ion plane.

Because the Photon Gear objectives used in the experiment are commercial products, the individual optical components and their geometrical parameters are not accessible to the user. Instead, the vendor provides a so-called "black-box" model that encapsulates the full optical behavior, which can be used directly within Zemax. Although the internal description cannot be inspected or modified, Zemax is still able to perform full ray tracing through the compiled model, enabling the calculation of spot diagrams, aberrations, and field-curvature effects. Ray tracing itself is based on Snell's law:

$$n_1 \sin(\theta_1) = n_2 \sin(\theta_2) \ , \tag{4.2.1}$$

with n_i being the respective refractive index of the optical medium, θ_1 the angle of incidence and θ_2 being the angle of refraction [90].

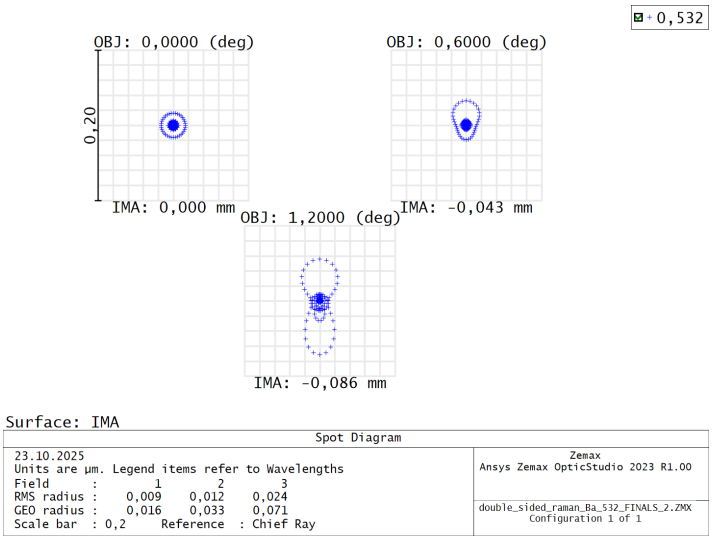


Fig. 4.5: Zemax spot diagram of the 532 nm addressing beam at the image plane (IMA), evaluated for three object-space field angles (OBJ): 0.0°, 0.6°, and 1.2°. The root-mean-square (RMS) spot radii of 0.009 µm, 0.012 µm, and 0.024 µm quantify the average radial deviation of the traced rays from the reference image point. The geometric (GEO) spot radii of 0.016 µm, 0.033 µm, and 0.071 µm correspond to the maximum distance of any traced ray from that point. The grid spacing is 0.2 µm.

The Zemax simulations and the behavior predicted by the simulations provided valuable insight into the design and performance of the overall optical system. For the imaging path as well, shown schematically in Fig. 4.1, a corresponding Zemax model was used to guide the implementation and alignment of the optical components.

The central element of the addressing system is the AOD, which is a form of acousto-optical modulator (AOM) optimized for angular beam steering rather than pure optical frequency shifting. This functionality is achieved by using a crystal cut that differs from standard AOMs, producing distinct acoustic and optical properties due to the crystal's lattice orientation. This specific crystal cut and interaction geometry suppresses the observable consequences of the intrinsic frequency shift, so that the device acts predominantly as a beam deflector rather than a frequency shifter. In addition, the optical phases of the beams emerging from the two AOD devices of the double-sided addressing can be synchronized and precisely adjusted with a suitable RF signal generator. The first pulse of the manipulation sequence defines the phase reference and thereby determines whether the resulting single-qubit rotation on the Bloch sphere is performed around the x or the y axis. All subsequent pulses are defined relative to this initial phase, such that a phase shift of $\pi/2$ switches the rotation axis from x to y. This change of rotational axis follows directly from the rotating-wave approximation (RWA) and is explicitly visible in Eq. 2.5.20.

While the lenses in the addressing system establish the required beam characteristics, the AOD provides the lateral beam displacement needed to select the ion(s) to be addressed. The device is driven by a RF signal that generates an acoustic wave inside the crystal, from which the optical beam diffracts. When multiple RF frequencies are applied simultaneously, the resulting superposition of acoustic waves produces a corresponding superposition of diffracted beam positions. In this way, multiple ions can be addressed simultaneously without requiring additional laser systems. Fig. 4.6 illustrates the AOD and its underlying working principle. The AOD operates in the Bragg regime, where only the ±1st diffraction orders satisfy the Bragg condition:

$$m\lambda = 2\Lambda(\nu_{\mathrm{RF}}) \sin(\theta_{\mathrm{Bragg}}) \qquad \Longrightarrow \qquad \theta_{\mathrm{Bragg}} \approx \frac{m\,\lambda}{2\,\Lambda(\nu_{\mathrm{RF}})} = \frac{m\,\lambda\,\nu_{\mathrm{RF}}}{2\,v_{\mathrm{ac}}} \ , \tag{4.2.2}$$

where $\Lambda(\nu_{\mathrm{RF}}) = v_{\mathrm{ac}}/\nu_{\mathrm{RF}}$ is the acoustic wavelength with velocity v_{ac} generated in the crystal by the applied RF frequency ν_{RF}, λ is the optical wavelength, m denotes the diffraction order, and θ_{Bragg} is the internal Bragg angle.

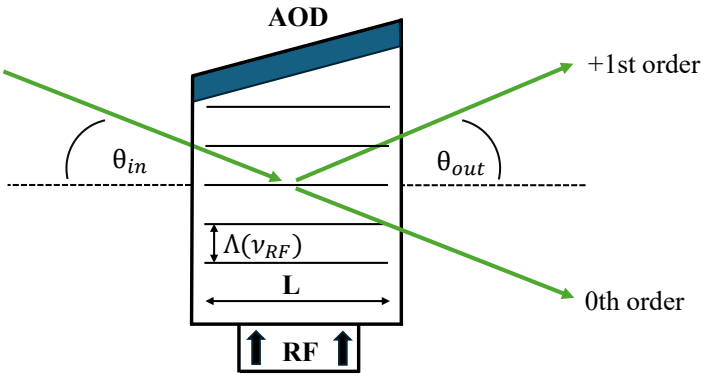


Fig. 4.6: Schematic of the AOD showing the 0th and +1st diffracted orders. The incident angle is denoted by θ_{in}, while the deflection angle of the diffracted beam is labeled θ_{out}. The length of the optical–acoustic interaction region inside the crystal is indicated by L. RF marks the applied radio-frequency drive, and $\Lambda(\nu_{\mathrm{RF}})$ denotes the acoustic wavelength generated in the crystal as a function of the RF frequency ν_{RF}, which sets the Bragg condition and thereby the resulting deflection angle. The blue bar indicates an acoustic absorber used to suppress back reflections of the sound wave, typically mounted at a slight angle to minimize residual back-propagating waves.

In contrast to conventional Bragg diffraction from a stationary lattice, the light in an AOD diffracts from a traveling sound wave. Momentum conservation with the traveling acoustic grating changes the beam's propagation direction, producing an angular deflection that scales approximately as [30]:

$$\Delta\theta_{\mathrm{out}} = \arctan\left(\frac{k_{\mathrm{ac}}}{k}\right) \approx \frac{k_{\mathrm{ac}}}{k} = \frac{\lambda}{\Lambda(\nu_{\mathrm{RF}})} \,, \tag{4.2.3}$$

with k_{ac} being the wave-vector magnitude of the acoustic wave traveling inside the crystal and k that of the optical input beam. Varying the RF frequency ν_{RF} changes the acoustic wavelength and thus the Bragg condition, enabling rapid tuning of the output angle. The internal Bragg angle itself varies linearly with the RF frequency as Eq. 4.2.2 shows. If the incidence angle is fixed, as it is the case within our experiment, large frequency excursions eventually lead to a mismatch between the incidence angle and the Bragg angle, reducing the diffraction efficiency. This effect defines the angular acceptance bandwidth of the AOD. The achievable rate of deflection variation is limited by several temporal factors: the electrical rise time of the RF signal, the time required for the acoustic wave to build up inside the crystal, and the access time, i.e., the time needed for the acoustic wave to traverse the optical beam. Given the acoustic velocity in quartz ($5\,\mathrm{km\,s^{-1}}$ to $6\,\mathrm{km\,s^{-1}}$), deflection rates up to several MHz are feasible. The same principles apply to negative diffraction orders, except that they require the opposite incidence angle.

When the incidence angle is precisely matched to the Bragg angle, the diffraction efficiency and bandwidth are maximized, and the resulting spectral bandshape reduces to a pure sinc- or Bessel-type function, depending on the effective aperture of the AOD[3] [91]. If the incidence angle is geometrically detuned from the ideal Bragg condition, the diffraction efficiency can be obtained using more elaborate methods. These approaches can involve a momentum-space (k-space) construction to evaluate the phase-matching condition geometrically, rather than solving the coupled differential wave equations directly. Small angular detunings introduce a modified bandshape consisting of the usual sinc/Bessel envelope accompanied by characteristic side lobes ("ripples") around the central frequency. For first-order Bragg diffraction, the efficiency can be described by the coupled-wave solution of Kogelnik [92]:

$$\eta(s,\zeta) = \frac{s^2}{s^2+\zeta^2} \cdot \sin^2\left(\sqrt{s^2+\zeta^2}\right) \,, \tag{4.2.4}$$

where η denotes the diffraction efficiency, s represents the coupling strength determined by the acoustic wave inside the crystal and is proportional to the square root of the applied RF power, $s \propto \sqrt{P_{\mathrm{RF}}}$, and $\zeta \coloneqq \frac{1}{2}\Delta k_z L$

[3] Acousto-optic deflector of type DTSX-400-532-M023, designed for operation at 532 nm.

is the dimensionless longitudinal phase mismatch between the interacting waves. Here, Δk_z denotes the difference of the relevant optical and acoustic wave-vector components along the propagation direction z and thus incorporates deviations from exact Bragg matching, in particular angular detuning of the incident beam. The interaction length is given by L and is equivalent to the width of the optical crystal. The contrast between the bandshape under ideal Bragg matching and the band profile arising from angular detuning is illustrated in Fig. 6.2(b) and Fig. 6.3(b) in Sec. 6.2. Furthermore, it should be noted that the scalar description used here does not treat polarization effects explicitly. These effects enter through the effective acousto-optic coupling coefficient, which depends on the photo-elastic tensor of the crystal and on the input and output polarization vectors. In general, this coupling can be written schematically as:

$$\kappa \propto \mathbf{e}_{\text{out}}^{*} \cdot \Delta\boldsymbol{\varepsilon} \cdot \mathbf{e}_{\text{in}} \ , \tag{4.2.5}$$

where $\Delta\boldsymbol{\varepsilon}$ denotes the acoustically induced permittivity modulation [30]. A full vectorial treatment is therefore required to describe possible polarization changes caused by the AOD. In the scalar model used in Eqs. 4.2.2–4.2.4, such polarization-dependent effects are absorbed into the effective coupling strength s and are not described explicitly.

4.3 Light distribution and addressing control

In this section, the breadboard responsible for controlling the operational actions of the addressing units is introduced. A schematic of this breadboard is shown in Fig. 4.7.

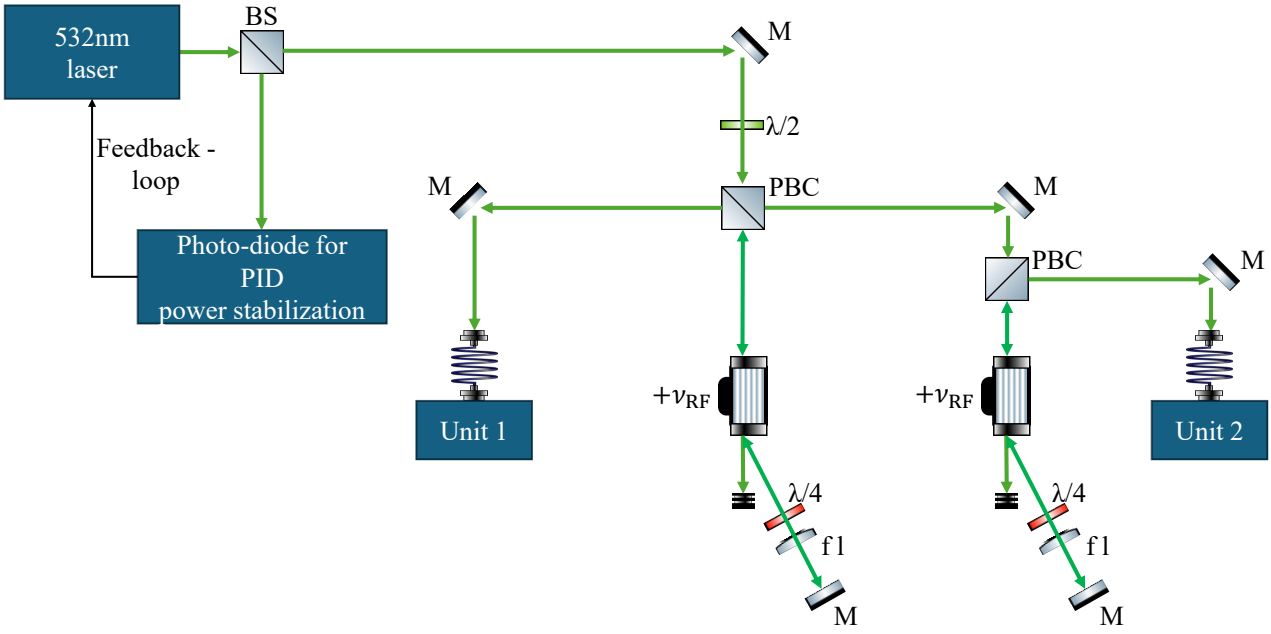


Fig. 4.7: Schematic of the control breadboard. Abbreviations: M – mirror; BS – non-polarizing beam splitter with fixed splitting ratio; PBS – polarizing beam splitter cube; $\lambda/2$ – half-wave plate; ν_{RF} – RF drive frequency of the AOMs; f l – focusing lens. A 532 nm laser serves as the input source to the breadboard. A small fraction of the power (about 1 %) is directed onto a photodiode for active power stabilization via a feedback loop. The remaining power is evenly split into two AOM double-pass paths in cat-eye configuration, using half-wave plates and PBS cubes, each providing the controlled input beam for one addressing unit.

A 532 nm laser system[4] provides the light source for the control breadboard. A small fraction of the optical input power (approximately 1 %) is directed onto a photodiode, which serves as the detector for a power-stabilization branch. The photodiode produces a voltage proportional to the incident optical power, providing the error signal for the power-stabilization feedback loop that is returned to the laser power control input. This signal is then processed by a proportional–integral–derivative (PID) controller, which adjusts the laser output power to maintain a constant intensity [93]. The remaining optical power is divided evenly between two AOM double-pass setups, each providing a total frequency shift of $2\nu_{\text{RF}}$. The combination of $\lambda/2$ phase-retarding wave plates and polarizing beam-splitter cubes (PBCs) allows us to distribute the laser power

[4] Coherent – Verdi V5

between the different arms according to the experimental requirements. A theoretical framework for this kind of power-distribution scheme based upon light polarization and PBCs is provided in Sec. 2.2.

The double passes are implemented in a cat-eye configuration: the first positive AOM-diffracted orders are focused onto retroreflecting mirrors such that, upon reflection, they retrace (almost exactly) the incoming paths through the AOM during the first pass [94]. The zeroth orders are directed into a beam dump. A pair of $\lambda/4$ phase-retarding wave plates placed in front of the retroreflectors rotates the polarization of the returning, double-passed beams by 90° relative to the input, ensuring that the PBCs preceding the double passes reflect the beams rather than transmitting them. Finally, the double-passed light is coupled into optical fibers, which provide the inputs for the addressing units. If the two double-pass AOMs are not operated exactly at the same radio frequency $+\nu_{\mathrm{RF}}$ but are slightly detuned with respect to each other, the superposition of the TEM_{00} and TEM_{10} modes acquires a time-dependent relative phase, $\Delta\phi(t) = \Delta\omega\, t = \Delta\nu\, 2\pi\, t$, resulting in a temporal beating of the combined mode.

Chapter 5

Layout of addressing units and incorporation of phase plate

For the physical realization of quantum gate operations in trapped-ion experiments, one requires the capability to manipulate individual ions with high precision. This task, known as single-ion addressing, is achieved by introducing a tightly focused laser beam, the addressing beam. The pointing and steering of such addressing beams are performed by the addressing units.

The addressing units used in the experiment are compact optical devices capable of steering the beam direction and controlling additional beam properties such as polarization, spot size, focal depth, and divergence, in conjunction with the remaining optical elements of the experiment. In our setup, two such units illuminate the ions from opposite sides along the propagation of the horizontal radial direction of the trap.

The addressing unit design used in the experiment builds upon an established system that has been successfully used in other trapped-ion experiments, such as the LinTrap setup [88]. The following sections describe the design and operating principles of the addressing units employed in the experiment, as well as the function of their individual components.

5.1 Addressing unit layout

Fig. 5.1 shows a two-dimensional top-view schematic of the addressing-unit layout. The light path of the off-resonant 532 nm addressing beam begins in the upper left corner with a fiber-coupled input collimator[1]. The polarization of the input light is aligned with the principal axis of the fiber-coupled collimator using a polarimeter[2] to prevent intensity noise arising from polarization fluctuations introduced by the fiber.

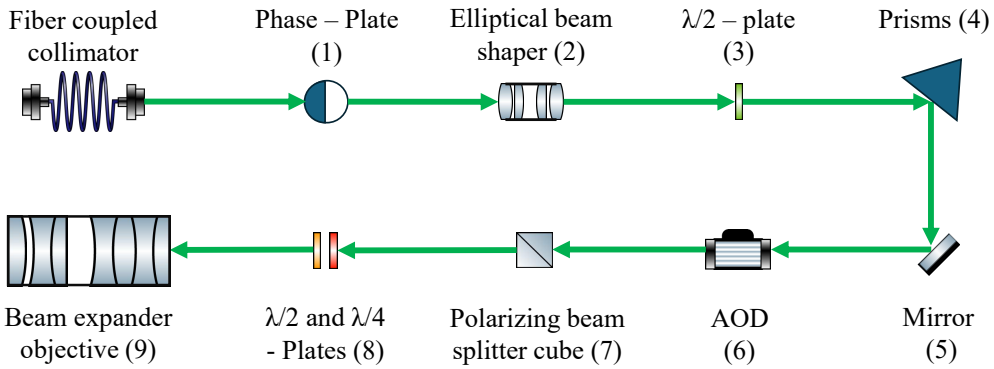


Fig. 5.1: 2D-schematic of addressing unit layout. The input for the addressing is provided by a fiber-coupled collimator (on the top left in the schematic). All subsequent optical elements are numbered and explained in the main text in a detailed list with corresponding item number.

[1] Schäfter & Kirchhoff: 60FC-M-12 with a special coating optimized for the addressing wavelength of 532 nm
[2] Schäfter & Kirchhoff — SK010PA, 450–800,nm

1. The first optical element after the input collimator is the phase plate, which is used to generate a TEM_{10} mode from the incoming fundamental TEM_{00} mode. This phase plate is the only optical element that is not present in both addressing units and is included exclusively in the unit providing the TEM_{10} addressing beam. The integration of this phase plate, as well as its theoretical working principle, are described in detail in Sec. 5.2.

2. The next optical element is the elliptical beam shaper, which modifies the beam waist only along the axial trap direction while leaving the vertical radial direction unchanged, thereby producing an elliptical beam profile. This component prevents illumination and charging of the compensation electrodes and avoids clipping of the addressing beam, while allowing use of the full NA along the axial trap dimension. According to Eq. 2.2.9, increasing the beam waist before a focusing optic reduces the focus spot size, making axial beam shaping sufficient for addressing a linear ion chain.

3. The subsequent $\lambda/2$ phase plate sets the correct polarization for the AOD. Because several reflective optical elements lie between this phase plate and the AOD, the light path is first aligned up to the intended AOD position. Instead of installing the AOD at this stage, a polarimeter is placed at its location to measure and adjust the polarization of the beam accordingly.

4. The next elements in the beam path are two fixed 45° prisms mounted on translation stages, which deflect the beam upward toward downstream optical components. In contrast to adjustable mirror mounts, these prisms provide a mechanically stable and well-defined beam deflection while allowing lateral beam position adjustments through the translation stages. They provide the degrees of freedom required to align the addressing beam through the apertures of downstream optical elements, such as the AOD device or the final beam-expander objective, without introducing additional angular alignment parameters at this stage.

5. The following mirror, together with the adjustable orientation of the AOD device, determines the angle of incidence onto the AOD. This interplay between mirror orientation and AOD alignment influences both the diffraction efficiency and the available bandwidth of the AOD. If the beam propagation is tilted at this stage, the mirror mount allows for correcting the alignment before the beam enters the AOD.

6. The AOD device follows next in the beam path. It is mounted on a specially designed base plate that can rotate over a limited angular range (approximately 30°). This rotating plate is itself mounted on a goniometer, which provides rotation around the beam propagation axis and allows compensation for small relative tilts between the addressing path and the ion chain inside the trap. For theoretical background on AOD operation, the reader is referred to Sec. 4.2 of this thesis and Ref. 91, 92. Details of the AOD characterization are presented in Sec. 6.2.

7. A Glan–Taylor polarizing beam-splitting prism is next in the beam propagation path. This element serves two purposes within the addressing system. First, it re-cleans the polarization of the addressing beam. Second, it suppresses the undesired diffraction orders produced by the AOD. In the Bragg regime and for the chosen alignment, the AOD primarily generates the desired −1st diffraction order together with a residual 0th order, while all higher diffraction-order intensities are negligible (below the 1 % level). Due to the compact design of the addressing units, spatially blocking the undesired 0th order (e.g. with a razor blade) is not feasible, as the separation between the orders in the remaining propagation distance is insufficient. Although simulations performed at AQT indicate that the 0th order is sufficiently displaced from the ion chain at the trapping region (100 µm to 150 µm), it is nevertheless good experimental practice to minimize unnecessary stray light. This prism exploits the polarization dependence of the diffracted beams: the −1st order receives a polarization rotation, whereas the 0th order remains unchanged, allowing efficient separation based on polarization. The measured extinction ratio of the prism is $R_{\text{ext}} = 4.37(6)\,\%$.

8. Next follows a combination of $\lambda/4$ and $\lambda/2$ phase-retarding wave plates, both mounted in rotational mounts. Together, these wave plates allow precise control of the polarization of the addressing beam at the ion position and enable independent polarization settings for each addressing unit. In this way, the system can be operated either with intensity gradients (identical linear polarizations) or with polarization gradients (different linear polarizations).

9. Finally, the addressing beam enters the beam-expander objective, which is realized in an afocal relay configuration enabling largely independent control of spot size and angular mapping [95]. This element introduces a controlled beam divergence to match the entrance field diameter of the Photon Gear microscope objective and thereby efficiently utilize the NA of the optical system. The focal depth can be fine-adjusted by varying the spacing between the two lens groups of the beam-expander objective. In addition, the objective allows tuning of the effective angular magnification, which determines the displacement of the addressing beam per MHz of AOD input frequency. Identical displacement of the two superimposed addressing beams is ensured by matching this angular magnification between both addressing units via fine adjustment of the position of the final lens element (the tip) relative to the remaining lenses. Both adjustment degrees of freedom are indicated in Fig. 5.1 (item 9) by the gaps between the individual lenses.

5.2 TEM_{10} mode creation and phase plate incorporation

A major adaptation to the addressing-unit design was the incorporation of the phase plate, which is used to generate a TEM_{10} Hermite–Gauss mode for the double-sided addressing system. This section is divided into two parts. First, the physical working principle by which the phase plate converts an incoming fundamental TEM_{00} mode into the desired higher-order mode is discussed. Second, the mechanical integration of the phase plate into one of the two addressing units is described. This integration is realized by means of a specially designed mount adapter, which was partially fabricated in-house.

5.2.1 Physical working principle of the phase plate for TEM_{10} mode generation

The creation of a TEM_{10} mode using a phase plate can be understood within the framework of Fourier optics [30, 96, 97]. A central concept of Fourier optics is the description of image formation in a linear, shift-invariant optical system via spatial convolution:

$$\underbrace{g(x,y)}_{\text{image}} = \underbrace{f(x,y)}_{\text{object}} * \underbrace{h(x,y)}_{\text{PSF}} , \tag{5.2.1}$$

where $f(x,y)$ denotes the object field, $h(x,y)$ the point spread function (PSF), which describes the system's response to a point-like light source, and $g(x,y)$ the resulting image field. The convolution operation, denoted by the symbol $*$, is defined in one dimension as:

$$(f * g)(x) = \int_{-\infty}^{\infty} f(x-\tilde{x})\, g(\tilde{x})\, d\tilde{x} \ . \tag{5.2.2}$$

In Fourier optics, the Fourier transform is taken with respect to spatial coordinates. For a one-dimensional transverse coordinate x, it is defined as:

$$F(k_x) = \mathcal{F}\{f(x)\} = \int_{-\infty}^{\infty} f(x)\, e^{-ik_x x}\, dx \ , \tag{5.2.3}$$

with k_x being the spatial frequency of dimension x. Applying the Fourier transform to the imaging equation yields:

$$\begin{aligned} g(x,y) &= \mathcal{F}^{-1}\left[\mathcal{F}\{f(x,y)\} \cdot \mathcal{F}\{h(x,y)\}\right] \\ &= \mathcal{F}^{-1}[F(k_x,k_y) \cdot \underbrace{H(x,y)}_{\text{OTF}}] \ , \end{aligned} \tag{5.2.4}$$

where $H(x,y)$ is the optical transfer function (OTF), which is defined as the Fourier transform of the PSF. The OTF characterizes how spatial frequencies of the object are transmitted by the optical system to the image. Equation 5.2.4 follows from the convolution theorem, which states that convolution in the spatial domain corresponds to multiplication in the spatial-frequency domain.

Within this Fourier-optics framework, numerical simulations were performed to model the action of the phase plate. In these simulations, the phase plate was approximated as a step function imposing a relative phase shift of π between the two halves of an incident fundamental TEM_{00} beam. Although the phase step can be idealized as infinitely sharp, the resulting discontinuity in the phase profile inevitably introduces high spatial-frequency components. Upon propagation through the phase plate, these components give rise to diffraction-induced side-lobes extending beyond the central TEM_{10} intensity distribution.

These diffraction side-lobes constitute an undesired contribution to the addressing beam profile of an ideal TEM_{10} mode, as they can increase crosstalk to neighboring ions. Two mitigation strategies were identified: either the implementation of an additional spatial-filtering stage, such as a cleaning telescope with a pinhole placed in its Fourier plane, i.e. the focal plane of the cleaning telescope, or a rotation of the TEM_{10} mode with the side-lobes still present, such that the side-lobes are oriented away from the ion chain. In the present experiment, the latter approach was chosen, and the TEM_{10} addressing beam was rotated by approximately 15°, selected empirically as a compromise between side-lobe suppression and usable force gradient. This rotation reduces addressing errors without introducing additional optical complexity.

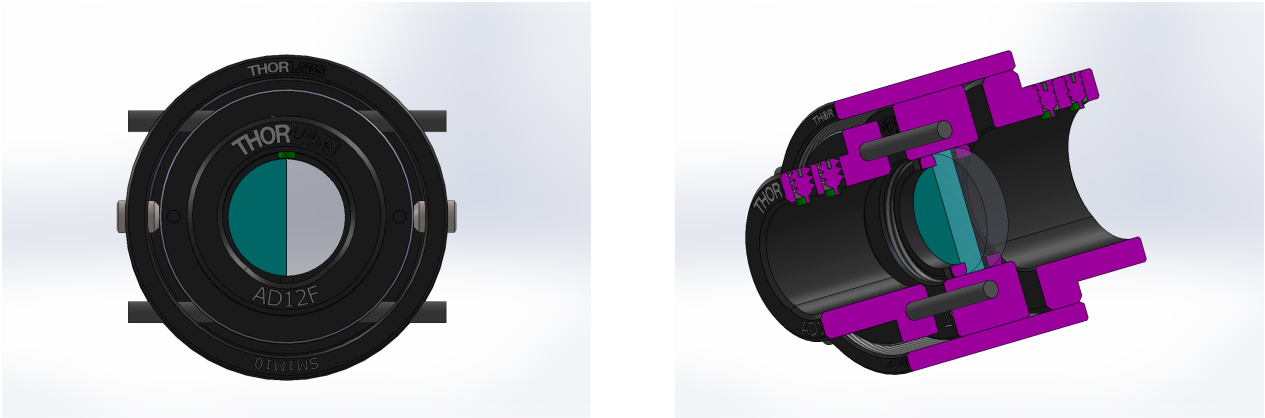
5.2.2 Mount adapter

For symmetry reasons, it is imperative to align the fundamental TEM_{00} beam centrally with respect to the phase plate. Any lateral misalignment breaks the intended spatial symmetry of the generated TEM_{10} mode and thereby distorts the resulting optical force profile acting on the ion. Since the coupling to motional degrees of freedom is determined by the spatial gradient of the light field, preserving the symmetry of the addressing beam is essential to ensure controlled and selective excitation of the desired motional modes while suppressing unwanted couplings. In the harmonic axial trapping potential, this symmetry directly maps onto the coupling strengths between the optical dipole force and the motional eigenmodes of the ion.

In the ideal situation, one would aim for a stable alignment precision of the complete optical system at a level of a single µm, in order to guarantee a high degree of symmetry and, consequently, well-defined parity. However, the thermal expansion coefficients of standard metals lead to spatial changes on the order of several tens of micrometers (10 µm to 30 µm), rendering such alignment precision difficult to realize in practice. Achieving this level of stability would require the use of expensive high-end materials throughout the entire experiment and all involved opto-mechanical components.

To address this challenge and enable stable, highly central alignment of the addressing beam, a suitable mount adapter was developed. In collaboration with the university's mechanical workshop, standard commercial opto-mechanical components were adapted to introduce additional degrees of freedom. These adaptations allow high-precision alignment of the addressing beam with respect to the center of the phase plate, within the expected deviations caused by the thermal expansion of aluminum.

In this mount-adapter design, the thread of the input collimator mount is removed and replaced by two guiding pins that act as linear rails. The collimator mounted within this structure can therefore be translated in a controlled manner, similar to a translation stage. Once aligned, the position is fixed rigidly using two additional set screws. A SolidWorks blueprint of the developed mount adapter is shown in Fig. 5.2.



(a) (b)

Fig. 5.2: SolidWorks blueprint views of the partially self-manufactured mount adapter used for precise phase plate alignment. (a) Front blueprint view of the partially self-manufactured mounting adapter. The input collimator is omitted in the rendering to make the central alignment line of the integrated phase plate clearly visible. (b) Angled sectional view of the mounting adapter.

Chapter 6

Characterization and implementation of addressing units

The following sections present the opto-mechanical characterization of both addressing units and their individual components. For the investigation of single components and their specific properties, test setups external to the addressing units were frequently employed. These free-standing test setups provided improved accessibility and additional degrees of freedom for alignment and diagnostics.

For certain properties of interest, such as the collimation quality of the laser beam within the addressing units, it was otherwise not possible to acquire a sufficient number of data points within the compact geometry of the units themselves. Unless stated otherwise, the quoted uncertainties throughout this chapter correspond to statistical errors derived from the respective measurements or measurement series and do not include systematic contributions, such that the total uncertainty is likely underestimated.

The final section of this chapter, Sec. 6.7, focuses on the implementation, alignment, and quantum mechanical performance optimization of the addressing units in the experiment, utilizing the confined ions in a quantum metrology sense. This chapter, and in particular its final section, therefore constitutes the main experimental results of this thesis.

6.1 Collimation quality of addressing unit input

The goal of this section was to verify that the input light field of the addressing units matches the beam parameters assumed in the optical simulations used for the design of the experiment. To this end, several candidate fiber-coupled input collimators were characterized. In the following, only the results for the collimator ultimately selected for operation are presented.

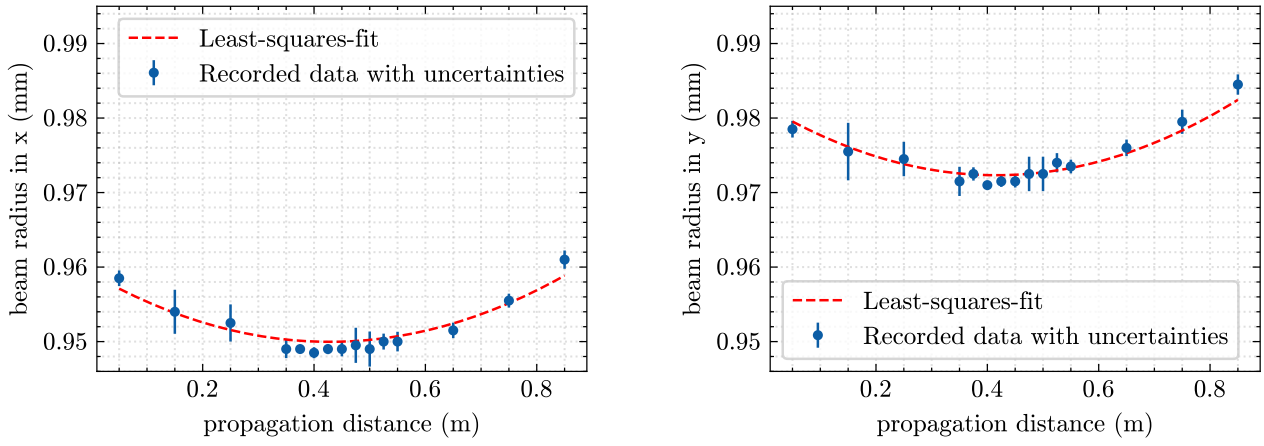
For the measurements, beam-radius data and associated uncertainties were obtained using a beam profiler[1]. Each data point along the propagation direction was recorded with a detection time of one minute. The observed variation in the uncertainties is mainly attributed to the laser delivery path, whose optical power was not actively stabilized during the measurements.

Fig. 6.1 shows the measured beam radii at the input of the first addressing unit for both spatial dimensions transverse to the propagation direction z, namely x and y, together with least-squares fits based on the Gaussian beam propagation model:

$$w(z,\, z_0,\, w_0,\, z_R) = w_0 \sqrt{1 + \left(\frac{z - z_0}{z_R} \right)^2} \,,$$

which follows from Eq. 2.2.4 with the inclusion of an additional longitudinal offset z_0. For the transverse x direction, the fit yields a Rayleigh length of $z_{R,x} = 3.1(2)\,\mathrm{m}$, a waist position of $z_{0,x} = 43(2)\,\mathrm{cm}$, and a minimum waist of $w_{0,x} = 950.0(4)\,\mu\mathrm{m}$, implying a difference to the Zemax simulation of 5 %. For the transverse y direction, the fit reveals a Rayleigh length of $z_{R,y} = 3.0(1)\,\mathrm{m}$, a waist position of $z_{0,y} = 42(1)\,\mathrm{cm}$, and a minimum waist of $w_{0,y} = 972.3(3)\,\mu\mathrm{m}$, corresponding to a difference to the theoretically assumed value in the simulations of approximately 3 %.

[1] Ophir Photonics Ltd., Spiricon SP620U beam profiling camera



(a) (b)

Fig. 6.1: Gaussian beam waist as a function of propagation distance for the input beam of the first addressing unit. Least-squares fits based on Eq. 2.2.4 are shown for both transverse directions. (a) Transverse x direction, yielding a spatial offset of $z_{0,x} = 43(2)\,\mathrm{cm}$, a minimum waist of $w_0 = 950.0(4)\,\mu\mathrm{m}$, and a Rayleigh length of $z_{R,x} = 3.1(2)\,\mathrm{m}$. (b) Transverse y direction, yielding $z_{0,y} = 42(1)\,\mathrm{cm}$, $w_{0,y} = 972.3(3)\,\mu\mathrm{m}$, and $z_{R,y} = 3.0(1)\,\mathrm{m}$.

The slight differences between the fitted parameters in the two transverse directions indicate weak astigmatism of the input beam, which is commonly observed in practical free-space beam delivery systems and can arise from residual alignment imperfections or optical aberrations. The extracted values agree within uncertainties and exhibit comparable propagation behavior on both transverse axes. The measured waist sizes in both spatial dimensions are closest to the value used in the Zemax simulations ($w_0 = 1\,\mathrm{mm}$) among all tested input collimators, deviating by approximately 4 % when averaged. This level of agreement between theoretical simulation and experimental observation was used as the basis for the addressing optics input and the subsequent experimental implementation.

The second input collimator for the opposing addressing unit was ordered at a later stage, after experimental validation of several candidates, and was therefore not available during the quantitative measurements presented here. Although preliminary attempts were made to characterize the collimation quality of the second input collimator, the limited available space did not permit a comparable measurement. In agreement with the experimental team, a qualitative assessment was therefore considered sufficient. Given the use of the same fiber type and an identical collimator model, no physical mechanism is expected to prevent comparable beam waist and Rayleigh length values from being achieved. The qualitative inspection of the second input collimator was consistent with the results obtained for the first input collimator.

6.2 Efficiency and bandwidth of both AOD devices

As a next step, both AOD devices were analyzed, as they constitute a key optical element of the addressing units. The AOD enables controlled steering of the laser beam by varying the applied RF signal. As described in more detail in Sec. 4.2, changes in the RF frequency lead to different angular deflections of the diffracted beam. The quantification of the deflection performance included several complementary aspects. In particular, the optical diffraction efficiency and the accessible bandwidth of the employed -1st diffraction order of both AOD devices were studied. The investigation and results of these two aspects are presented in this section, while the analysis of optical aberrations is treated separately in Sec. 6.4.

Fig. 6.2 shows the results obtained for the first AOD device. Each data point and its associated uncertainty were measured using a power meter[2], with a total of 50 measurement samples per data point. On the left, in Fig. 6.2(a), the transmitted optical power of the -1st diffracted order is plotted as a function of the RF power applied to the AOD. For this measurement, the RF frequency was kept constant at a central value of $\nu_0 = 80\,\mathrm{MHz}$. With an initial optical power before the AOD of $975(5)\,\mu\mathrm{W}$, the optical diffraction efficiency shown here was obtained by normalizing the transmitted power to this input value. The absolute RF power corresponding to the x-axis was determined using a handheld RF spectrum analyzer, where a setting of $-4.4\,\mathrm{dBm}$ corresponded to approximately 1 W of RF output power for the specific RF amplifier[3] and RF signal

[2]Thorlabs, model 100D power meter
[3]Mini-Circuits ZHL-SW-1$^+$ RF amplifiers

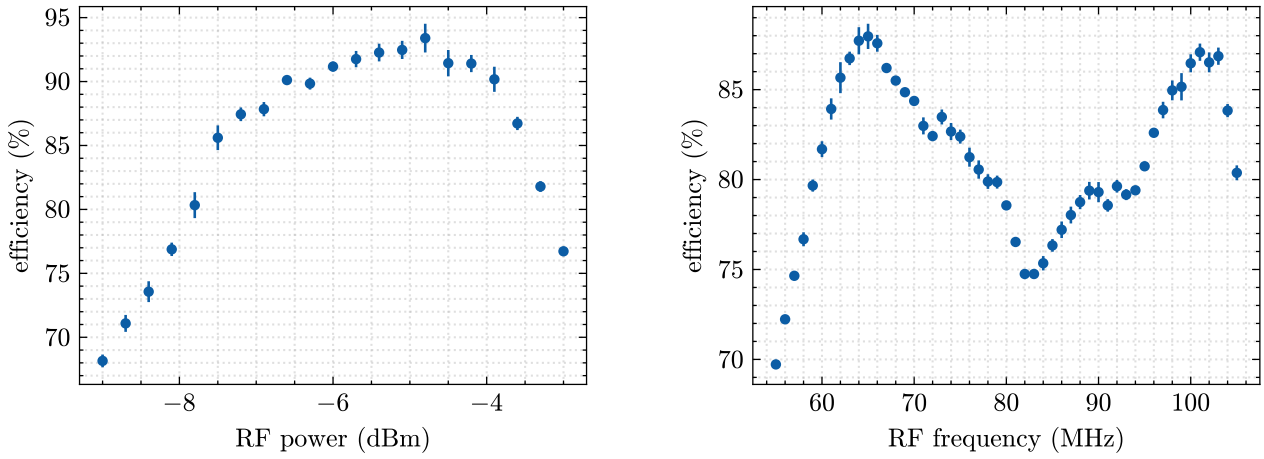


Fig. 6.2: Measurement results for the first AOD device. (a) Optical power efficiency of the −1st diffraction order as a function of the RF power applied to the AOD crystal. (b) Optical power efficiency of the −1st diffraction order as a function of the RF frequency applied to the AOD crystal.

generator[4] configuration used. The recorded data points exceed the specifications given in the manufacturer datasheet, which lists an efficiency of $> 78\,\%$ for the −1st diffraction order. The maximum efficiency observed in the present measurement series amounts to $93(1)\,\%$.

The next property investigated for the first AOD device was its total bandwidth. In addition to the material properties of the acousto-optical crystal, the bandwidth is mainly determined by the angle of incidence at the crystal surface. This angle governs the shape of the diffraction efficiency curve and therefore directly determines the accessible bandwidth [91]. In Fig. 6.2(b), the transmitted optical power of the −1st diffraction order is plotted as a function of the applied RF frequency across the full nominal bandwidth of 50 MHz, centered around $\nu_0 = 82(4)\,\mathrm{MHz}$, as specified by the manufacturer. The overall shape of the measured bandwidth profile is consistent with the provided test datasheet. However, distortions and asymmetries are visible, which are attributed to optical power fluctuations during the measurement. Since the acquisition of the full bandwidth measurement required a certain time, with each data point obtained from 50 individual samples, the system had sufficient time to undergo slow drifts between successive measurement points. In particular, the optical power of the beam was not actively stabilized during these measurements. Nevertheless, the qualitative behavior of the AOD bandwidth is clearly demonstrated. Additional, unrecorded measurements employing continuous sweeps of the RF frequency further confirmed that a smooth and symmetric bandwidth profile can be achieved under more stable conditions.

The quantitative determination of the bandwidth was based on the full width at half maximum (FWHM) criterion. Within the tested frequency range of 50 MHz, none of the recorded diffraction efficiencies dropped below half of the maximum peak value for the chosen settings of the first AOD device. This result implies an effective bandwidth that is at least as large as, and potentially larger than, the value specified in the provided test datasheet of 50 MHz. Overall, the advertised performance characteristics of the AOD device were verified and confirmed.

For the second AOD device, the same characterizations of optical diffraction efficiency and total diffraction bandwidth were performed. Fig. 6.3 shows the measurement results for the optical diffraction efficiency as a function of RF power (Fig. 6.3(a)) as well as for the total diffraction bandwidth (Fig. 6.3(b)). The optical diffraction efficiency of the second AOD device exhibits qualitatively the same dependence on RF power as observed for the first device, while the absolute efficiency values and the shape of the curve differ slightly. This deviation becomes apparent when directly comparing Fig. 6.2(a) and Fig. 6.3(a). It is mainly attributed to small variations in the RF signal chain, including the amplifier, signal generator, and RF cabling. Even when identical device models are used, individual components in respective devices and cable lengths can introduce minor differences in the effective RF power delivered to the AOD. In addition, the power fluctuations contribute to the differences. Within the bandwidth measurement of the second AOD device, the influence of the chosen angle of incidence was investigated. A higher diffraction efficiency at the central frequency results in a bandwidth profile that approaches a single-peaked shape, reflecting the absence of additional angular detuning. This behavior is explained in more detail in Sec. 4.2 and Ref. [91]. When operated with the same angular

[4] Rigol Technologies DSG815 RF signal generator

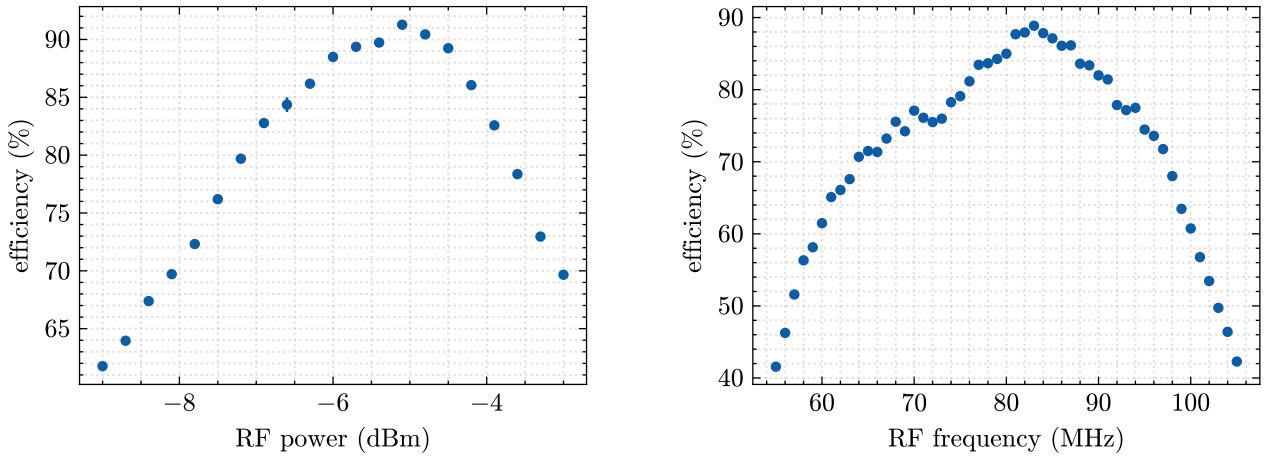


Fig. 6.3: Measurement series for the second AOD device. (a): Measurement of optical power efficiency of the −1st diffracted order as a function of the RF power applied to the AOD crystal. (b): Measurement of optical power efficiency of the −1st diffracted order as a function of the RF frequency applied to the AOD crystal (with no angular detuning in place to visualize bandwidth-shape change).

detuning, the diffraction efficiency profile of the second AOD device over the measured frequency interval qualitatively matches that of the first device. A direct comparison of the measurement uncertainties in Fig. 6.2 and Fig. 6.3 shows improved stability during the characterization of the second AOD device. Quantitatively, the maximum relative uncertainty for the first device amounts to ±1.12 %, whereas for the second device the maximum uncertainty is reduced to ±0.64 %. This corresponds to a reduction of the maximum noise level to approximately 57 % of the original value for the second AOD device.

For implementation in the experiment, neither of the bandwidth settings shown above was chosen. Instead, an intermediate operating point was selected in the transition region of the bandwidth profile. This choice provides a relatively high optical diffraction efficiency of approximately 85 % at the central frequency while yielding flatter slopes around the maximum of the efficiency curve. Flatter slopes correspond to a reduced sensitivity of the optical diffraction efficiency to variations in the applied RF frequency. In the experiment, optical diffraction efficiency and bandwidth profile are used in an interdependent trade-off. Frequency dependent variations in diffraction efficiency can be compensated by adjusting the RF power. For this reason, both AOD devices are chosen to operate in a linear regime of the efficiency curve, below saturation, where such compensation remains feasible. The reduced slope of the selected bandwidth profile further minimizes the required compensation, thereby improving operational robustness. Fig. 6.4 shows the chosen bandshape, analytically simulated using coupled-wave theory of Kogelnik as introduced in Sec. 4.2.

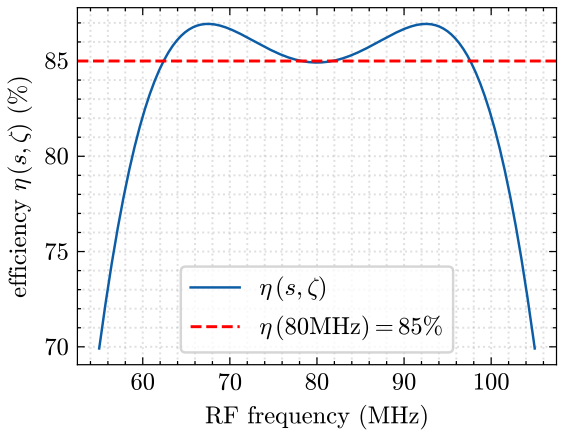


Fig. 6.4: Simulated optical diffraction efficiency profile for the chosen bandwidth setting according to Eq. 4.2.4, with $s \approx 509$ and an angular detuning of $\Delta\theta \approx 31\,\mu\text{rad}$. The detuning parameter ζ is varied via a linearized mapping of the RF-frequency detuning, resulting in an optical diffraction efficiency of 84.9 % at the central AOD RF frequency of 80 MHz. The red dashed line indicates the target diffraction efficiency of 85 % used for the experimental alignment of the AOD device at the central RF frequency.

6.3 Fundamental addressing properties in the ion plane

The purpose of the test setup used in this section was to observe and quantify fundamental properties of the addressing beams under realistic experimental conditions, without requiring direct implementation on the actual experiment. These properties include the achievable spot size, the accessible deflection range in the ion plane, and the magnitude of Airy-fringe-induced crosstalk. Fig. 6.5 shows a schematic overview of the test setup and its main components.

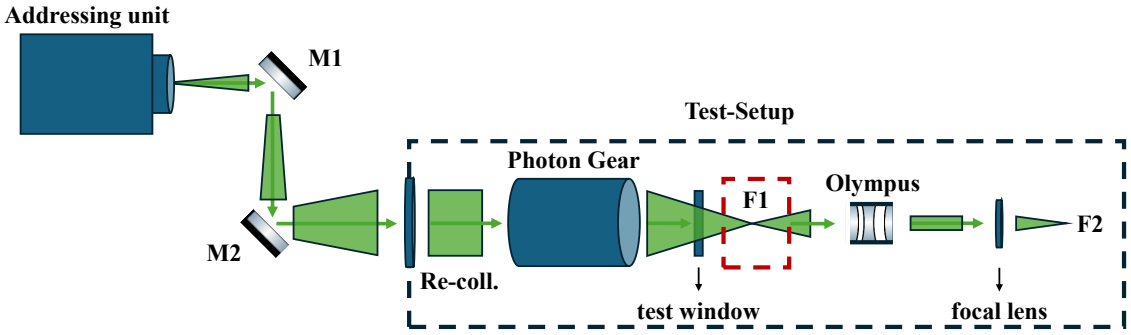


Fig. 6.5: Schematic overview of the test setup illustrating the indirect spot-size measurement principle using a Keplerian telescope. The addressing unit under characterization provides the light, which is reflected by two mirrors (M) before being re-collimated and subsequently illuminating the Photon Gear microscope objective. After transmission through the test window, the Photon Gear objective produces a tightly focused beam at the ion plane (F1). The beam is subsequently re-collimated by an Olympus objective, and a final focusing lens generates a second focus (F2). The two focal planes F1 and F2 are related via the combined magnification of the Olympus objective and the final focusing lens, forming an effective Keplerian telescope.

This test setup was equipped with the same mount for the Photon Gear objective as used in the experiment. In addition, it contained a test window positioned at the correct relative distance with respect to the Photon Gear objective. The test window closely matched the one used in the experiment. The window deviated in thickness (by approximately 50 µm) and lacked the dedicated anti-reflection coating for the 532 nm addressing wavelength due to time and cost constraints.

As a final optical component, the test setup featured an additional objective, namely an Olympus objective, which, in combination with a focusing lens of focal length f_{lens} =180 mm, provides a magnification of $M = 20$. The beam waist at the position of the ion plane (F1) is theoretically on the order of a single µm or below and is therefore too small to be resolved directly. The beam profiler[5] used for the measurements in this section has a detector array with pixel dimensions of 3.69 µm × 3.69 µm, meaning that a single pixel is already larger than the expected spot size.

This limitation is overcome by an indirect measurement scheme implemented at the output of the test setup. After the focus in the ion plane, the Olympus objective re-collimates the addressing beam and, together with the final focusing lens, forms a Keplerian telescope. This optical configuration produces a second focus (F2), which is well resolvable and stands in direct relation to F1 via the magnification.

6.3.1 Spot size characterization after the Photon Gear objective

After assembling the test setup, the distances between the optical elements were matched to the simulated values as accurately as permitted by the available alignment tools. For this purpose, a pocket ruler with an uncertainty of 0.5 mm was used. When feasible, and for distances small enough to allow it, a calibrated digital caliper with a nominal uncertainty of 0.01 mm was employed to further improve the alignment precision. In addition to the intrinsic uncertainties of the measurement devices, parallax alignment errors were considered. These errors arise from imperfect alignment of the observer eye relative to the measurement scale. Since the optical elements were not directly contacted during alignment to avoid surface damage, such parallax errors are unavoidable in this context.

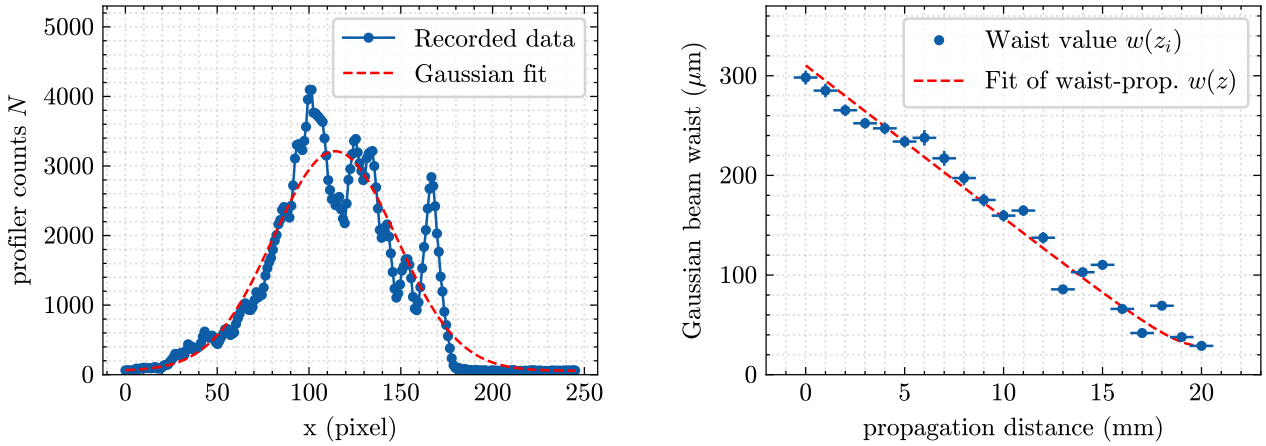
Following the alignment of the opto-mechanical components, the addressing beam was adjusted to illuminate the Photon Gear objective centrally and under normal incidence. The vertical spatial dimension was verified

[5]Ophir Photonics Ltd., Spiricon LBP2 beam profiling camera (SP928 series)

using several height checks with an optical iris, while the orthogonal horizontal dimension was referenced to the threaded hole grid of the optical table.

After all components had been adjusted to the specified alignment tolerances, measurements of the spot size produced by the Photon Gear objective were performed. For these measurements, a beam profiler mounted on a translation stage was used. Fig. 6.6 shows the recorded data and the corresponding evaluation for one exemplary frame (Fig. 6.6(a)), as well as the resulting beam waist evolution over the recorded propagation range (Fig. 6.6(b)).

A focusing lens with a focal length of exactly 180 mm was not available, so one with a focal length of 200 mm was used at the output of the test setup. The final 20 mm of the beam propagation were recorded and the extracted beam waist values were analytically converted according to Eq. 2.2.9 to the effective focal length of 180 mm, ensuring consistency with the magnification of the optical configuration.



(a) (b)

Fig. 6.6: Measurement series using the test setup shown in Fig. 6.5, including the indirect spot size measurement principle. (a) Representative single-frame analysis at the beginning of the recorded beam propagation, positioned 20.0(6) mm before the final focal plane F2. A Gaussian fit yields a beam waist of $w(z_0 = -20\,\text{mm}) = 175(4)\,\mu\text{m}$. (b) Sixteen consecutive frames were analyzed and averaged to obtain one beam waist value per propagation position, with an associated 1σ uncertainty. Adjacent positions were separated by 1 mm, with a total uncertainty in propagation distance of 0.6 mm, arising from the use of a pocket ruler and parallax error. In total, 20 positions were recorded before the final focal plane F2, where optical aberrations remained minimal. A fit using a Gaussian beam waist propagation model $w(z, z_0, w_0, z_R)$ yields a minimal waist of $w_0 = 1.3(2)\,\mu\text{m}$.

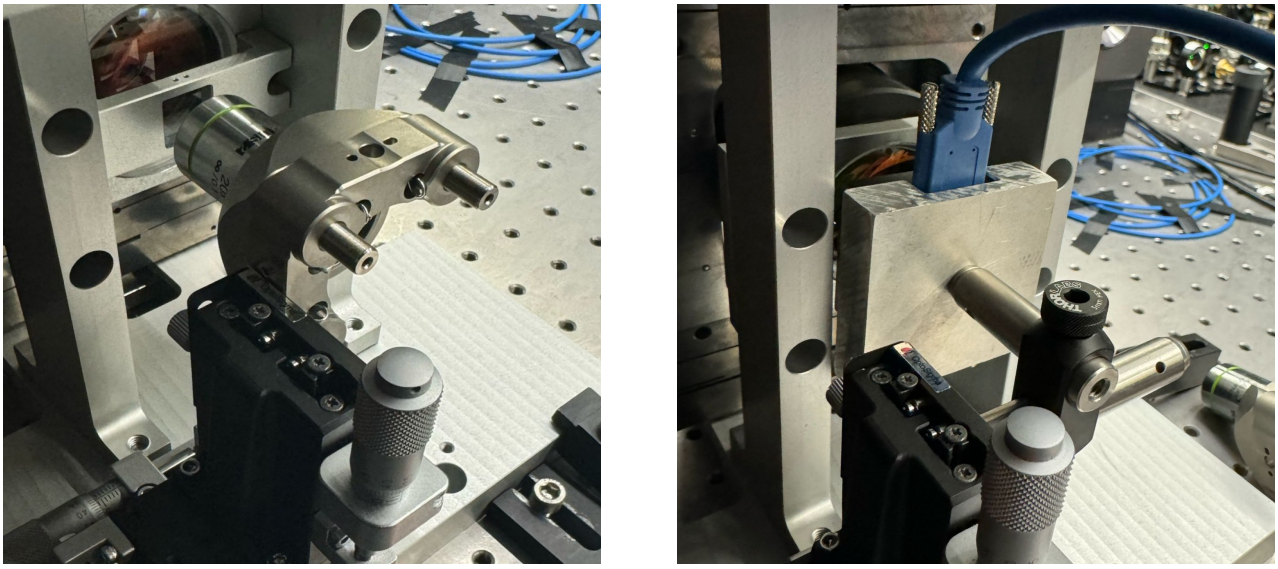
At each of the 20 recorded propagation positions, the beam profiler recorded a total of 16 image frames. For each propagation position, the 16 individual fit results and their associated uncertainties were averaged to obtain a single beam waist value with a corresponding 1σ uncertainty. Inspection of the data and the Gaussian fit of the exemplary frame shown in Fig. 6.6(a) revealed that the transverse beam profile deviated noticeably from an ideal Gaussian distribution. This behavior was most likely attributed to optical aberrations. The influence of these aberrations was also evident in the analyzed data for the full beam propagation shown in Fig. 6.6(b), as these data points were directly based on the individual positional evaluations. In addition, the beam profile on the far side of the final focus F2 consistently exhibited stronger distortions than on the near side.

As a consequence, the Gaussian beam waist propagation could only be fitted asymmetrically with respect to the focal plane F2, rather than around it. Furthermore, the coefficient of determination, R^2, defined as:

$$R^2 = 1 - \frac{\sum_i (y_i - f_i)^2}{\sum_i (y_i - \bar{y})^2}\,, \tag{6.3.1}$$

was used to assess the quality of the fits by quantifying the deviation of the experimental data from the physical model through the corresponding residuals [98]. The fit model and the number of free parameters were fixed for all datasets, preventing artificial increases of R^2 through over-parameterization. The individual fit results for each position were averaged and yielded values below 0.87, as did the resulting global fit of the Gaussian beam waist propagation. This result indicates that neither the individual positional fits nor the resulting global fit of the Gaussian beam waist propagation were of sufficient quality to support quantitative conclusions. The fitted spot size values obtained from this analysis can therefore only be interpreted as upper thresholds for the achievable spot size when using the complete test setup.

Realigning the objectives and adjusting their relative angular tilt had no measurable effect on the aberrations. Despite considerable effort and senior support, this strategy did not lead to any improvement. Therefore, the approach was altered: instead of relying on the indirect characterization scheme via a Keplerian telescope using the complete test setup, the beam propagation of interest around the focal plane F1 was measured directly. A custom adapter mount was fabricated, allowing the beam profiler to be positioned within the confined space of the test setup (Fig. 6.7(b)), after which the Keplerian telescope based on the Olympus objective and the corresponding focusing lens were replaced (Fig. 6.7(a)). The region of interest, the focal area in the ion plane, indicated by the red box around F1 in Fig. 6.5, was thus directly accessible. Although the spot size of the focus in the ion plane F1 remained too small to be resolved, the waist evolution in this region could be recorded directly.



(a) (b)

Fig. 6.7: Test setup and an adapted version of it. (a) Olympus objective on a custom-made mount, resting on a 3D translation stage. (b) Custom-made adapter holding a beam profiler for measuring the Gaussian beam propagation directly after the test window.

For all measurement runs employing this direct approach, the beam profiler was placed immediately after the test window, at the minimum achievable distance permitted by the device dimensions and the required neutral-density (ND) filters protecting it. The same adapter mount holding the beam profiler in the test setup was used to determine the position of the focal plane F1 produced by the Photon Gear objective behind the test window, yielding a focal length of $f_{\mathrm{PG}} = 16.20(5)\,\mathrm{mm}$. Using this focal plane as a reference point, all beam profiler measurement runs were translated into a common axial coordinate system. Within this coordinate system, the minimum beam waist was consistently observed at a position corresponding to an effective detector offset of approximately $13.27(5)\,\mathrm{mm}$ behind the test window.

The first measurement runs using the direct approach showed that the previously observed optical aberrations encountered when using the complete test setup were no longer present. This observation indicates the aberrations originate in the re-imaging stage (Olympus objective + relay), not in the Photon Gear objective. The possible causes of these aberrations are therefore narrowed down to either a relative angular misalignment between the two objectives, which could not be corrected, or an insufficient optical aperture of the Olympus objective for the strongly diverging beam. With this optical limitation bypassed by the direct measurement approach, data could be recorded in the focal region with sufficient fit quality to permit a reliable interpretation of the results.

After using mechanical instruments as guidance to align the beam profiler orthogonally to the beam propagation path directly after the test window, the two mirrors in front of the Photon Gear objective, M1 and M2, were used for beam walking. The process of beam walking continued until moving the translation stage of the profiler along the propagation direction no longer caused a noticeable shift in the addressing beam position on the detector array. This alignment ensured that there was no relative tilt between the Photon Gear objective and the beam profiler detector array. In Fig. 6.8, the data and the fits for the waist propagation of two separate measurement runs taken with the direct approach are shown.

Again, 16 data frames were recorded for each position, this time, however, symmetrically around the focus F1, and for a total of only 12 different propagation positions. The 16 frames were fitted individually as before

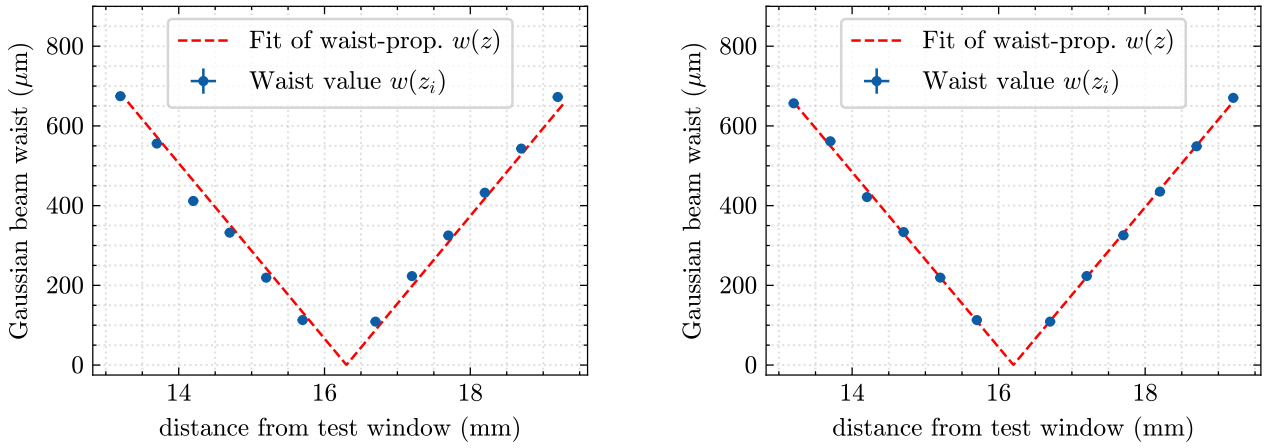


Fig. 6.8: Measurement series using the adapted test setup with the direct approach of recording directly (starting approximately 13.27 mm after the test window). (a): Gaussian beam waist as a function of propagation distance **without** the AOD in place. The fit yields a minimal waist of $w_0 = 851(9)$ nm and a spatial offset of $z_0 = 16.2(1)$ mm. (b): Same as (a) but **with** the AOD in place. The fit yields a minimal waist of $w_0 = 772(4)$ nm and a spatial offset of $z_0 = 16.2(1)$ mm.

and then averaged to obtain the waist value at a given propagation position and its uncertainty. The resulting data points and their least-squares evaluation can be seen in Fig. 6.8. The uncertainty in the propagation distance, 70 µm, arising from the combined contributions of calibrated caliper uncertainty, parallax error, and thermal expansion of aluminum, is not visible in the plot, as the total recorded propagation range exceeds this value by approximately a factor of 100. For the same reason, the individual uncertainties of the beam waist values (4 µm to 13 µm) are not resolved. Given the strong convergence and divergence of the beam around the focus, with a Rayleigh length of only 3.51 µm, the resulting y-axis scaling prevents these error bars from being resolved. The measured waist evolution is well described by Gaussian beam propagation with an average value for the coefficient of determination $R^2 > 0.99$. Since with this direct approach the minimum waist and the region around it could neither be recorded, the minimum waist w_0 was fitted according to Eq. 2.2.4 assuming an ideal effective beam quality factor of $M^2 = 1$.

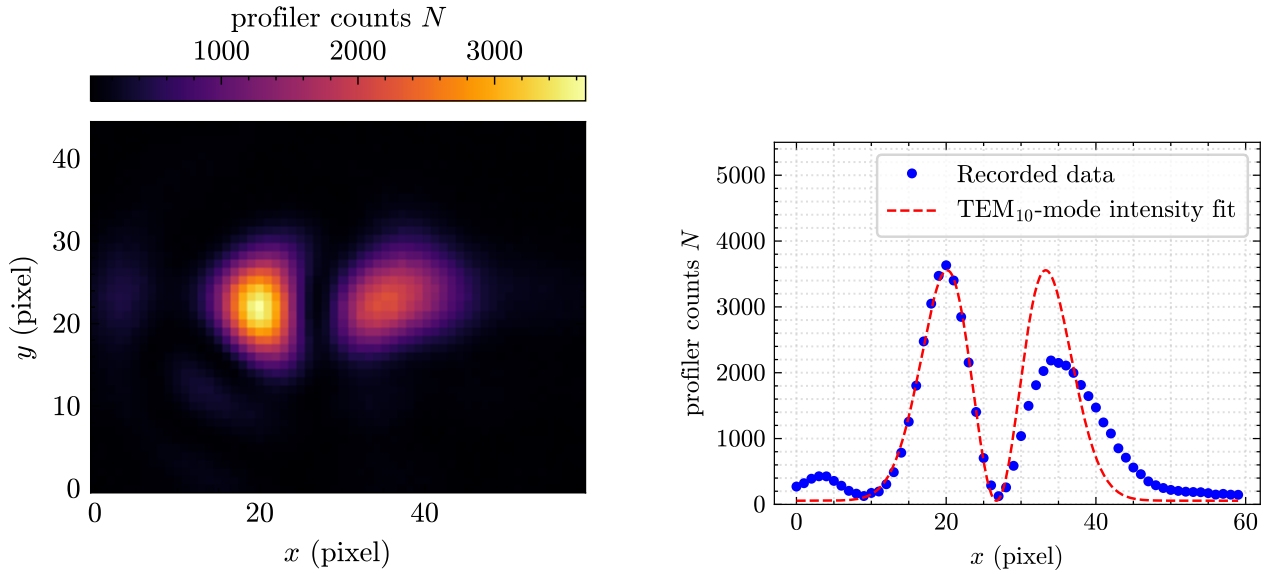
In the specific measurement run shown in Fig. 6.8(a), the AOD was removed from the optical path to test whether any difference in the beam properties would occur, which was not the case. The fit of the Gaussian beam waist propagation reveals a minimum beam radius of $w_0 = 851(9)$ nm. The plot in Fig. 6.8(b) shows the same measurement, now with the AOD in place. The analysis yields a minimum beam radius of $w_0 = 772(4)$ nm. This waist value obtained with the AOD in place represents the closest achieved match to the minimal attainable spot size, which is diffraction-limited and corresponds to the Airy disk radius given by Eq. 2.2.10. The diffraction limit determines the smallest possible spot size as a function of the wavelength under consideration and the numerical aperture (NA) of the optical system [27]. For the NA of the present system and the used wavelength, the theoretical limit amounts to:

$$r_{\text{min}} = \frac{1.22}{2} \cdot \frac{\lambda}{n \sin\theta} = 0.61 \cdot \frac{\lambda}{\text{NA}} = 406\,\text{nm}\ .$$

Based on the analysis, the most likely factor limiting the achievable spot size at the time of these measurements with the test setup was the beam-expander objective, in particular the condition of its tip. The beam-expander converts the collimated beam into a diverging beam and provides several degrees of freedom, in particular adjustable separations between the two elements of the expander and the position of the final lens (the tip), as described in more detail in Sec. 5.1. Together with the distances between the optical elements along the propagation path and the properties of the collimated input beam, these degrees of freedom determine the depth and size of the focus. The issue of the beam-expander tip being mechanically stuck was resolved later, during the implementation of the addressing system in the experiment. After correcting this condition, subsequent tests using ions as quantum-metrology sensors yielded results closer to the diffraction limit (in average 640 nm), indicating the system limitations of the optical addressing were almost reached during the measurements with the test setup.

The spatial offset values obtained from the data shown in Fig. 6.8, which correspond to the focal length of the Photon Gear objective behind the test window, initially indicated a potential discrepancy. The experimental design requires the focus to be located approximately 18 mm behind the ion-trap viewport, whereas the measurement results suggested a value of 16.2 mm behind the test window. Upon further investigation, this discrepancy was traced back to the use of an outdated simulation configuration. In the two simulation versions, the beam-propagation distance from the end of the addressing unit to the illumination point of the Photon Gear objective differed by 2.1 cm. The experimental result was therefore re-evaluated using Zemax with the beam-propagation distances corresponding to the test setup as implemented. Under these conditions, the simulation reproduces the measured focal position of 16.2 mm behind the test window. This result confirms that, for the intended final geometry, the focus is correctly located at the ion plane, approximately 18 mm behind the ion-trap viewport.

For the counter-propagating addressing unit providing the TEM_{10} mode, a similar strategy was followed. First, the complete test setup was used and the focus was optimized for a single-shot measurement, as shown in Fig. 6.9. However, this approach again proved to be of limited success. Due to optical aberrations, only one half of the mode exhibited the expected intensity distribution, as illustrated in Fig. 6.9(a). A one-dimensional intensity profile derived from Eq. 2.2.7 was fitted to the measured data using a least-squares procedure, as shown in Fig. 6.9(b). This fit yields a minimum waist size of $w_0 = 1.5(2)\,\mu\mathrm{m}$. However, the goodness of fit, characterized by an R^2 value of 0.75, limits the confidence with which the result can be interpreted. The obtained value can therefore only be regarded as an upper-bound estimate.



(a) (b)

Fig. 6.9: Visualization and data analysis of the Hermite-Gaussian TEM_{10} mode in focus F2 (as indicated in the test setup schematic of Fig. 6.5) using the whole test setup. (a) Image of the TEM_{10} mode, taken with a beam profiler. (b) Analysis of the TEM_{10} mode yielding a minimal waist of $w_0 = 1.5(2)\,\mu\mathrm{m}$.

Next, the direct measurement approach was applied again, and propagation data points were recorded directly after the test window (F1 in the schematic of Fig. 6.5), where the previously observed optical aberrations were avoided. Representative frames of these measurements are shown in Fig. 6.10. The initial measurement position was chosen immediately after the test window, identical to the starting position used for the TEM_{00} case. Characterizing the properties of the TEM_{10} mode beam requires fitting the corresponding intensity distribution for each recorded propagation position within the framework of Fourier optics. In contrast to the fundamental mode, the TEM_{10} mode intensity profile cannot be described by a simple Gaussian beam model when transitioning between Fourier space and real space. Instead, its propagation must be modeled using either a partial Fourier transformation or an explicit Fresnel diffraction integral approach:

$$U(x', y', z) = \frac{e^{ikz}}{i\lambda z} \iint U(x, y, 0)\, \exp\left[\frac{ik}{2z}\left((x' - x)^2 + (y' - y)^2\right)\right] dx\, dy\ , \tag{6.3.2}$$

which must be evaluated for each individual propagation position [30]. However, a convenient relation exists, introduced as Eq. 2.2.8 in Sec. 2.2, that connects the waist $w(z)$ of a fundamental TEM_{00} mode to that of a

general $\mathrm{TEM}_{\mathrm{nm}}$ mode [27]. This relation implies:

$$w_{0,(n=1,m=0)} = w_0 \sqrt{2n+1}\sqrt{2m+1} = w_0\sqrt{3}\ , \tag{6.3.3}$$

which permits the result of the TEM_{00} mode analysis to be scaled by a factor of $\sqrt{3}$. For the minimal beam waist of the TEM_{10} mode, this yields $w_{0,(1,0)} = 1.337(7)\,\mu\mathrm{m}$. This approach is justified, since at the time of these measurements only a single input collimator was available for the characterization of both addressing units. The fundamental waist w_0 at the entrance of the addressing optics thus remained unchanged between the measurements of the two units.

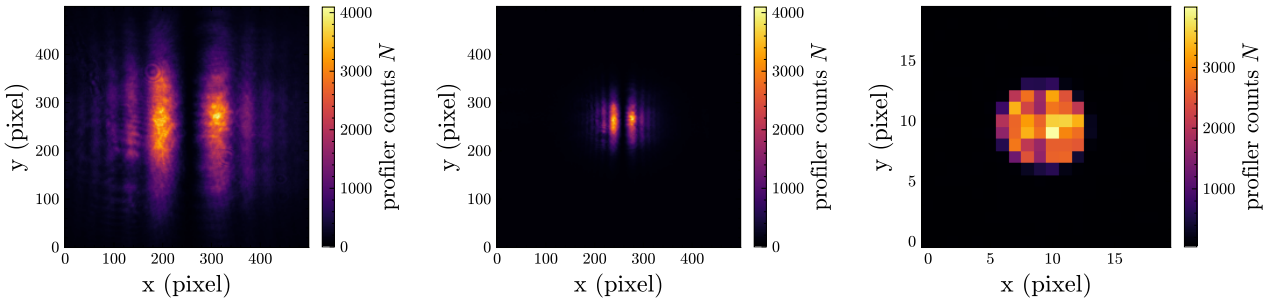


Fig. 6.10: Visualization of TEM_{10} mode propagation directly after the test window around focus F1 (as indicated in the test setup schematic of Fig. 6.5). (a) TEM_{10} Fourier-space pattern at the starting position directly behind the test window (before focal plane F1 and approximately 13.27 mm after the test window). (b) TEM_{10} Fourier-space pattern after 4 mm of propagation distance relative to the starting position. (c) Real-space manifestation of the TEM_{10} mode near the focal plane F1 after 6 mm propagation relative to the starting position.

6.3.2 Deflection range

Another aspect investigated with this particular test setup, whose schematic is shown in Fig. 6.5, was the maximum achievable deflection angle of the AOD device. This angle directly determines the spatial range that the focus of the addressing beam can cover within the ion plane of the trap, referred to as the deflection range. Together with the axial trap voltage and the number of ions loaded, both of which set the inter-ion spacing, the deflection range determines the total number of ions that can be addressed [83].

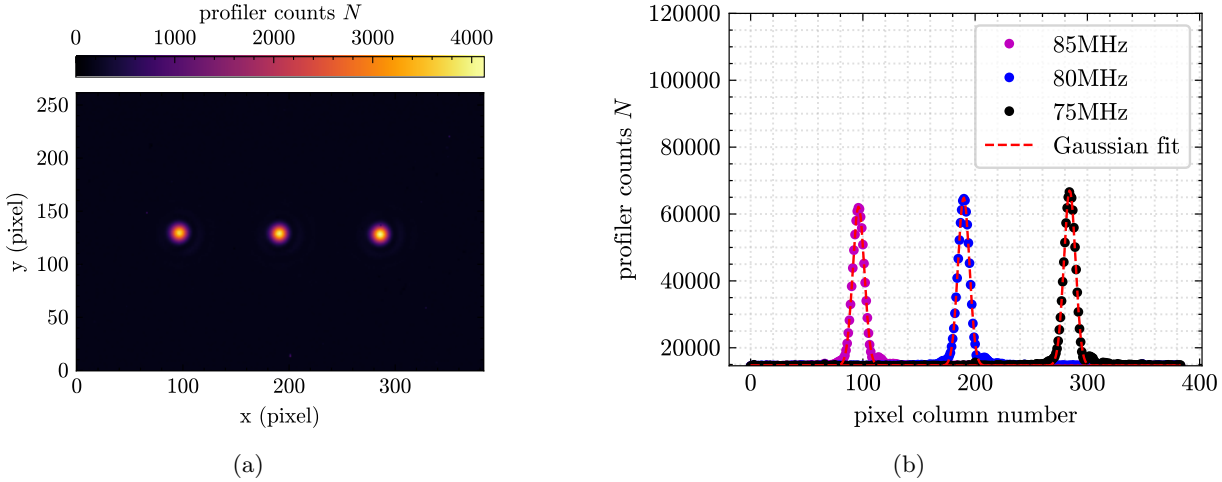


Fig. 6.11: (a): Three laser beam positions for three different RF frequencies (75 MHz, 80 MHz, 85 MHz) applied to the AOD. (b): Analysis of the three positions shown in (a), yielding positional pixel offsets of Gaussian fit model $x_0 = 96.09(1),\ 189.88(1),\ 284.04(1)$ from left to right.

The complete test setup enabled measurements probing the total bandwidth over a range of approximately 10 MHz around the central frequency, while remaining within the sensor array of the beam profiler. Accordingly, eleven distinct deflection positions were recorded, corresponding to eleven RF frequencies spaced by 1 MHz

around the central frequency $\nu_0 \approx 80\,\mathrm{MHz}$. Fig. 6.11(a) shows a composite image of three representative beam spots corresponding to the central frequency and the two extrema of the accessible RF input frequency range of the first AOD. The quantitative analysis of the recorded data is presented in Fig. 6.11(b).

For this investigation, an additional optical iris was introduced and installed on the front side of the Photon Gear objective. By closing the iris and thereby blocking a large fraction of the incoming beam, the resulting spot size in the ion plane F1 was effectively increased, in accordance with Eq. 2.2.10. While the spot size in the focal plane of the Photon Gear objective changed, the propagation wave vector of the beam remained theoretically unchanged.

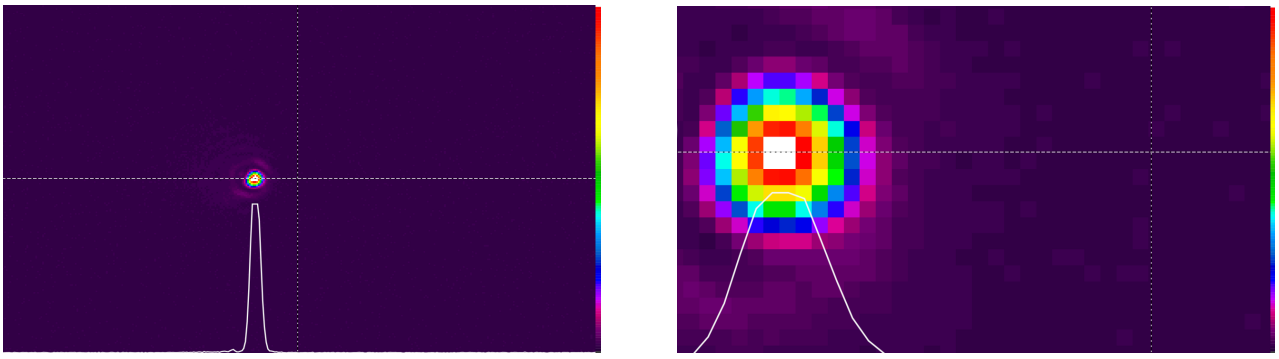
This theoretical expectation was verified experimentally by selecting a region of interest (ROI) on the beam profiler device. The ROI was defined with the iris fully opened, while observing the accessible range of the addressing beam, including the presence of optical aberrations, in the final focal plane F2. After closing the iris, the same ROI remained accessible for the now aberration-free addressing beam. This approach yields beam spots that are easier to fit and analyze, while still covering the same spatial range as the original distorted spots. The resulting measurement series and its analysis indicate a total deflection range of 156(9) µm over the full bandwidth range of 50 MHz. A second, simplified test setup qualitatively confirmed this value for the other AOD device, consistent with the deflection angle of 41 mrad stated in the data sheet over the full considered bandwidth.

The observation that this increased spot size could be imaged correctly at focus F2 using the complete test setup demonstrates that the observed optical aberrations originate from the combination of an insufficient optical aperture of the specific Olympus objective and a relative angular tilt between the two objectives used in the test setup. For the smaller spot size produced by the Photon Gear objective, the beam diverges too strongly such that, despite a working distance of 1.2 mm to the Olympus objective, its full aperture becomes illuminated. As a consequence, the beam is partially clipped, leading to scattering and interference effects that give rise to optical aberrations, independent of the optical alignment.

6.3.3 Estimation of Airy fringe induced crosstalk

When light passes through a circular aperture such as a lens, pupil, or pinhole, every point of the aperture acts as a secondary source according to the Huygens–Fresnel principle [90]. As a result, the incoming light wave does not form a perfectly sharp focus but instead undergoes diffraction. The secondary wavelets interfere constructively and destructively, thereby forming concentric bright rings around the focus, known as Airy fringes [31].

In our experiment, the entrance field diameter of the Photon Gear objective is matched, and the formation of Airy fringes in the ion plane F1 must therefore be expected [90]. To investigate the magnitude of ion crosstalk induced by these Airy fringes, measurements using the complete test setup were required. A beam profiler was positioned at focus F2, as indicated in Fig. 6.5, and the position of the nearest neighboring ion was assumed to be 4 µm, which for $^{138}Ba^{+}$ ions corresponds to an axial trap frequency of $\omega_{\mathrm{axial}} \approx 470\,\mathrm{kHz}$ according to numerical simulation.



(a) (b)

Fig. 6.12: Recorded data used to estimate crosstalk caused by the Airy fringe on the neighboring ion. (a) beam profiler image of the TEM_{00} mode addressing beam after the full test setup, recorded with an exposure time of 64 µs. The crosshair marks the position of the neighboring ion when the addressing beam is centered on the target ion. (b) Zoom-in of (a).

The magnification of the Keplerian telescope, formed by the Olympus objective and the corresponding focusing lens, together with the pixel dimension of the beam profiler device was used to calculate the approximate position of the assumed neighboring ion (Fig. 6.12). The exposure time was then increased until the pixel of the beam profiler array at the position corresponding to the neighboring ion reached saturation (Fig. 6.13). The linear relation between exposure time and photon flux (intensity) allowed the estimation of Airy fringe magnitude at the assumed neighboring-ion position in comparison to the actually addressed ion.

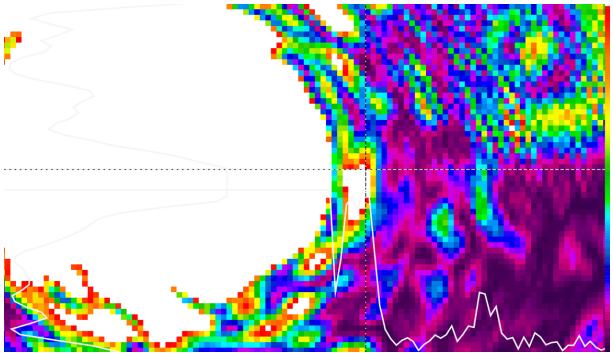


Fig. 6.13: Saturation test of the beam profiler sensor at the position corresponding to a neighboring ion. The exposure time needed to be increased to 419 ms to reach saturation on that pixel.

Asymmetric aberrations in the final focal plane F2 complicated the assessment of crosstalk induced by the Airy fringes. Consequently, the crosstalk was evaluated on both sides of the focus, and the final estimate was obtained by averaging the two values. This procedure yields a first Airy-fringe crosstalk of 0.17(16) %, which is acceptable for Raman gate operations, since the Raman Rabi frequency depends on the product of the two addressing fields ($\Omega_\mathrm{R} \propto E_1 E_2$).

6.4 Quantification of aberrations through addressing optics

Possible optical aberrations of both addressing units and their individual components were quantified using the Nijboer–Zernike diffraction theorem, which is introduced and discussed in more detail in Sec. 2.2. The corresponding Zernike coefficients can be measured using a wavefront-sensor[6]. However, care must be taken, as multiple conventions exist for the ordering and indexing of the Zernike modes. The specific wavefront-sensor device used for this characterization defines Z-4 as the astigmatism Zernike coefficient rotated by 45° with respect to the optical axis (denoted by Z_2^{-2}), Z-5 as the defocus (Z_2^{0}), and Z-6 (Z_2^{+2}) as the astigmatism Zernike coefficient.

As a first step, the influence of the AOD device itself was investigated. Measurements were performed at two RF frequencies—the central drive frequency and a frequency at the edge of the acoustic bandwidth—each at two different RF power settings. For each configuration, the data were averaged over 100 samples. The resulting second-order Zernike coefficients of the first AOD device are summarized in Tab. 6.1. Based on the specified wavefront-sensor sensitivity of $\lambda/15$ and the number of samples, an uncertainty of $\pm 0.007 \cdot \lambda$ per coefficient is obtained and indicated only for the first table entry ($\lambda = 532\,\mathrm{nm}$). Although coefficients up to fourth order were extracted, all higher-order terms remain negligible within this uncertainty and are therefore omitted. No statistically significant dependence on RF power or drive frequency is observed, indicating that neither parameter constrains the operating regime with respect to beam quality.

Table 6.1: Measurement of Zernike coefficients for different RF frequencies (RF-F) and RF powers (RF-P) applied to the first AOD device, with the remainder of the addressing unit excluded. All Zernike coefficients are given in units of the wavelength $\lambda = 532\,\mathrm{nm}$.

1st AOD	**RF-F = 80 MHz**		**RF-F = 105 MHz**	
Zernike Coefficient	**RF-P = −5.8 dBm**	**RF-P = −8.8 dBm**	**RF-P = −5.8 dBm**	**RF-P = −8.8 dBm**
Z-4 (2/ − 2)	−0.012(7)	−0.010	−0.009	−0.008
Z-5 (2/0)	0.044	0.045	0.046	0.044
Z-6 (2/2)	−0.014	−0.013	−0.010	−0.009

[6]Thorlabs Shack–Hartmann wavefront sensor, WFS series (WFS150-5C)

The next step involved a series of measurements was performed to investigate the Zernike coefficients of individual optical components as well as their combined effects in different configurations. The measurements were again carried out using the wavefront sensor and averaged over one hundred measurement shots. The corresponding results are presented in Tab. 6.2 and carry the same uncertainty as in the AOD investigation. Only second-order Zernike coefficients are presented, as all higher-order terms remain negligible within the uncertainty, with the exception of the Trefoil aberration coefficient, stated here explicitly as $Z_3^{+3} = -0.009 \cdot \lambda$.

Table 6.2: Measurement of Zernike coefficients, given in units of wavelength $\lambda = 532\,\text{nm}$, for various configurations of the addressing unit's optical components, comparing partial setups to the fully assembled system.

Zernike-Coefficient	**Setup 1**	**Setup 2**	**Setup 3**	**Setup 4**	**Setup 5**	**Setup 6**
Z-4 $(2/-2)$	0.001	0.003	−0.005	0	−0.008	−0.010
Z-5 $(2/0)$	0.045	−0.100	0.050	0.046	0.047	−1.006
Z-6 $(2/2)$	−0.007	−0.500	0.003	−0.006	−0.003	0.054

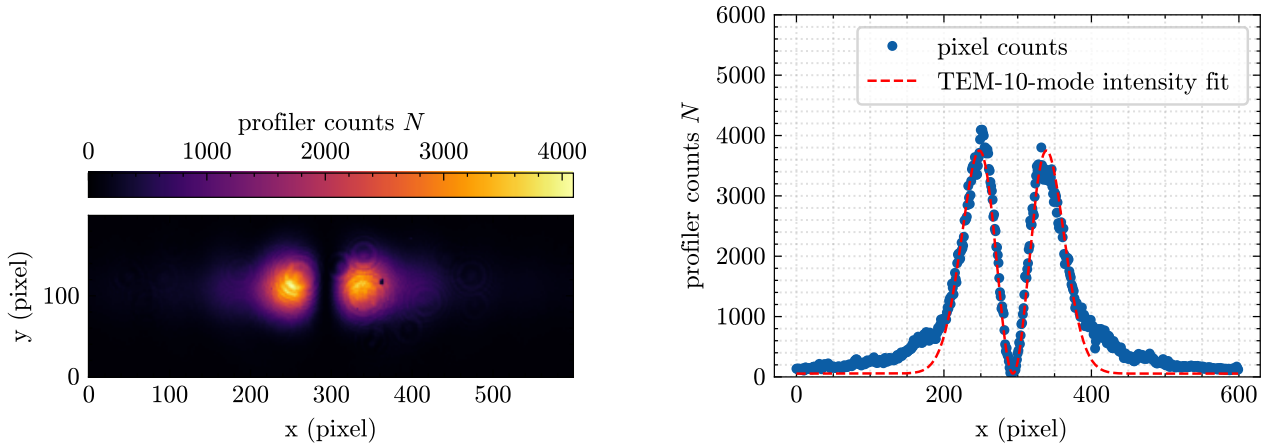
Setup 1 is the collimator alone, the starting point of this analysis, and part of every setup as it is the light source. Setup 2 looks at the elliptical beam shaper alone (next to the input collimator). The effects on the fundamental input Gaussian beam are clearly visible, compared to setup 1. Z-5, the so-called defocus, and Z-6, the astigmatism Zernike coefficient, are altered substantially. This increase in the astigmatism coefficient is expected, as the elliptical beam shaper deliberately introduces astigmatism by design through converting a symmetrical input beam into an elliptical output one. The defocus coefficient, on the other hand, most likely arises from non-optimized spacing between the shaper elements during this measurement. The next configuration, setup 3, consisted of input collimator and all reflective parts of the addressing unit. More specific the two prisms and the dielectric mirror. Compared again to the input, setup 1, there is hardly a significant change in any of the relevant Zernike coefficients.

In setup 4 three phase retarding wave plates were added to setup 3, two $\lambda/2$ and one $\lambda/4$. In setup 5 another optical element was added on top of those in setup 4: a Glan-Taylor polarization cleaning prism. These configurations, setup 4 and setup 5, also show hardly any differences compared with the input alone in setup 1. Finally, in the last measurement all parts of the addressing unit, with the exception of the phase plate, were observed together in setup 6. The most notable differences cause the elliptical beam shaper and the beam-expander objective. With the beam-expander objective in place though, also the change in the defocus coefficient is expected naturally. As the observed changes are consistent with the expected diverging behavior (defocus coefficient), the investigation reveals no indication of a systematic issue. Consequently, no adaptations for optimization were required.

6.5 Quality of created TEM_{10} mode

The quality of the generated TEM_{10} Hermite–Gaussian mode is investigated in this section, as deviations from the ideal mode profile could affect the addressing fidelity and crosstalk performance of the system. As described in Sec. 5.2, the mode is generated using a phase plate mounted in a specially designed adapter. The resulting interference pattern in the Fourier plane is imaged onto a beam profiler, on which a series of 16 single-shot measurements is recorded. A lens with a large focal length ($f_l = 500\,\text{mm}$) is employed to ensure that the image in the focal plane is sufficiently large to be conveniently resolved, in accordance with Eq. 2.2.9. One exemplary measurement, together with the corresponding analyzed data, is shown in Fig. 6.14. The fit is performed along a single transverse dimension only with the coefficient of determination, averaged over the fits performed in this measurement series and quoted with one standard deviation of uncertainty, amounting to $R^2 = 0.934(1)$. This value indicates good agreement between the physical fit model and the recorded data. The result therefore confirms that the phase plate generates a TEM_{10} Hermite–Gaussian mode with a quality consistent with the requirements of the addressing experiment.

During this measurement, a residual lateral misalignment between the input collimator and the phase plate produced a visible asymmetry in the intensity peaks, as shown in Fig. 6.14(b). The average relative difference between the two peak intensities in this measurement series amounts to $8(2)\,\%$. An analysis of the residuals shows that the deviation from the ideal value of $R^2 = 1$, which corresponds to perfect agreement between the physical model and the measured data, can be attributed partly to this asymmetry in peak height and, more significantly, to the observed lobes. The physical origin of these lobes is discussed in Sec. 5.2. At a later stage, the alignment was readjusted, resulting in an improved symmetry of the intensity profile. The results presented here should therefore be regarded as a conservative lower bound on the mode quality achievable with the phase plate itself, with the performance in the final experimental configuration expected to be higher.



(a) (b)

Fig. 6.14: Visualization and quantitative characterization of the generated TEM_{10} mode. (a) Single-shot beam profiler image visualizing the generated TEM_{10} mode. (b) Intensity profile along the pixel row with maximum illumination, fitted using the theoretical TEM_{10} distribution (based on Eq. 2.2.7, for one spatial dimension x only) to assess the mode quality.

6.6 Contrast investigation of addressing beam superposition

This investigation is motivated by the question of how well the two addressing beams can be superimposed under realistic experimental conditions. As explained in Sec. 2.6, the transverse gate operation investigated in this experiment relies on the gradient force arising from the intensity distribution of the superimposed addressing beams to control both the sign and the magnitude of the AC-Stark shift, which in turn determines the phase acquired by the addressed ion. The more precisely the two beams interfere, both constructively and destructively, the more accurately the intended phase shifts can be imparted. The achievable interference contrast, commonly referred to as the visibility, is defined in terms of the maximal and minimal intensities:

$$C := \frac{I_{\max} - I_{\min}}{I_{\max} + I_{\min}} , \tag{6.6.1}$$

where the constant prefactor depends only on the fixed spatial position and the chosen field-amplitude ratio. The visibility is a relevant figure of merit, as it provides a direct characterization of the beam superposition quality. For the investigation of the contrast, the two double-pass AOMs of the control breadboard, depicted and described in Sec. 4.3, were used as the light source in a test setup configured as shown in Fig. 6.15. One arm of the test setup supported the fundamental TEM_{00} mode, while the second arm was used for the generation of the TEM_{10} mode by means of the phase plate. The phase plate was mounted on a one-dimensional translation stage, which enabled precise alignment of the beam such that it passed centrally through the plate. An additional $\lambda/2$ phase-retarding wave plate in the TEM_{00} arm provided the degree of freedom required to adjust the relative polarization between the two arms and, consequently, between the two addressing modes. A 50:50 beam-splitter cube combined the optical fields from both arms with equal intensity, independent of their polarization, thereby allowing the superposition of the two modes. The mirror (M), in combination with the fiber collimator mounts, was used to optimize the spatial overlap of the two beams. The resulting superimposed intensity distribution was then imaged onto the detector array of the beam profiler device using a focusing lens.

A dual-channel RF signal generator[7] was used to drive the double-pass AOMs of the control breadboard. The device provides a common clocked frequency reference for both output channels and allows adjustment of the relative phase between the two outputs. Despite these capabilities, the relative phase could not be held fixed over the duration of the measurement. Instead, the superposition of the two modes exhibited a slow and irregular temporal beating. While the dual-channel RF signal generator itself operated as specified, environmental influences such as mechanical vibrations, air currents, and possible pressure fluctuations in the optical fibers led to random phase drifts. Additional systematic effects, including polarization instability at the fiber collimators, further contributed to the observed temporal beating.

Since this issue could not be resolved without implementing additional stabilizing mechanisms, multiple image series comprising a total of 64 frames of the slowly and randomly beating interference pattern were recorded, ensuring that the points of interest, or positions very close to them, were captured within the dataset.

[7] Windfreak Technologies, SynthHD (v2)

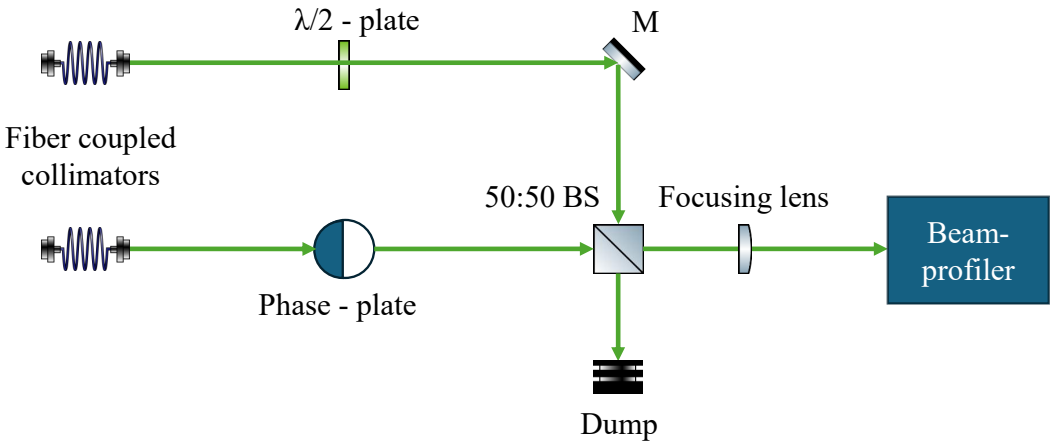


Fig. 6.15: Schematic of the test setup used to investigate polarization-dependent interference and the resulting contrast achievable. Two fiber-coupled collimators are supplied with 532 nm light from the respective AOM double-pass paths of the control breadboard (see Fig. 4.7). The beams are combined in a Mach–Zehnder–like interferometer geometry, where one arm contains the TEM_{00} addressing beam and the other passes through the phase plate to generate the TEM_{10} addressing beam. A $\lambda/2$ phase-retarding wave plate before the non-polarizing 50:50 beam splitter (BS) enables polarization tuning without modifying the beam intensities.

Fig. 6.16 shows a representative image from the measurement series recorded with opposite polarizations of the two addressing modes. All frames in this dataset are statistically identical, as the conditions required for interference are not met when the polarizations are orthogonal. While the absence of interference in this configuration is expected from a theoretical standpoint, it was nevertheless recorded and included in the final evaluation of the contrast as a function of the polarization difference.

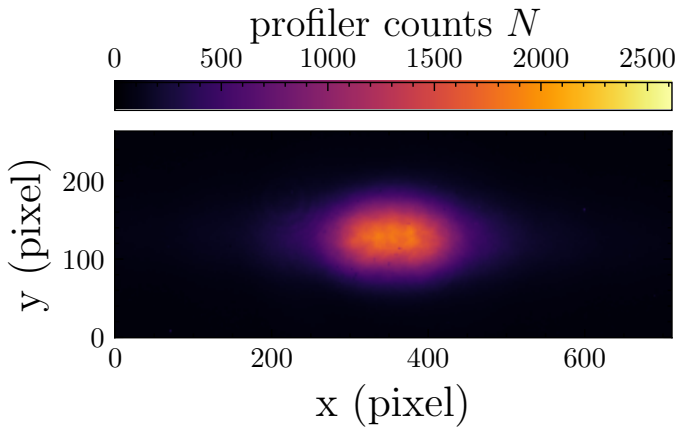


Fig. 6.16: Exemplary image of the superposition between the TEM_{00} and TEM_{10} addressing beams with orthogonal polarization, resulting in suppressed interference.

The other extreme, corresponding to a superposition with identical polarizations, is shown in Fig. 6.17. This configuration produces the temporal intensity distribution ideally required for driving the transverse gate operation investigated in our experiment, which relies on an intensity gradient, as illustrated earlier in Fig. 2.23. In Fig. 6.17(a), the superposition corresponds to a phase difference of $\Delta\phi(t) = 0$. In Fig. 6.17(b), the system is shown at the intermediate phase of the temporal beating, corresponding to $\Delta\phi(t) = \pi/2$. Finally, Fig. 6.17(c) shows the opposite turning point of the beating, at a phase difference of $\Delta\phi(t) = \pi$.

A measurement series comprising 5 different relative polarization differences, ranging from identical to orthogonal polarizations, enables the investigation of the contrast over the full polarization-difference range, as shown in Fig. 6.18. The analysis strategy for each data point therein proceeded as follows: one frame of the respective series was selected, and the pixel with maximal intensity was identified by fitting the expected intensity distribution given in Eq. 2.6.16. The obtained pixel position was then used to extract the intensity at the same position in all other recorded frames of that series. In this way, the contrast C was calculated for each frame pair in the series according to Eq. 6.6.1.

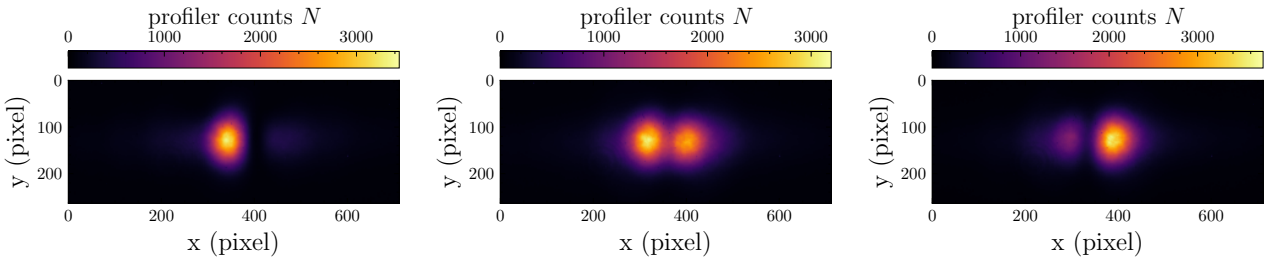


Fig. 6.17: Three exemplary images recorded with identical polarization settings, showing the superposition of the TEM_{00} and TEM_{10} addressing beams for different time-dependent phase differences $\Delta\phi(t)$. (a) Superposition at $\Delta\phi(t) = 0$. (b) Superposition at $\Delta\phi(t) = \pi/2$. (c) Superposition at $\Delta\phi(t) = \pi$.

The 100 largest contrast values among the total measurement series were selected to determine the mean and spread of the maximum achievable contrast, corresponding to frames closest to constructive and destructive interference and yielding a variance that remained stable against moderate changes in the selection size. For orthogonal polarization settings, all obtained contrast values were included in the final evaluation, as without interference the distribution of pairwise contrasts is dominated by intensity fluctuations arising from registration noise in the single-pixel evaluation. The theoretical model employed for the least-squares fitting of the polarization-dependent contrast C is based on Eq. 2.6.16 and, in combination with the definition of the contrast, yields:

$$C = \frac{2\sqrt{2}E_0E_1(x-x_0)}{E_0^2 + 2(x-x_0)E_1^2} \cdot \left|\cos\left(\angle(\boldsymbol{\epsilon}_0, \boldsymbol{\epsilon}_1)\right)\right| = \text{const.} \cdot \left|\cos\left(\angle(\boldsymbol{\epsilon}_0, \boldsymbol{\epsilon}_1)\right)\right| , \tag{6.6.2}$$

where the expression is evaluated for a fixed spatial position and a fixed absolute field ratio E_0/E_1.

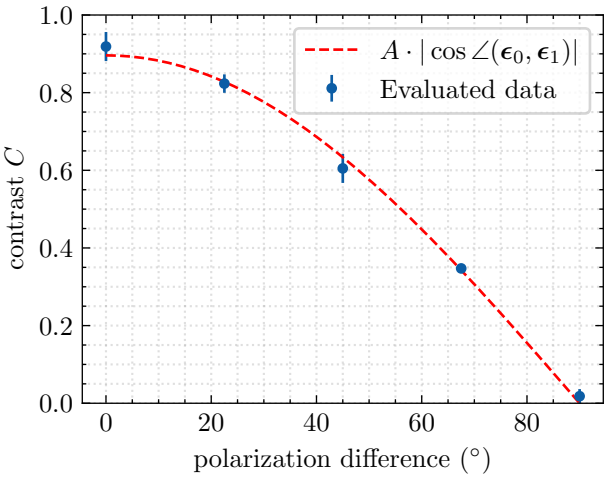


Fig. 6.18: Polarization-dependent contrast C of the superposition of the TEM_{00} and TEM_{10} addressing beams. Each data point is obtained from 100 frame pairs sampling the interference beating at different relative phase values, from which the maximal contrast values are extracted. For orthogonal polarization, all 4096 frame pairs are used to determine the mean value and standard deviation, since a single-pixel evaluation in the absence of interference otherwise yields spurious contrast values caused by intensity fluctuations and registration noise. The fit yields an amplitude of $A = 90(1)\,\%$, corresponding to the maximum achievable contrast.

The contrast does not reach unity due to the chosen relative optical powers of the two modes, whereas equal field amplitudes would yield a contrast of one. Under the power settings used throughout this section, with the TEM_{00} power set to approximately two thirds of the TEM_{10} power, a numerical evaluation yields a maximum achievable contrast of $93(3)\,\%$ at the approximate position of the strongest intensity gradient. This power ratio was selected to represent a realistic operating point constrained by scattering. In an addressing system of the present type, the scattering error scales with the field-amplitude ratio, $\propto E_0/E_1$. The ratio employed here therefore reduces the scattering error, which constitutes the dominant limitation in such a setup [99]. The measured data and the corresponding analysis yield a contrast of $C = 90(1)\,\%$, which agrees within uncertainty with the predicted upper bound under the chosen power settings.

6.7 Implementation and performance optimization

This section documents the installation of the addressing system into the experiment. Since the 532 nm addressing light is intrinsically off-resonant with the barium transitions, direct alignment via resonant Rabi oscillations was not possible. Instead, the AC-Stark shift described by Eq. 2.5.28 was exploited in combination with a Ramsey-type sequence, which is discussed in more detail in Sec. 2.6. An illustration of the specific scheme used for optimizing the alignment is shown in Fig. 2.17(b). Within this approach, the ions effectively served as quantum probes for the alignment procedure.

First, a chain of ions was trapped and the system was initialized such that all ions in the register were prepared in the ground state. After initialization, a collective optical $\pi/2$ pulse using coherent 1762 nm light transferred all ions from the ground state to the equatorial plane of the Bloch sphere. In this superposition state, the qubits accumulate a relative phase determined by the energy splitting between the ground and excited states. In the rotating frame defined by the energy splitting, the qubits ideally remain stationary on the Bloch sphere within the coherence time of the system, after which decoherence processes modify the effective phase evolution.

Without addressing any of the ions, the Ramsey time was calibrated to be large and within the coherence time, $\tau_{Ramsey} = 1\,\text{ms}$. At the end of the Ramsey interval, a second collective $\pi/2$ pulse transferred the qubits to the excited state. The system was then reinitialized and the sequence was continuously repeated, with the addressing beam acting during the Ramsey interval between the two collective $\pi/2$ pulses. The search for the AC-Stark shift signal was performed using this continuously running Ramsey sequence, while the degrees of freedom provided by the mirror mounts were adjusted to optimize the alignment of the addressing beam.

As soon as the addressing beam illuminated an ion, the induced AC-Stark shift caused the qubit, which was stationary on the equatorial plane in the rotating frame, to acquire an additional phase during the Ramsey interval. As a result, the final collective $\pi/2$ pulse no longer transferred the addressed qubit to the excited state with a probability of 1. The accumulated phase is proportional to both the Ramsey wait time and the magnitude of the induced AC-Stark shift, allowing the shift strength to be estimated from the measured phase for a given Ramsey time. With increasing AC-Stark shift, the population of the excited state after the final $\pi/2$ pulse was progressively suppressed due to the accumulated phase during the Ramsey interval, indicating improved spatial overlap between the addressed ion and the focus of the radial addressing beam.

For sufficiently large AC-Stark shifts, the qubit was over-rotated, such that the excited-state population increased again after reaching complete suppression. At this point, the Ramsey time was reduced, which weakened the suppression due to the shorter interaction time of the addressing beam. The alignment was then further optimized to suppress the excited-state population again at the reduced Ramsey time. This procedure was iterated until no further improvement was observed and the Ramsey wait time was reduced to a practically achievable minimum of $\tau_{Ramsey} = 100\,\mu\text{s}$.

Once the initial alignment of the addressing beam was completed, an additional aspect was investigated: the focal depth. For this purpose, the relative distance between the Photon Gear microscope objective and the viewport of the ion trap was varied slightly to verify whether the focal plane coincided with the ion plane or was located slightly before or after it. In parallel, the adjustable spacing between the lens groups of the beam-expander objective was used to fine-tune the focal depth.

After the AC-Stark signal strength was optimized, the deflection axis was aligned with the ion chain inside the trap. A relative tilt between the deflection axis and the ion chain would result in a diagonal scan across the ions, thereby inducing different AC-Stark shift magnitudes along the qubit register. The goniometer integrated into the addressing unit was therefore used in combination with beam-walking to align the deflection axis with the ion register, such that variations of the AOD input RF frequency result in beam deflection strictly along the axial trap direction, i.e. along the ion chain, without any relative tilt. The sequence used to verify and visualize this alignment closely resembles the sequence employed for detecting the AC-Stark shift signal. The essential difference is that, in this case, the AOD input RF frequency additionally serves as a scan variable and is incremented between successive sequence cycles. An example of such a Ramsey deflector scan for the fundamental TEM_{00} addressing beam with seven ions in the register is shown in Fig. 6.19.

The separation of the peaks in Fig. 6.19, with a mean value of 1.4(1) MHz, directly reflects the relative position of the focal plane with respect to the ion chain as well as the angular magnification set by the beam-expander tip. An increase in the peak separation corresponds to a focal plane located closer to the ions or to a higher angular magnification. The maximum achievable separation indicates that the ions are positioned in the focal plane under the maximal angular magnification. In addition, the envelope of peaks visible in the scan originates from the selected bandwidth profile of the AOD device and from the absence of optical power stabilization in the addressing system at the time of measurement.

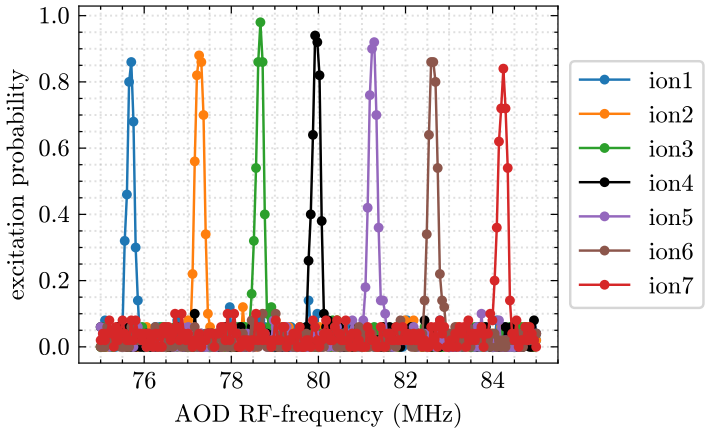


Fig. 6.19: Ramsey-type sequence with underlying single-ion addressing deflector scan with the TEM_{00} mode addressing beam and the Ramsey waiting time fixed at $\tau_{Ramsey} = 100\,\mu\mathrm{s}$.

An analytical simulation including the mass of $^{138}\mathrm{Ba}^{+}$ ions and an axial trap frequency of $\omega_{\mathrm{axial}} = 340\,\mathrm{kHz}$ yields a total distance of 29.5 µm spanned by the 7 ions in the chain and allows translation of the RF frequency scan variable into spatial distances. This relation provides access to the minimum waist of the addressing beam via the measured peak widths. With a mean value of 0.19(1) MHz, the TEM_{00} mode peak widths in Fig. 6.19 correspond to an averaged minimum waist of $w_0 = 0.6(3)\,\mu\mathrm{m}$. A systematic error of one axial pixel dimension (16 µm) of the EMCCD camera was included in this estimate, which is likely to overestimate the actual uncertainty. However, the yielded value is consistent with the minimum waist obtained prior to implementation in the experiment.

The optimization of the optical addressing system with the TEM_{00} mode beam was confirmed using the same Ramsey-type scheme as before, but with a modified measurement protocol. The AOD input RF frequency was kept fixed in order to ensure repeated addressing of the same ion, while the waiting time of the Ramsey sequence served as the scan variable instead of a calibrated, fixed Ramsey time. In this configuration, off-resonant Rabi oscillations induced by the AC-Stark shift were driven on the addressed ion. Due to residual crosstalk in the single-ion addressing, the AC-Stark shift experienced by the other, non-addressed ions likewise induced Rabi oscillations, albeit at significantly lower frequencies. The resulting Rabi frequencies therefore provide a direct measure of the crosstalk error associated with single-ion addressing. The coherent crosstalk coupling from ion j to ion i is quantified by the ratio of the corresponding Rabi frequencies:

$$\epsilon_{i|j} = \frac{\Omega_i}{\Omega_j}\,, \tag{6.7.1}$$

where Ω_j denotes the Rabi frequency of the addressed ion and Ω_i the undesired coherent coupling on ion i. An exemplary Ramsey time scan for addressing the first of the 7 ions in the chain is shown in Fig. 6.20.

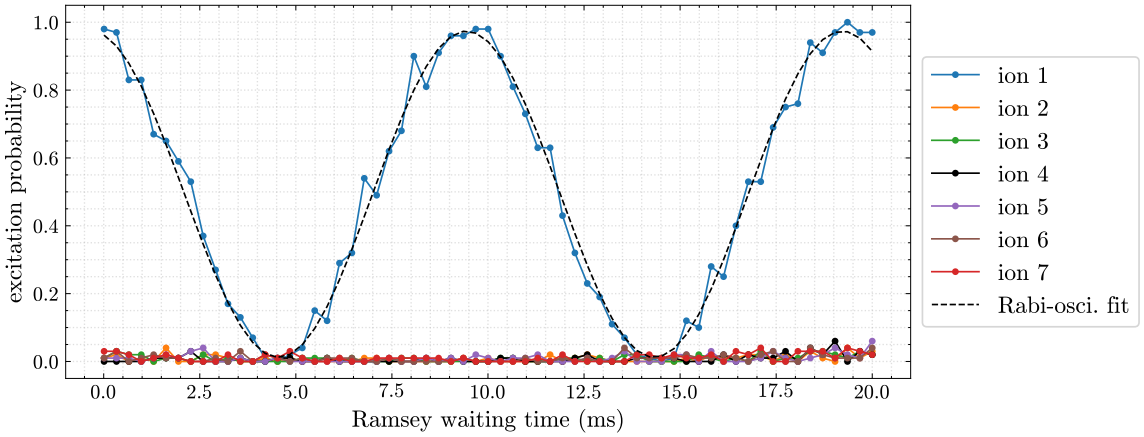


Fig. 6.20: An example of a Ramsey-type time scan with constant single-ion addressing of the first ion in the chain is shown, where the Ramsey waiting time is used as the scan variable. A cosine fit yields a Rabi frequency of $\Omega = 102.3\,\mathrm{Hz}$ for the addressed ion, $\Omega = 7.6\,\mathrm{mHz}$ for the nearest neighboring ion, and $\Omega = 1.8\,\mathrm{mHz}$ for the remaining spectator ions with determinable coupling.

The increased noise floor compared to Fig. 6.19 originates primarily from the efficiency of resolved sideband cooling, as well as from experimental factors such as the calibration of the collective $\pi/2$ pulses. By repeating this Ramsey-type time scan while individually addressing each ion in the chain and extracting the corresponding Rabi frequencies of both the addressed and spectator ions, the addressing-induced crosstalk couplings can be represented in matrix form, as shown in Fig. 6.21. Although these values should be regarded as preliminary due to ongoing optimization of the addressing optics, the measured performance is already comparable to, and in some cases exceeds, crosstalk levels reported in similar experiments [100, 101].



Fig. 6.21: Matrix of coherent crosstalk couplings $\epsilon_{i|j}$ between the 7 ions in the chain, obtained from Rabi oscillation fits while individually addressing each ion in separate scans. Each matrix element gives the ratio of the Rabi rate on ion i to that on the intentionally addressed ion j. The diagonal elements are normalized to unity and indicate the driven ion itself.

Owing to the Airy-fringe diffraction limit, it is physically reasonable that only off-resonant addressing schemes [102] achieve crosstalk couplings on the order of $\mathcal{O}(10^{-5})$ without the use of elaborate compensation techniques [103]. As physical gate error rates below typical fault-tolerance thresholds of $\mathcal{O}(10^{-3})$ are compatible with effective quantum error correction (QEC), addressing approaches in other experimental implementations do not necessarily require such stringent suppression of crosstalk couplings when combined with QEC [104].

In view of one of the stated goals of the experiment, namely maximizing the overall gate operation fidelity, the implemented and characterized optical addressing system for single-ion addressing can be regarded as successful. The crosstalk coupling induced by single-ion addressing, which contributes to the total gate error, lies within an acceptable range. Even at this preliminary stage, the best-performing cases for directly neighboring ions reach crosstalk couplings on the order of $\mathcal{O}(10^{-5})$. When considering all nearest-neighbor pairs in the chain, the crosstalk coupling remains on the order of $\mathcal{O}(10^{-4})$ or below.

A comparison of the off-diagonal elements of the crosstalk coupling matrix in Fig. 6.21 reveals that the investigated TEM_{00} mode alignment allows for further improvement. The observed asymmetry indicates that one neighboring ion already exhibits crosstalk couplings close to the targeted level of $\mathcal{O}(10^{-5})$, while the opposite neighbor remains approximately one order of magnitude larger. This behavior is consistent with residual coma aberrations, as suggested by the differing structure of the upper-left and lower-right regions of the matrix, where crosstalk coupling is distributed asymmetrically. The white entries in the matrix correspond to crosstalk couplings below the measurable threshold, as the finite coherence time limits a reliable extraction of values on the order of $\mathcal{O}(10^{-6})$ and below.

The installation of the second counter-propagating radial addressing unit, which completes the double-sided addressing system used to investigate transverse gate operations, was characterized using the same Ramsey-type deflector scans with a fixed waiting time for the addressing unit providing the TEM_{10} mode. Fig. 6.22 shows one of the early deflector scans obtained for the TEM_{10} side. The widths of the double peaks were already in the vicinity of the targeted magnitude, with a mean value of 0.23(1) MHz, corresponding to a minimum waist of $w_0 = 2(1)\,\mu\mathrm{m}$. The separation of the peaks, with a mean value of 0.66(6) MHz, is significantly smaller than that observed for the TEM_{00} mode in Fig. 6.19, where a mean separation of 1.4(1) MHz was obtained. All values were extracted under the same assumptions as for the TEM_{00} side.

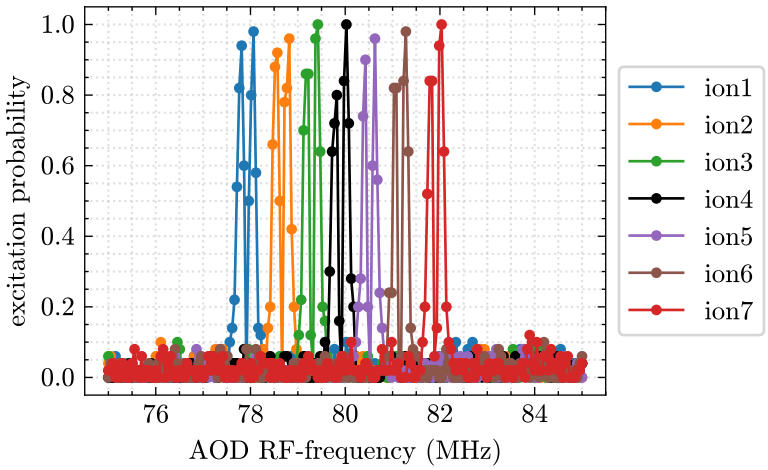


Fig. 6.22: Ramsey-type sequence with underlying single-ion addressing deflector scan with the TEM_{10} mode addressing beam and the Ramsey waiting time fixed at $\tau_{Ramsey} = 100\,\mu s$.

The notable differences in peak separation of both addressing sides are explained by variations in beam propagation lengths, the relative distances between all involved components of the two addressing arms, the properties of the collimated input beams, and the magnification set by the final lens of the beam-expander objective in each addressing unit. The ability to adjust the magnification using the beam-expander objective allows compensation of these contributions. For the early Ramsey deflector scan of the TEM_{10} side shown in Fig. 6.22, the magnification had not yet been properly adjusted.

Bringing the two addressing beams into superposition with such a pronounced mismatch in magnification would result in significantly different spatial deflections per MHz. As a consequence, a stable superposition as aimed for would only be achieved for a single AOD input RF frequency. The rate at which the superposition degrades determines the AOD input RF-frequency range over which it remains undisturbed and is governed by the difference in spatial deflection, which is directly reflected in the separation of the peaks observed in the deflector scans. The optical addressing system was therefore further adjusted to better match the magnifications of both sides, and thus the spatial deflection per MHz, of both addressing arms. The resulting alignment can be demonstrated by overlaying two Ramsey deflector scans, one for the TEM_{00} mode and one for the TEM_{10} mode. Fig. 6.23 shows the achieved superposition of the two addressing beams for a single ion in a 7-ion chain, illustrated by the overlapping Ramsey-type deflector scans. The blue curve corresponds to the Ramsey deflector scan of the TEM_{00} mode, while the red curve corresponds to that of the TEM_{10} mode. The TEM_{00} mode sits at the minimum of the double-peaked intensity distribution of the TEM_{10} mode.

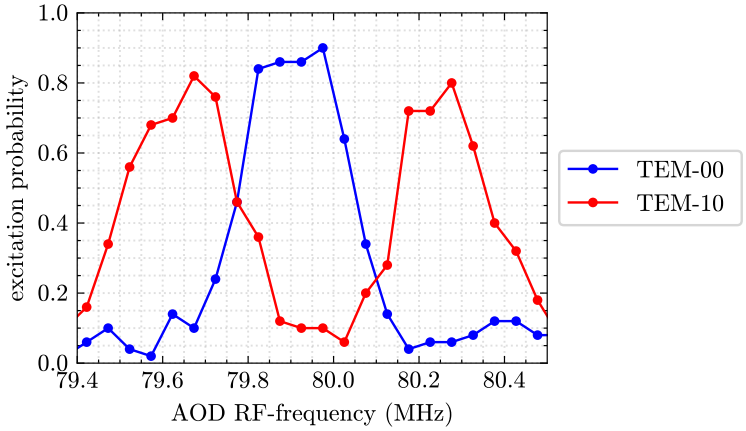


Fig. 6.23: Aligned superposition of TEM_{00} and TEM_{10} addressing beams for a single ion sitting close to the central AOD frequency of 80 MHz.

As Fig. 6.23 shows the alignment of the addressing-beam superposition only for a single ion, based on a zoomed-in region of two overlaid Ramsey-type deflector scans for a 7-ion chain, it reveals the quality of the superposition only within a very limited range. The plot in Fig. 6.24 therefore shows both Ramsey deflector scans overlaid for the complete ion register. As before, the blue curve corresponds to the Ramsey-type deflector

scan of the TEM_{00} mode, while the red curve corresponds to that of the TEM_{10} mode. The central ion, corresponding to the fourth peak of the blue curve, reproduces the zoomed-in region shown previously and represents the target configuration for the alignment, namely a superposition of the two modes at the central frequency of 80 MHz.

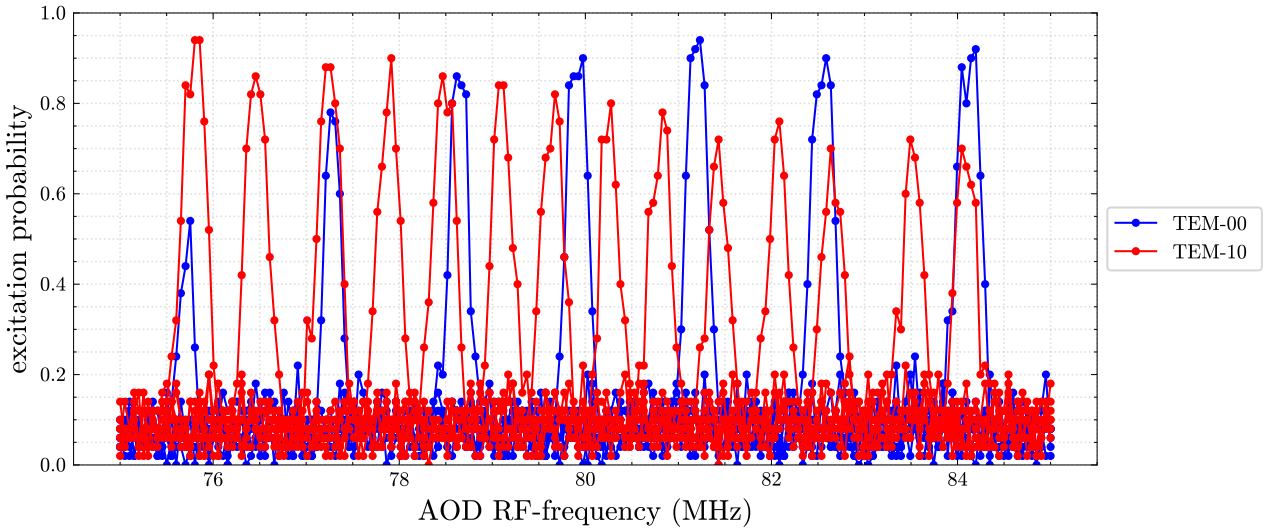


Fig. 6.24: Superposition of the TEM_{00} and TEM_{10} addressing beams for the full 7-ion string, showing the remaining mismatch in angular magnification.

Since the spatial separation of the peaks of both addressing sides was not yet perfectly matched, the two modes exhibit different spatial deflections per MHz, as discussed above. The resulting degradation of the superposition is visible in Fig. 6.24 on both flanks of the central frequency, where the quality of the overlap progressively deteriorates with increasing deflection. For the TEM_{00} mode, the peak separation remained at 1.4(1) MHz, while for the TEM_{10} mode it improved to 1.3(1) MHz. Although the resulting difference in spatial deflection per MHz appears small, it is not negligible. Subsequent investigations revealed that a faulty component within the beam-expander objective was responsible for the persistent difference in magnification between the two addressing arms. After the beam-expander objective was fixed and the angular magnifications of both addressing sides could be matched, a transverse light-shift (LS) gate operation involving two ions in a 2-ion chain was implemented and successfully observed. While the population fidelity was initially decent, the parity population was not. Only after further investigation and additional cooling of the radial modes could a transverse LS gate operation with a total fidelity of 93 % be achieved. The corresponding measurement of the quantum-state evolution during the transverse LS gate operation is shown in Fig. 6.25.

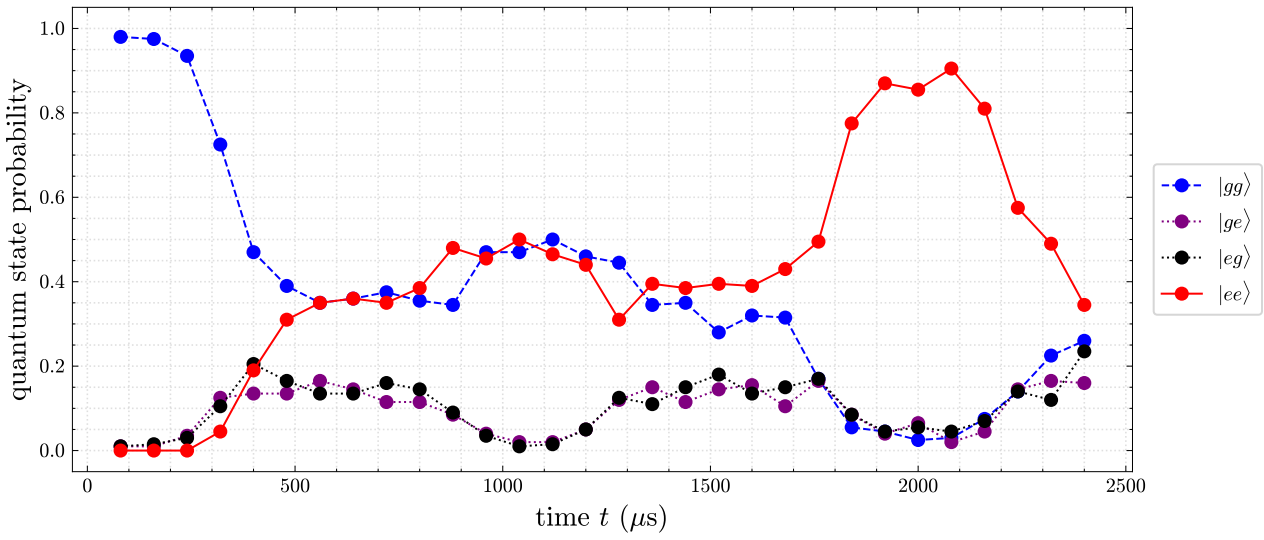


Fig. 6.25: Evolution of quantum states during a transverse light-shift gate operation for 2 ions in a 2-ion chain, visualized by a time scan of the gate operation. For a theoretical comparison, see Fig. 2.20 in Sec. 2.6.

Chapter 7

Conclusion and outlook

This thesis presents several contributions to the mechanical assembly and opto-mechanical characterization of the optical addressing system. The optical characterization began with an assessment of the fiber-coupled input collimators of both addressing units, enabling the selection of a configuration whose properties most closely matched the simulation-based requirements. Dedicated test setups were assembled to investigate system parameters such as efficiency, bandwidth, and frequency response of the acousto-optic deflectors (AODs). In addition, the expected focal spot size and accessible deflection range in the ion plane were analyzed, and the magnitude of Airy-fringe-induced crosstalk was estimated. A detailed analysis of the Zernike coefficients further allowed the exclusion of significant optical aberrations within the addressing systems.

Furthermore, the mechanical integration of the phase plate used to generate the TEM_{10} addressing beam was carried out, followed by a systematic characterization of the resulting beam quality. The achievable total contrast of the superposed addressing beams was experimentally investigated as a function of polarization configuration and relative field amplitudes. The experimental work concluded with a comprehensive documentation of the addressing system installation and performance optimization, culminating in a quantitative investigation of ion-addressing-induced crosstalk. This investigation resulted in the measurement of a complete crosstalk coupling matrix, shown in Fig. 6.21, which provides an experimental assessment of addressing-induced coupling across the ion chain.

With respect to transverse gate operations, the counter-propagating off-resonant radial addressing scheme implemented in the experiment was most likely coupling too strongly to unwanted radial motional modes of the ion chain. This undesired coupling excites additional radial motion and consequently degrades the parity fidelity and, therefore, the overall gate operation fidelity. This observed fidelity degradation originates from the wave-vector mismatch mechanism known from Raman-type gate operations, which arises from the non-zero difference in the propagation wave vectors of the manipulating beams, as described in Eq. 2.5.35 of Sec. 2.5.

Nevertheless, a proof of principle for realizing an entangling light-shift (LS) gate operation using the transverse addressing approach could be demonstrated. After additional cooling of the relevant radial motional modes, a transverse-type LS gate operation with an average total fidelity of 93 % was achieved. The corresponding state evolution is shown in Fig. 6.25. Although the detailed implementation of this gate scheme remains under development, this result confirms the fundamental feasibility of the transverse LS gate concept.

Based on the insights gained in this work, the addressing scheme of the experiment has since been reconsidered. In particular, a transition to a configuration employing co-propagating addressing beams was chosen. This configuration is expected to suppress coupling to radial motional modes and thereby address the principal limitation identified for the transverse approach. A detailed discussion of this revised scheme is presented in another publication, Ref. 68.

Beyond the specific results obtained in this work, the experimental methods and analysis strategies developed for the characterization of tightly focused optical addressing systems may also be applicable to related trapped-ion experiments. In particular, the systematic assessment of optical beam quality, deflection performance, and addressing-induced crosstalk provides a practical framework for evaluating and improving individual-ion control in multi-ion architectures. In this sense, the results presented here contribute to ongoing efforts toward scalable and high-fidelity quantum gate operations based on optical addressing.

Bibliography

[1] M. Planck. "Zur Theorie des Gesetzes der Energieverteilung im Normalspektrum". In: *Verhandlungen der Deutschen Physikalischen Gesellschaft* 2 (1900), pp. 237–245.

[2] A. Einstein. "Über einen die Erzeugung und Verwandlung des Lichtes betreffenden heuristischen Gesichtspunkt". In: *Annalen der Physik* 322.6 (1905), pp. 132–148. DOI: 10.1002/andp.19053220607.

[3] N. Bohr. "On the Constitution of Atoms and Molecules". In: *The London, Edinburgh, and Dublin Philosophical Magazine and Journal of Science* 26.151 (1913), pp. 1–25. DOI: 10.1080/14786441308634955.

[4] W. Heisenberg. "Über quantentheoretische Umdeutung kinematischer und mechanischer Beziehungen". German. In: *Zeitschrift für Physik* 33 (1925), pp. 879–893.

[5] E. Schrödinger. "Quantisierung als Eigenwertproblem". In: *Annalen der Physik* 384.4 (1926), pp. 361–376. DOI: https://doi.org/10.1002/andp.19263840404.

[6] P.A.M. Dirac. "The Quantum Theory of the Electron". In: *Proceedings of the Royal Society of London. Series A, Containing Papers of a Mathematical and Physical Character* 117.778 (1928), pp. 610–624. DOI: 10.1098/rspa.1928.0023.

[7] P.W. Shor. "Algorithms for Quantum Computation: Discrete Logarithms and Factoring". In: *Proceedings of the 35th Annual Symposium on Foundations of Computer Science (FOCS)*. IEEE, 1994, pp. 124–134. DOI: 10.1109/SFCS.1994.365700.

[8] K. Cherkaoui Dekkaki, I. Tasic, and M.D. Cano. "Exploring Post-Quantum Cryptography: Review and Directions for the Transition Process". In: *Technologies* 12.12 (2024). ISSN: 2227-7080. DOI: 10.3390/technologies12120241.

[9] H.J. Manetsch, G. Nomura, E. Bataille, et al. "A tweezer array with 6,100 highly coherent atomic qubits". In: *Nature* 647.8088 (2025), pp. 60–67. ISSN: 1476-4687. DOI: 10.1038/s41586-025-09641-4.

[10] S. McArdle, S. Endo, A. Aspuru-Guzik, et al. "Quantum computational chemistry". In: *Reviews of Modern Physics* 92 (1 2020), p. 015003. DOI: 10.1103/RevModPhys.92.015003.

[11] S. Jordan. *Quantum Algorithm Zoo*. https://quantumalgorithmzoo.org. Accessed: 2025-04-28.

[12] D.P. DiVincenzo. "The Physical Implementation of Quantum Computation". In: *Fortschritte der Physik* 48.9-11 (2000), pp. 771–783. DOI: 10.1002/1521-3978(200009)48:9/11<771::AID-PROP771>3.0.CO;2-E.

[13] T. Nanda, B.K. Dhanalakshmi, and B.N. Lakshmi. "An Explorative Cross Sectional Comprehensive Survey on Quantum Computing". In: *SN Computer Science* 5.8 (2024), p. 1130. ISSN: 2661-8907. DOI: 10.1007/s42979-024-03505-w.

[14] S.S. Gill, A. Kumar, H. Singh, et al. "Quantum computing: A taxonomy, systematic review and future directions". In: *Software: Practice and Experience* 52.1 (2022), pp. 66–114. DOI: 10.1002/spe.3039.

[15] H. Häffner, C.F. Roos, and R. Blatt. "Quantum computing with trapped ions". In: *Physics Reports* 469.4 (2008), pp. 155–203. ISSN: 0370-1573. DOI: https://doi.org/10.1016/j.physrep.2008.09.003.

[16] Y.L. Xu, L. Zhang, C. Zhang, et al. "Long-Time Storage of a Qubit Encoded in Decoherence-Free Subspace Using a Dual-Type Quantum Memory". In: *Physical Review Letters* 135 (23 2025), p. 230803. DOI: 10.1103/mjqd-9mvf.

[17] J. Preskill. "Quantum Computing in the NISQ era and beyond". In: *Quantum* 2 (2018), p. 79. ISSN: 2521-327X. DOI: 10.22331/q-2018-08-06-79. arXiv: arXiv:1801.00862 [quant-ph].

[18] Z. Cai, R. Babbush, S.C. Benjamin, et al. "Quantum error mitigation". In: *Reviews of Modern Physics* 95 (2023), p. 045005. DOI: 10.1103/RevModPhys.95.045005.

[19] C.D. Bruzewicz, J. Chiaverini, R. McConnell, et al. "Trapped-ion quantum computing: Progress and challenges". In: *Applied Physics Reviews* 6.2 (2019). ISSN: 1931-9401. DOI: 10.1063/1.5088164. arXiv: 1904.04178 [quant-ph].

[20] M.A. Nielsen and I.L. Chuang. *Quantum Computation and Quantum Information*. Cambridge University Press, 2010. ISBN: 9781107002173. DOI: 10.1017/CBO9780511976667.

[21] D.J. Griffiths. *Introduction to Quantum Mechanics*. 3rd ed. Cambridge University Press, 2018. ISBN: 9781107189638.

[22] A. Javadi-Abhari, P. Nation, L. Bishop, et al. *Quantum Computing with Qiskit*. 2024. arXiv: 2405.08810 [quant-ph]. URL: https://arxiv.org/abs/2405.08810.

[23] C.M. Dawson and M.A. Nielsen. "The Solovay-Kitaev algorithm". In: *Quantum Information and Computation* 6.1 (2006), pp. 81–95. ISSN: 1533-7146.

[24] D. Gottesman. "Stabilizer Codes and Quantum Error Correction". Available at https://arxiv.org/pdf/quant-ph/9705052v1. PhD thesis. California Institute of Technology, 1997.

[25] V. Bergholm, J. Izaac, M. Schuld, et al. *PennyLane: Automatic Differentiation of Hybrid Quantum-Classical Computations*. arXiv preprint. 2022. arXiv: 1811.04968 [quant-ph].

[26] F. Verstraete, J. Dehaene, B. De Moor, et al. "Four qubits can be entangled in nine different ways". In: *Physical Review A* 65.5 (2002), p. 052112. DOI: 10.1103/PhysRevA.65.052112.

[27] A.E. Siegman. *Lasers*. Mill Valley, CA: University Science Books, 1986. ISBN: 9780935702118.

[28] E. Zauderer. "Complex argument Hermite–Gaussian and Laguerre–Gaussian beams". In: *J. Opt. Soc. Am. A* 3.4 (1986), pp. 465–469. DOI: 10.1364/JOSAA.3.000465.

[29] F. Pampaloni and J. Enderlein. *Gaussian, Hermite-Gaussian, and Laguerre-Gaussian beams: A primer*. arXiv:physics/0410021. 2004. arXiv: physics/0410021 [physics.optics].

[30] B.E.A. Saleh and M.C. Teich. *Fundamentals of Photonics*. 3rd ed. Hoboken, NJ: Wiley, 2019. ISBN: 9781119506874.

[31] G.B. Airy. "On the Diffraction of an Object-Glass with Circular Aperture". In: *Transactions of the Cambridge Philosophical Society* 5.3 (1835), pp. 283–291. URL: https://archive.org/details/transactionsofca05camb/page/282/.

[32] S. van Haver. "The Extended Nijboer–Zernike Diffraction Theory and its Applications". PhD thesis. Delft, The Netherlands: Delft University of Technology, 2010. ISBN: 978-90-78314-12-7.

[33] Nobel Prize Organization. *The Nobel Prize in Physics 1989 – W. Paul*. Accessed: 2026-03-13. 1989. URL: https://www.nobelprize.org/prizes/physics/1989/paul/biographical/.

[34] K.F. Gauss. "Allgemeine Lehrsätze in Beziehung auf die im verkehrten Verhältnisse des Quadrats der Entfernung wirkenden Anziehungs- und Abstossungs-Kräfte". In: *Gesammelte Werke. Band 5*. Originally written 1835–1839; first published 1840. Göttingen: Königliche Gesellschaft der Wissenschaften zu Göttingen, 1877, pp. 197–244.

[35] M. Wiesinger, F. Stuhlmann, M.A. Bohman, et al. "Trap-integrated fluorescence detection with silicon photomultipliers for sympathetic laser cooling in a cryogenic Penning trap". In: *Review of Scientific Instruments* 94.12 (2023), p. 123202. DOI: 10.1063/5.0170629.

[36] J. Berrocal and D. Rodríguez. "High-performance in-vacuum optical system for quantum optics experiments in a Penning-trap". In: *EPJ Quantum Technology* 12.58 (2025). DOI: 10.1140/epjqt/s40507-025-00357-y.

[37] B.J. McMahon, K.R. Brown, C.D. Herold, et al. "Individual-Ion Addressing and Readout in a Penning Trap". In: *Physical Review Letters* 133 (2024), p. 173201. DOI: 10.1103/PhysRevLett.133.173201.

[38] D. Tandeitnik, O. Kremer, F. Almeida, et al. "All-optical saddle trap". In: *Physical Review Applied* 22.4 (2024), p. 044073. DOI: 10.1103/PhysRevApplied.22.044073.

[39] V.I. Baranov, D.R. Bandura, and S.D. Tanner. "Limitations of the effective potential for the evaluation of the ion energy in the RF-driven quadrupole field". In: *International Journal of Mass Spectrometry* 247.1 (2005), pp. 40–47. ISSN: 1387-3806. DOI: 10.1016/j.ijms.2005.08.011.

[40] F.G. Major, V.N. Gheorghe, and G. Werth. *Charged Particle Traps: Physics and Techniques of Charged Particle Field Confinement*. Vol. 37. Springer Series on Atomic, Optical, and Plasma Physics. Berlin: Springer, 2005. ISBN: 9783540220435.

[41] A. Maitra, D. Leibfried, D. Ullmo, et al. "Far-from-equilibrium noise-heating and laser-cooling dynamics in radio-frequency Paul traps". In: *Physical Review A* 99.4 (2019), p. 043421. DOI: 10.1103/PhysRevA.99.043421.

[42] A. Mohammadi, J. Wolf, A. Krükow, et al. "Minimizing rf-induced excess micromotion of a trapped ion with the help of ultracold atoms". In: *Applied Physics B* 125.7 (2019), p. 122. ISSN: 1432-0649. DOI: 10.1007/s00340-019-7223-y.

[43] D. Leibfried, R. Blatt, C. Monroe, et al. "Quantum dynamics of single trapped ions". In: *Reviews of Modern Physics* 75 (1 2003), pp. 281–324. DOI: 10.1103/RevModPhys.75.281.

[44] P.K. Ghosh. *Ion Traps*. Oxford, UK: Oxford University Press (Clarendon Press), 1996. ISBN: 978-0-19-8539957.

[45] M. Knoop, I. Marzoli, and G. Morigi, eds. *Ion Traps for Tomorrow's Applications*. Proceedings of the International School of Physics "Enrico Fermi", Course 189. Amsterdam: IOS Press and Società Italiana di Fisica, 2015. ISBN: 978-1-61499-526-5.

[46] K. Zimmermann, M.V. Okhapkin, O.A. Herrera-Sancho, et al. "Laser ablation loading of a radiofrequency ion trap". In: *Applied Physics B* 107.4 (2012), pp. 883–889. ISSN: 1432-0649. DOI: 10.1007/s00340-012-4884-1.

[47] R. Wester. "Radiofrequency multipole traps: tools for spectroscopy and dynamics of cold molecular ions". In: *Journal of Physics B: Atomic, Molecular and Optical Physics* 42.15 (2009), p. 154001. DOI: 10.1088/0953-4075/42/15/154001.

[48] K. J. Arnold, S. R. Chanu, R. Kaewuam, et al. "Measurements of the branching ratios for $6P_{1/2}$ decays in $^{138}Ba^{+}$". In: *Physical Review A* 100 (3 2019), p. 032503. DOI: 10.1103/PhysRevA.100.032503.

[49] Z. Zhang, K.J. Arnold, S.R. Chanu, et al. "Branching fractions for $P_{3/2}$ decays in Ba^{+}". In: *Physical Review A* 101 (6 2020), p. 062515. DOI: 10.1103/PhysRevA.101.062515. arXiv: 2003.02263 [physics.atom-ph].

[50] H.J. Metcalf and P. van der Straten. *Laser Cooling and Trapping*. Graduate Texts in Contemporary Physics. New York: Springer, 1999. ISBN: 978-0-387-98747-7. DOI: 10.1007/978-1-4612-1470-0.

[51] J.Z. Klose, J.R. Fuhr, and W.L. Wiese. "Critically Evaluated Atomic Transition Probabilities for Ba I and Ba II". In: *Journal of Physical and Chemical Reference Data* 31.1 (2002), pp. 217–230. DOI: 10.1063/1.1448482.

[52] F. Schmidt-Kaler, J. Eschner, R. Blatt, et al. "Laser Cooling of Trapped Ions". In: *Laser Physics at the Limits*. Ed. by H. Figger, C. Zimmermann, and D- Meschede. Berlin, Heidelberg: Springer Berlin Heidelberg, 2002, pp. 243–260. ISBN: 978-3-662-04897-9. DOI: 10.1007/978-3-662-04897-9_24.

[53] L. Allen and J.H. Eberly. *Optical Resonance and Two-Level Atoms*. New York: Dover Publications, 1975. ISBN: 978-0486655338.

[54] J.J. Sakurai and J. Napolitano. *Modern Quantum Mechanics*. 2nd. San Francisco: Addison-Wesley, 2011. ISBN: 978-0-8053-8291-4.

[55] A.H. Myerson, D.J. Szwer, S.C. Webster, et al. "High-Fidelity Readout of Trapped-Ion Qubits". In: *Phys. Rev. Lett.* 100 (20 2008), p. 200502. DOI: 10.1103/PhysRevLett.100.200502.

[56] F. Zähringer, G. Kirchmair, R. Gerritsma, et al. "Realization of a Quantum Walk with One and Two Trapped Ions". In: *Physical Review Letters* 104 (10 2010), p. 100503. DOI: 10.1103/PhysRevLett.104.100503.

[57] C. Cohen-Tannoudji, J. Dupont-Roc, and G. Grynberg. *Photons and Atoms: Introduction to Quantum Electrodynamics*. 1st ed. New York: John Wiley & Sons, 1997. ISBN: 978-0-471-18433-1.

[58] C. Cohen-Tannoudji, J. Dupont-Roc, and G. Grynberg. *Atom-Photon Interactions: Basic Processes and Applications*. New York: John Wiley & Sons, 1998. ISBN: 978-0-471-29336-1.

[59] R. Loudon. *The Quantum Theory of Light*. 3rd ed. Oxford: Oxford University Press, 2000. ISBN: 978-0-19-850176-3.

[60] D.J. Wineland, M. Barrett, J. Britton, et al. "Quantum information processing with trapped ions". In: *Philosophical Transactions of the Royal Society A: Mathematical, Physical and Engineering Sciences* 361.1808 (2003), pp. 1349–1361. DOI: 10.1098/rsta.2003.1205.

[61] R. Hobson, W. Bowden, S.A. King, et al. "Modified hyper-Ramsey methods for the elimination of probe shifts in optical clocks". In: *Physical Review A* 93.1 (2016), p. 010501. DOI: 10.1103/PhysRevA.93.010501.

[62] E.L. Hahn. "Spin Echoes". In: *Physical Review* 80.4 (1950), pp. 580–594. DOI: 10.1103/PhysRev.80.580.

[63] R. Blatt and D. Wineland. "Entangled states of trapped atomic ions". In: *Nature* 453 (2008), pp. 1008–1015. DOI: 10.1038/nature07125.

[64] A. Sørensen and K. Mølmer. "Quantum Computation with Ions in Thermal Motion". In: *Physical Review Letters* 82.9 (1999), pp. 1971–1974. DOI: 10.1103/PhysRevLett.82.1971.

[65] D. Jonathan and M.B. Plenio. "Light-shift-induced quantum gates for ions in thermal motion". In: *Physical Review Letters* 87.12 (2001), p. 127901. DOI: 10.1103/PhysRevLett.87.127901.

[66] G. Kirchmair, J. Benhelm, F. Zähringer, et al. "Deterministic entanglement of ions in thermal states of motion". In: *New Journal of Physics* 11.2 (2009), p. 023002. DOI: 10.1088/1367-2630/11/2/023002.

[67] A. Ashkin, J.M. Dziedzic, J.E. Bjorkholm, et al. "Observation of a single-beam gradient force optical trap for dielectric particles". In: *Optics Letters* 11.5 (1986), pp. 288–290. DOI: 10.1364/OL.11.000288.

[68] T. Faorlin, L. Panzl, P. Grosser, et al. *Entangling ions with engineered light gradients*. 2026. arXiv: 2603.07548 [quant-ph]. URL: https://arxiv.org/abs/2603.07548.

[69] C.H. Baldwin, B.J. Bjork, M. Foss-Feig, et al. "High-fidelity light-shift gate for clock-state qubits". In: *Physical Review A* 103 (1 2021), p. 012603. DOI: 10.1103/PhysRevA.103.012603. arXiv: 2003.01102 [quant-ph].

[70] J. Eschner, G. Morigi, F. Schmidt-Kaler, et al. "Laser cooling of trapped ions". In: *Journal of the Optical Society of America B* 20.5 (2003), pp. 1003–1015. DOI: 10.1364/JOSAB.20.001003.

[71] R. Ozeri, W.M. Itano, R.B. Blakestad, et al. "Errors in trapped-ion quantum gates due to spontaneous photon scattering". In: *Physical Review A* 75 (4 2007), p. 042329. DOI: 10.1103/PhysRevA.75.042329.

[72] D. Mishin, D.O. Tregubov, N. Kolachevsky, et al. "Coherence of Microwave and Optical Qubit Levels in Neutral Thulium". In: *PRX Quantum* 6.4 (2025). Preprint version available as arXiv:2508.12887, p. 040329. DOI: 10.1103/f8xg-w57m. arXiv: 2508.12887 [quant-ph].

[73] M. Zhong, M.P. Hedges, R.L. Ahlefeldt, et al. "Optically addressable nuclear spins in a solid with a six-hour coherence time". In: *Nature* 517.7533 (2015), pp. 177–180. DOI: 10.1038/nature14025.

[74] A. Abragam. *Principles of Nuclear Magnetism*. International Series of Monographs on Physics. Oxford: Oxford University Press, 1961. ISBN: 978-0-19-852014-6.

[75] C.P. Slichter. *Principles of Magnetic Resonance*. 3rd. Vol. 1. Springer Series in Solid-State Sciences. Berlin, Heidelberg: Springer, 1989, p. 658. ISBN: 978-3-540-50157-2. DOI: 10.1007/978-3-662-09441-9.

[76] H.P. Breuer and F. Petruccione. *The Theory of Open Quantum Systems*. Oxford University Press, 2007. ISBN: 9780199213900. DOI: 10.1093/acprof:oso/9780199213900.001.0001.

[77] C.J. Foot. *Atomic Physics*. Oxford Master Series in Atomic, Optical and Laser Physics. Oxford: Oxford University Press, 2005. ISBN: 9780198506966.

[78] R.D. Cowan. *The Theory of Atomic Structure and Spectra*. Los Alamos Series in Basic and Applied Sciences. Berkeley, CA: University of California Press, 1981. ISBN: 978-0-520-90615-0.

[79] M. Ramm, T. Pruttivarasin, M. Kokish, et al. "Precision Measurement Method for Branching Fractions of Excited $P_{1/2}$ States Applied to $^{40}Ca^{+}$". In: *Physical Review Letters* 111 (2 2013), p. 023004. DOI: 10.1103/PhysRevLett.111.023004.

[80] M. Hettrich, T. Ruster, H. Kaufmann, et al. "Measurement of Dipole Matrix Elements with a Single Trapped Ion". In: *Physical Review Letters* 115 (14 2015), p. 143003. DOI: 10.1103/PhysRevLett.115.143003.

[81] A. Kreuter, C. Becher, G.P.T. Lancaster, et al. "Experimental and theoretical study of the $3d\,^2D$–level lifetimes of $^{40}Ca^{+}$". In: *Physical Review A* 71 (3 2005), p. 032504. DOI: 10.1103/PhysRevA.71.032504.

[82] I. Pogorelov, T. Feldker, C.D. Marciniak, et al. "Compact Ion-Trap Quantum Computing Demonstrator". In: *PRX Quantum* 2 (2 2021), p. 020343. DOI: 10.1103/PRXQuantum.2.020343.

[83] C.F. Roos. "Controlling the Quantum State of Trapped Ions". PhD thesis. PhD thesis. Innsbruck, Austria: University of Innsbruck, 2004. URL: https://www.uibk.ac.at/thesis/roos2004.pdf.

[84] C. Auchter, T.W. Noel, M.R. Hoffman, et al. "Measurement of the branching fractions and lifetime of the $5D_{5/2}$ level of Ba^{+}". In: *Physical Review A* 90 (6 2014), p. 060501. DOI: 10.1103/PhysRevA.90.060501.

[85] D. Yum, D. De Munshi, T. Dutta, et al. "Optical barium ion qubit". In: *Journal of the Optical Society of America B* 34.8 (2017), pp. 1632–1636. DOI: 10.1364/JOSAB.34.001632.

[86] D. Hucul, J.E. Christensen, E.R. Hudson, et al. "Spectroscopy of a Synthetic Trapped Ion Qubit". In: *Physical Review Letters* 119 (10 2017), p. 100501. DOI: 10.1103/PhysRevLett.119.100501.

[87] Newport Corporation. *S-2000A Pneumatic Vibration Isolators with Automatic Re-Leveling*. https://www.newport.com/f/pneumatic-vibration-isolators-with-automatic-re-leveling. Accessed: 2025-12-11. 2025.

[88] T. Monz, P. Schindler, J.T. Barreiro, et al. "14-Qubit Entanglement: Creation and Coherence". In: *Physical Review Letters* 106 (13 2011), p. 130506. DOI: 10.1103/PhysRevLett.106.130506.

[89] Radiant ZEMAX, LLC. *ZEMAX Optical Design Program: User's Manual*. ZEMAX 2011 Release. Redmond, WA, 2011.

[90] E. Hecht. *Optics*. 5th ed. Upper Saddle River, NJ: Pearson Education, 2016. ISBN: 978-1-292-09693-3.

[91] S. Kim. "Acousto-Optic Devices for Optical Signal Processing and Quantum Computing". Doctor of Philosophy thesis. PhD thesis. Boulder, CO: University of Colorado Boulder, 2008.

[92] H. Kogelnik. "Coupled wave theory for thick hologram gratings". In: *The Bell System Technical Journal* 48.9 (1969), pp. 2909–2947. DOI: 10.1002/j.1538-7305.1969.tb01198.x.

[93] K.J. Åström and R.M. Murray. *Feedback Systems: An Introduction for Scientists and Engineers*. 1st ed. Princeton Series in Applied Science. Princeton, NJ: Princeton University Press, 2008. ISBN: 978-0-691-13576-2.

[94] E.A. Donley, T.P. Heavner, F. Levi, et al. "Double-pass acousto-optic modulator system". In: *Review of Scientific Instruments* 76.6 (2005), p. 063112. DOI: 10.1063/1.1930095.

[95] G.F. Marshall and G.E. Stutz, eds. *Handbook of Optical and Laser Scanning*. 2nd ed. Boca Raton, FL: CRC Press, 2011. ISBN: 978-1-4398-0879-5. DOI: 10.1201/9781315218243.

[96] S. Perrin and P. Montgomery. "Fourier Optics: Basic Concepts". In: *arXiv preprint arXiv:1802.07161* (2018). arXiv: 1802.07161 [physics.optics].

[97] J.W. Goodman. *Introduction to Fourier Optics*. 3rd ed. Englewood, CO: Roberts and Company Publishers, 2005. ISBN: 978-0-9747077-2-3.

[98] J. Gao. "R-Squared (R2) – How much variation is explained?" In: *Research Methods in Medicine & Health Sciences* 5.4 (2024), pp. 104–109. DOI: 10.1177/26320843231186398.

[99] C.R. Clark, H.N. Tinkey, B.C. Sawyer, et al. "High-Fidelity Bell-State Preparation with $^{40}Ca^{+}$ Optical Qubits". In: *Physical Review Letters* 127 (13 2021), p. 130505. DOI: 10.1103/PhysRevLett.127.130505.

[100] A.S. Sotirova, B. Sun, J.D. Leppard, et al. "Low cross-talk optical addressing of trapped-ion qubits using a novel integrated photonic chip". In: *Light: Science & Applications* 13 (2024). DOI: 10.1038/s41377-024-01542-x.

[101] Y.-L. Chen, R.-R. Li, R. He, et al. "Low-crosstalk optical addressing system for atomic qubits based on multiple objectives and acousto-optic deflectors". In: *Physical Review Applied* 22 (5 2024), p. 054003. DOI: 10.1103/PhysRevApplied.22.054003.

[102] C. Piltz, T. Sriarunothai, A.F. Varón, et al. "A trapped-ion-based quantum byte with 10^{-5} next-neighbour cross-talk". In: *Nature Communications* 5 (2014). DOI: 10.1038/ncomms5679.

[103] J. Flannery, R. Matt, L.I. Huber, et al. "Physical coherent cancellation of optical addressing crosstalk in a trapped-ion experiment". In: *Quantum Science and Technology* 10.1 (2024), p. 015012. DOI: 10.1088/2058-9565/ad8371.

[104] A.G. Fowler, M. Mariantoni, J.M. Martinis, et al. "Surface codes: Towards practical large-scale quantum computation". In: *Physical Review A* 86.3 (2012), p. 032324. DOI: 10.1103/PhysRevA.86.032324.

Chapter 8

Acknowledgment

First and foremost, I would like to express my sincere gratitude to Assoz. Prof. Dr. Thomas Monz for giving me the opportunity and the privilege to work on a project such as Hyperion. I am deeply thankful for his guidance, his time, and his willingness to discuss questions and ideas, despite his demanding schedule. I will always remember this experience. During periods in which he was not available, Ass.-Prof. Dr. Martin Ringbauer and Ass.-Prof. Dr. Schindler Philip kindly provided support and guidance, for which I am equally grateful.

I would also like to extend my thanks to Prof. Dr. Rainer Blatt and his entire research group for welcoming me so warmly into the laboratory environment. In particular, I would like to thank the barium team: Cerchiari Giovanni, Weiser Yannick, Panzl Lorenz, and Faorlin Tommaso. It was a true privilege to work alongside them in the laboratories in Innsbruck over the past year. Their support, patience, and expertise strongly shaped my experience, and a substantial part of what I was able to learn and understand during this time is owed to them. I would also like to acknowledge my fellow Master's students Alfaro-Campos Sara, Lafenthaler Thomas, and Tian Haonan, whose collegiality and mutual support greatly contributed to this period.

Special thanks also go to Feldker Thomas, Nigg Daniel, Jacob Georg, and all members of the AQT company involved in this project. Their assistance and professional support on many occasions meant, and continue to mean, a great deal to the barium team.

I would further like to express my gratitude to the staff of the institute's mechanical workshop: Wegscheider Christoph, Schönherr Anton, and Markt Lukas. Their high-quality work made many custom adaptations feasible within the institute, significantly reducing both turnaround times and costs compared to external manufacturing.

For transparency, I would like to note that the AI tool ChatGPT (OpenAI) was used to assist with debugging and improving code snippets, as well as to refine the clarity and language of this thesis. All scientific results, interpretations, and conclusions were independently verified by the author such that the artificial intelligence was used in a responsible manner. In addition, the optical component library by Alexander Franzen, licensed under Creative Commons Attribution–NonCommercial, was used for the creation of some schematics presented in this thesis.

Last but the very opposite of least, I would like to express my infinite gratitude to my parents, Helga Maria Hörmann and Walter Maria Hörmann. Without them, I would neither be who I am today nor where I am today. I hope that I can meet their expectations and make them proud, even if only in a small way. My mother, in particular, could seriously be considered for sainthood, as I am quite certain that I will never be able to repay even a fraction of her kindness, love, and time.

This thesis shall end now with a quote, that can be found at the beginning of Ref. [32]:

> *How quick are we to learn, that is, to imitate what others have done or thought before. And how slow to understand, that is, to see the deeper connections. Slowest of all, however, are we in inventing new connections or even in applying old ideas in a new field.*
> — *Frits Zernike, Nobel Lecture, December 11th, 1953*